

Die approbierte Originalversion dieser Dissertation ist an der Hauptbibliothek der Technischen Universität Wien aufgestellt (<http://www.ub.tuwien.ac.at>).

The approved original version of this thesis is available at the main library of the Vienna University of Technology (<http://www.ub.tuwien.ac.at/englweb/>).

DISSERTATION

# Photonic Crystal Intersubband Photodetectors

ausgeführt zum Zwecke der Erlangung des akademischen Grades eines  
Doktors der technischen Wissenschaften

unter der Leitung von

Univ.-Prof. Dr. Gottfried Strasser  
Institut für Festkörperelektronik

eingereicht an der

TECHNISCHEN UNIVERSITÄT WIEN  
FAKULTÄT FÜR ELEKTROTECHNIK UND INFORMATIONSTECHNIK

von

**Dipl.-Ing. Stefan Kalchmair**

Mat.Nr. 0226230

Domgasse 4 / 33

1010 Wien

Wien, im Juni 2012

1. Gutachter : Univ. Prof. Dr. Gottfried Strasser
2. Gutachter : PD Dr. habil. Harald Schneider

Tag der mündlichen Prüfung: 29. Juni 2012

"Ich bin wirklich erleichtert, dass sich das Universum endlich erklären lässt.  
Ich dachte schon, das Problem läge bei mir."

Woody Allen



# Danksagung

Dies ist ein Dank an alle, die mich im Laufe dieser Arbeit unterstützt haben. Zuallererst gilt mein Dank meinem Doktorvater Univ. Prof. Dr. Gottfried Strasser für die Betreuung und für die Möglichkeit, in seiner großartigen Forschungsgruppe mitzuwirken.

Ich bedanke mich bei meinen Kollegen Sang Il Ahn, Alexander Alexewicz, Max Andrews, Bernhard Basnar, Alexander Benz, Garrett Cole, Hermann Detz, Roman Gansch, Tobias Kaposi, Pavel Klang, Elvis Mujagic, Michele Nobile, Clemens Ostermaier, Daniela Ristanic, Stephan Schartner, Werner Schrenk, Benedikt Schwarz, Clemens Schwarzer und Tobias Zederbauer für die nette Atmosphäre und die vielen interessanten Gespräche.

Ganz besonders bedanke ich mich bei Roman Gansch für die intensive Zusammenarbeit bei der Erforschung der PCS-QWIPs, für seine genialen Simulations-Tools und für die hochwertigen Diskussionen.

Max Andrews danke ich speziell für die unzähligen Korrekturen und Kommentare in meinen englischen Texten. Durch seine steten Verbesserungen wurden meine englischsprachigen Fähigkeiten ‚significantly improved‘.

Großer Dank gilt Werner Schrenk für die intensiven und gnadenlosen Diskussionen auf der Suche nach der richtigen Lösung.

Meinen Bürokollegen und Freunden Sang Il Ahn, Hermann Detz und Daniela Ristanic danke ich für die motivierenden Gespräche, die spannenden Diskussionen am Whiteboard und die wundervolle gemeinsame Zeit.

Besonderer Dank gilt auch PD Dr. Harald Schneider für die wegweisende Diskussion. Die kurze Zeit in seiner Forschungsgruppe gab mir den richtigen Impuls um mein Projekt erfolgreich abzuschließen.

Spezieller Dank geht an Clemens Ostermaier, der mich stets herausfordert und ermutigt hat. Er hat in vielerlei Hinsicht zum Erfolg dieser Dissertation und vieler anderer Projekte beigetragen.

Bei meiner Freundin Marion Altinger bedanke ich mich besonders für die stete Motivation und für die gemeinsame Freude an den Erfolgen.

Meinen Eltern und meinen Geschwistern danke ich von ganzem Herzen für die Unterstützung während meiner Dissertation und meines gesamten Studiums. Durch sie konnte ich diese hochwertige Ausbildung genießen.



# Abstract

The focus of this thesis was to improve the performance of quantum well infrared photodetectors (QWIPs). Today, commercially available QWIPs have detectivities up to  $10^{11} \text{ cm Hz}^{1/2}/W$ . Modern QWIP camera systems with megapixel sensors are available and frequently used in astronomy and military countermeasure systems. However, QWIPs suffer from certain drawbacks, in particular the lack of sensitivity to surface-normal incident light and the need for operation at cryogenic temperatures to get reasonable signal-to-noise ratios. The first issue is usually addressed by combining QWIPs with diffraction gratings. The second issue remains unsolved, generally forcing QWIPs to be operated at liquid nitrogen temperatures.

The key element of any photodetector is the absorber, which converts the incoming radiation into a measurable electronic signal. In QWIPs the photons are absorbed by confined electrons in quantum wells. To measure a strong response from any photodetector a large absorption is essential. However, the absorption per quantum well in a standard QWIP is usually below 1%. The total absorption can be increased by using a large number of quantum wells, but the measured photocurrent cannot be increased this way. The internal gain of the QWIP decreases with an increasing number of quantum wells. An efficient way to improving the absorption of the photodetector without altering its electrical properties is by embedding the absorber in a resonant cavity. Photons inside the cavity exhibit a longer lifetime. This increases the absorption probability and hereby the quantum efficiency of the detector. This principle is called resonant cavity enhancement.

We combined QWIPs with photonic crystal slab (PCS) resonators to detect surface-normal incident light and to improve the detector performance. The PCS shows strong resonant properties and excellent vertical mode confinement, which provides a high Q-factor even for radiative photonic crystal modes. The photodetector was built by fabricating a photonic crystal slab from the QWIP heterostructure. By selectively underetching the photonic crystal, a free-standing photonic crystal slab is created. As reference devices, standard mesa QWIPs were fabricated.

The PCS was designed using a time-efficient simulation tool - the revised plane wave expansion method. While a PCS is really a three-dimensional object, it can be approximated as a two-dimensional photonic crystal combined with a simple slab waveguide.

The simulation tool uses this very good approximation, allowing to calculate the entire photonic band structure of the PCS within a matter of seconds.

To measure the spectral photoresponse, all samples were illuminated with a Globar and measured with a Fourier transform infrared spectrometer. The PCS-QWIPs show pronounced resonance peaks, which correspond to the PCS modes. At the resonance frequencies, the photon lifetime in the active region is significantly increased, which causes enhanced absorption and sharp photocurrent peaks.

The absorption enhancement is used to increase the detectivity of the photodetectors. Compared to optimized standard QWIPs with a doping concentration of  $4 \times 10^{11} \text{ cm}^{-2}$ , low-doped QWIPs were grown with 100 times reduced quantum well doping. These low-doped QWIPs exhibit significantly lower dark current noise, but also lower detector responsivity. To increase the responsivity without increasing the detector noise, a PCS-QWIP was designed, where the strongest resonance of the PCS coincides with the peak absorption frequency of the QWIP. With this method a detectivity increase of up to 20 times was shown, compared to standard QWIPs. The detectivity enhancement is a combined effect of responsivity increase and noise current reduction. Low-doped PCS-QWIPs could be operated up to room temperature, still showing reasonable detectivities and manageable dark currents.

# Zusammenfassung

Das Ziel dieser Dissertation war die Verbesserung der Sensitivität von Quantentopf Infrarot Fotodetektoren (*quantum well infrared photodetectors*, QWIP). QWIPs sind heutzutage mit Detektivitäten bis zu  $10^{11} \text{ cm Hz}^{1/2}/\text{W}$  erhältlich. Moderne QWIP Kamerasysteme verfügen über Megapixel-Sensoren und finden Verwendung in der Astronomie und in militärischen Abwehrsystemen.

QWIPs haben jedoch gewisse Nachteile. Ein Nachteil ist die fehlende Sensitivität für senkrecht auf die Oberfläche einfallendes Licht. Ein weiteres Problem ist die Notwendigkeit, QWIPs bei kryogenen Temperaturen zu betreiben um brauchbare Signal-Rausch-Verhältnisse zu erhalten. Die Detektion von senkrecht einfallendem Licht erfolgt, indem ein Beugungsgitter auf den QWIP aufgebracht wird. Das zweite Problem ist bis heute ungelöst und QWIPs müssen weiterhin bei tiefen Temperaturen betrieben werden.

In jedem Fotodetektor findet man einen Absorber, der die auftreffende Strahlung in ein elektronisches Signal umwandelt. In QWIPs wird die Strahlung von den Elektronen in den Quantentöpfen absorbiert. Wichtig für ein starkes Signal ist eine hohe Absorption. Leider ist die Absorption pro Quantentopf in Standard-QWIPs unter 1%. Die Gesamtabsorption kann durch die Verwendung von mehreren Quantentöpfen erhöht werden, aber nicht der gemessene Fotostrom. Die interne Verstärkung reduziert sich proportional zur Anzahl der Quantentöpfe. Eine Möglichkeit zur Erhöhung der Absorption des Fotodetektors, ohne die elektrischen Eigenschaften zu verändern, ist die Verwendung eines optischen Resonators. Photonen im Resonator haben eine längere Lebensdauer, wodurch die Absorptionswahrscheinlichkeit und hiermit die Quanteneffizienz des Detektors erhöht werden. Diese Methode bezeichnet man als resonante Absorptionsverstärkung.

Im Rahmen dieser Arbeiten wurden QWIPs mit photonischen Kristallmembranen (*photonic crystal slabs*, PCS) kombiniert. Dies erlaubt die Detektion von senkrecht auf die Oberfläche einfallendem Licht und die Erhöhung der Sensitivität. Photonische Kristallmembranen sind ausgezeichnete Resonatoren und erlauben sehr gute vertikale Modenföhrung. Selbst für abstrahlende Moden sind hohe Q-Faktoren möglich. Für die Herstellung der Fotodetektoren wurden photonische Kristallmembranen aus der QWIP-Heterostruktur gefertigt. Zuerst wird der photonische Kristall in den QWIP geätzt und danach durch selektives Unterätzen eine freistehende Kristallmembran erzeugt. Als Referenzdetektoren wurden quaderförmige Standard-QWIPs gefertigt.

Für die Simulation der photonischen Kristallmembranen wurde ein zeiteffizientes Programm entwickelt – die *“revised plane wave expansion method”*. Eine photonische Kristallmembran ist zwar ein dreidimensionales Objekt, aber sie kann als reiner zweidimensionaler photonischer Kristall kombiniert mit einem ebenen Wellenleiter angenähert werden. Diese sehr gute Annäherung erlaubt die Berechnung der vollständigen photonischen Bandstruktur innerhalb weniger Sekunden.

Zur Messung der Fotostrom-Spektren wurden alle Proben mit einem Globar beleuchtet und mit einem Fourier-Transformations-Infrarot-Spektrometer analysiert. Das PCS-QWIP-Spektrum zeigt ausgeprägte Resonanzen, die zu den entsprechenden photonischen Kristallmembran-Moden gehören. Die Verweildauer der Photonen im Kristall bei der Resonanzfrequenz ist deutlich länger, wodurch die Absorption verstärkt wird und scharfe Resonanzspitzen entstehen.

Die resonante Absorptionsverstärkung kann genutzt werden um die Sensitivität des Fotodetektors zu erhöhen. Die Dotierung optimierter Standard-QWIPs für  $8\ \mu\text{m}$  Wellenlänge ist  $4 \times 10^{11}\ \text{cm}^{-2}$ . Um das Dunkelstromrauschen zu verringern wurden niedrig dotierte QWIPs mit 100-mal geringerer Dotierung gewachsen. Dadurch sinkt auch die Empfindlichkeit dieser niedrig dotierten QWIPs. Um die Empfindlichkeit zu erhöhen ohne mehr Detektorrauschen zu erzeugen wurde ein PCS-QWIP gefertigt, bei dem die stärkste Resonanz und das Absorptionsmaximum des QWIPs übereinanderliegen. Durch diese Methode wurde eine bis zu 20-fach höhere Detektivität erreicht, verglichen mit Standard-QWIPs. Diese Erhöhung der Detektivität ergibt sich aus einer Kombination der Erhöhung der Empfindlichkeit und der Verringerung des Detektorrauschens. Niedrig dotierte PCS-QWIPs wurden erfolgreich bei Raumtemperatur betrieben und zeigten noch immer akzeptable Detektivität und handhabbare Dunkelströme.

# Contents

<b>Abstract</b>	<b>v</b>
<b>Zusammenfassung</b>	<b>vii</b>
<b>1 Introduction</b>	<b>1</b>
1.1 Mid-infrared Optoelectronics . . . . .	1
1.2 Photonic Crystals . . . . .	10
<b>2 Quantum Well Infrared Photodetectors</b>	<b>17</b>
2.1 Electronic Intersubband Transitions . . . . .	18
2.2 Photocurrent . . . . .	22
2.3 Detector Performance . . . . .	30
<b>3 Photonic Crystal Resonators</b>	<b>37</b>
3.1 Theory of Photonic Crystals . . . . .	37
3.2 1D Photonic Crystals . . . . .	48
3.3 2D Photonic Crystals . . . . .	54
<b>4 Photonic Crystal QWIPs</b>	<b>63</b>
4.1 Design and Fabrication . . . . .	63
4.2 Experimental Results . . . . .	77
4.3 Detectivity Enhancement . . . . .	93
4.4 Resonance Tuning . . . . .	98
<b>5 Summary and Outlook</b>	<b>101</b>
<b>Appendix</b>	<b>107</b>
<b>Bibliography</b>	<b>117</b>
<b>Abbreviations</b>	<b>133</b>
<b>List of Publications</b>	<b>135</b>
<b>Curriculum Vitae</b>	<b>141</b>



# 1 Introduction

## 1.1 Mid-infrared Optoelectronics

The infrared (IR) radiation was discovered over 200 years ago by the astronomer William Herschel. He was passing sunlight through a prism and measuring the temperature of each color by holding thermometers into the light. In this experiment, he found that the temperature increases from the violet to the red end of the spectrum. To measure the ambient air temperature, which would serve as a control sample, he placed thermometers just beyond the red end of the visible spectrum. Instead this region showed a higher temperature than anywhere in the visible spectrum (Fig. 1.1). After further experiments he concluded that there must be an invisible form of light beyond the visible spectrum, which today is called the *infrared light* [1].

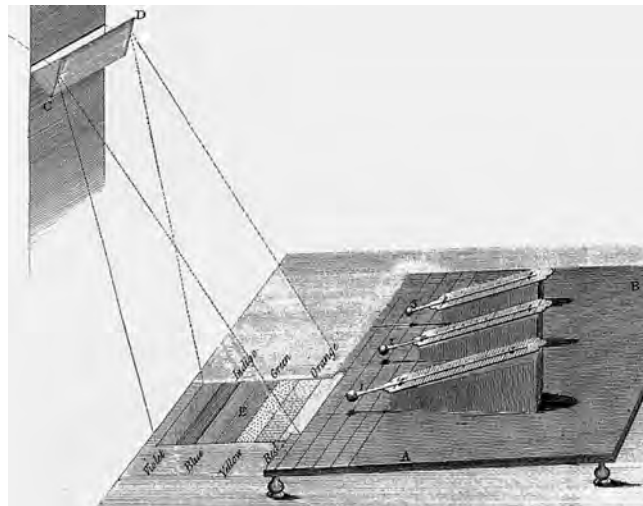


Figure 1.1: William Herschel's experimental setup, which led to the discovery of the infrared radiation. (Published in [2])

Since then continuous research was conducted to develop reliable and cost-efficient infrared light emitters and detectors. The mid-IR region ( $3 - 30 \mu m$ ) is particularly interesting for numerous applications including environmental monitoring, optical gas

sensing, infrared countermeasures and thermal imaging [3]. Mid-IR spectroscopy has become a standard tool for chemical analysis, since many chemical compounds show unique absorption lines in this spectral region (Fig. 1.2). Hence, the mid-IR spectral range is also called the chemical *finger print* region. Monitoring systems are used to detect and identify gases, pharmaceuticals and toxins by measuring the specific absorption bands of methane ( $3.3\ \mu\text{m}$ ),  $\text{CO}_2$  ( $4.6\ \mu\text{m}$ ),  $\text{CO}$  ( $4.2\ \mu\text{m}$ ),  $\text{NO}_x$  ( $6.5\ \mu\text{m}$ ), and many others. Therefore, it is highly desirable to develop efficient mid-IR emitters and detectors, needed to build sensitive mid-IR optical measurement systems.

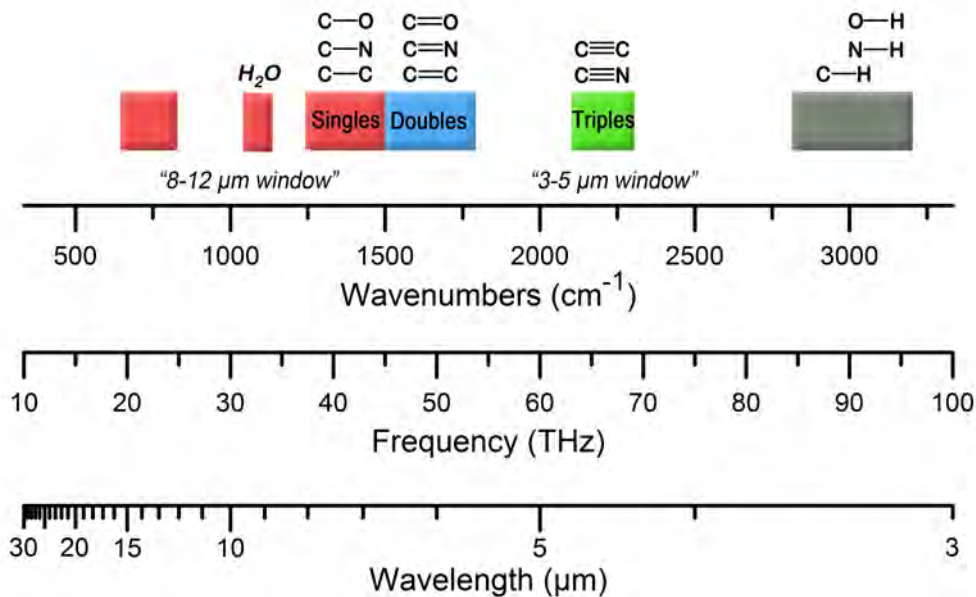


Figure 1.2: Organic compounds in the mid-infrared region. In this spectral range the absorption lines of organic compounds are very specific. Therefore, it is also called the *finger print* region. (Published in [4])

In addition, two atmospheric transmission windows exist ( $3 - 5\ \mu\text{m}$  and  $8 - 12\ \mu\text{m}$ ) that allow free-space optical communication as well as infrared military countermeasure systems. Data transmission speeds up  $2.5\ \text{GBit/s}$  were reported using high-speed modulated mid-IR lasers [5, 6, 7]. However, so far no commercial systems are available and further development of energy efficient sources and sensitive detectors is necessary.

Infrared imaging systems are the driving force behind the development for better mid-IR detectors, pushed forward mainly by the astronomical community and military agencies. Almost 30 years ago the first linear arrays for mid-IR scanning systems were reported [8, 9, 10]. The next generation mid-IR imaging systems were two-dimensional

(2D) pixel arrays, so called focal plane arrays (FPA). Since then the number of pixels has been growing exponentially in accordance with Moore's Law (Fig. 1.3a). Today's mid-IR imaging systems are called third generation FPAs, providing enhanced capabilities like high thermal resolution, high frame rates, multicolor functionality or on-chip signal processing [11]. Megapixel infrared imaging systems are commercially available and frequently used in science and industry (Fig. 1.3b).

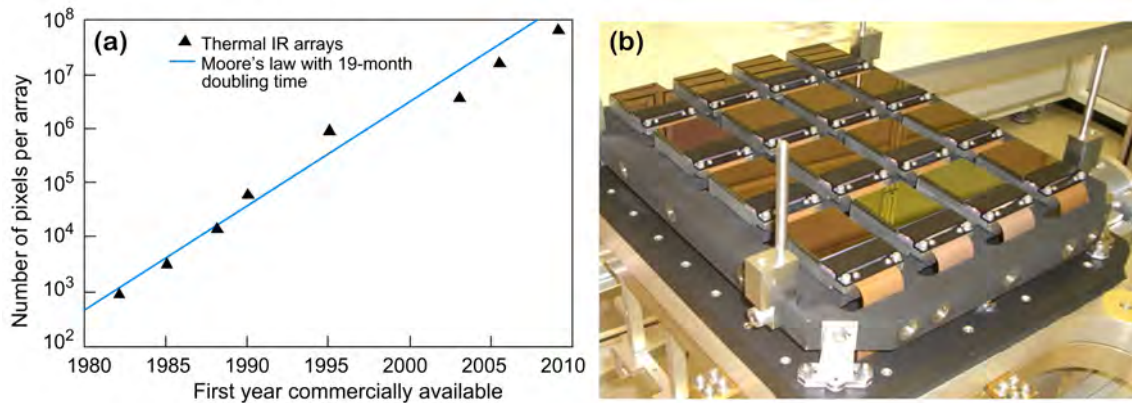


Figure 1.3: State-of-the-art mid-IR focal plane arrays. (a) The number of pixels on a mid-infrared focal plane array has been growing exponentially, in accordance with Moore's Law for almost 30 years. (b) Sensor chip assembly for an infrared telescope, composed by sixteen 2048x2048 MCT mid-infrared focal plane arrays. The detectors will be operated at 72 K and are ready to be placed in the telescope's camera system. (Published in [11])

Similar as in many other scientific fields, the research focus for novel mid-IR optoelectronic systems is on semiconductors, since they allow miniaturization and low-cost fabrication. Unfortunately the same efficient technologies developed for optoelectronic devices in the visible range cannot be applied to devices in the mid-IR. The band gaps of standard semiconductor materials such as Gallium Arsenide (GaAs), Indium Phosphide (InP), or Silicon (Si) are all larger than 1 eV, while the photon energy of mid-IR radiation is much lower (40–400 meV). Therefore, it is not possible to use electron-hole recombination or interband transitions in standard semiconductors for the generation or detection of mid-IR light. The straightforward solution was the development of semiconductors with narrower band gaps. Working mid-IR lasers were shown based on lead salt semiconductors, but the performance is limited by non-radiative Auger recombination, hence efficient operation is possible only at cryogenic temperatures [12, 13]. On the other hand, mid-IR photodetectors fabricated from narrow gap semiconductors present today's most sensitive detectors [11].

**Mid-infrared Photodetectors** Photodetectors in the mid-IR region are generally based on two different detection principles: *thermal detectors* and *photon detectors*.

Thermal detectors measure the temperature change of a small absorber. The temperature change is then converted to an electronic signal. Examples are thermocouples, which make use of the thermoelectric effect, or pyroelectric detectors like Deuterium Triglycin Sulfite (DTGS), that measure the change of electrical polarization. Thermal detectors generally show good sensitivity, but slow photoresponse since a finite volume needs to be cooled or heated entirely. However, they are relatively cheap in production, can be used at room temperature and show a broad well-defined absorption spectrum [14].

Photon mid-IR detectors are fabricated from semiconductors, which exhibit an electronic transition by absorbing the incident radiation. In a narrow band gap material the photons excite electron-hole pairs, which are separated and measured as photocurrent or photovoltage. Examples for the near infrared and parts of the mid-IR spectral range are Indium Gallium Arsenide (InGaAs) photodiodes or Indium Antimonide (InSb) photodetectors. The most widely used detector material for the entire mid-IR spectrum today is Mercury Cadmium Telluride (HgCdTe or MCT). It has many excellent properties such as high sensitivity and fast photoresponse, but faces some drawbacks compared to other semiconductors [15, 16]. The major drawback of MCT is the non-uniformity and hereby low yield in production.

A different physical absorption mechanism for photon detectors is based on intersubband transitions in semiconductor heterostructures. The electronic transitions happen between subbands only in the conduction band or in the valence band. The technology enabling these types of photodetectors is called intersubband optoelectronics.

**Intersubband Optoelectronics** Pronounced quantum effects always occur, when one or more dimensions of a structure approach the characteristic length scale of the elementary excitation. This is called *quantum confinement* and can be in one dimension e.g. in quantum wells (QW), two dimensions e.g. in nanowires (NW) or in three dimensions e.g. in quantum dots (QD). Quantum confinement in semiconductors is achieved by confining electrons (or holes) in potential wells. The characteristic length for electron-hole pairs in semiconductors is in the range of 10 nm. The confinement changes the allowed energy states in the structure and leads to the formation of electronic subbands [17].

With the invention of molecular beam epitaxy (MBE) in 1960 it suddenly became possible to study and exploit quantum confinement effects in semiconductors [18]. In MBE, different materials are deposited in the form of *molecular beams* onto a heated crystalline substrate to grow thin epitaxial layers (Fig. 1.4a).

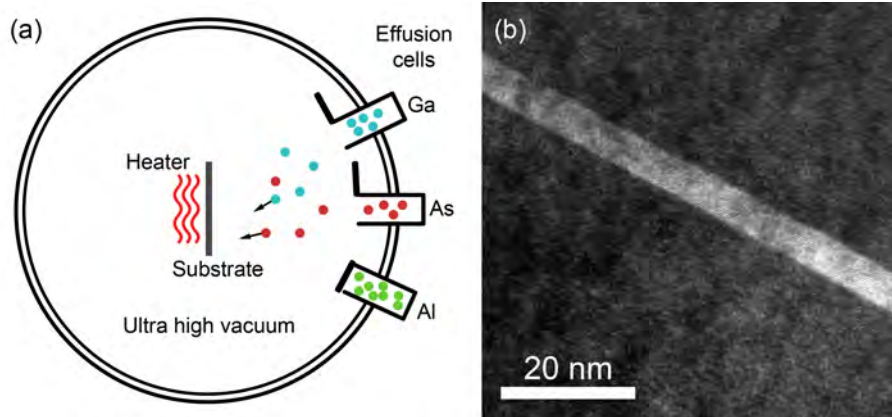


Figure 1.4: Molecular beam epitaxy. (a) Schematic structure of a MBE growth chamber. (b) Transmission electron microscopy image of a MBE grown heterostructure. (Image (b) courtesy of H. Detz, TU Wien)

The molecular beams are usually formed by thermally evaporating high-purity elemental sources. The entire process is performed in an ultra-high vacuum environment. The growth rates are typically on the order of a few  $nm/min$ . The molecular beams can be switched on and off very rapidly, allowing to grow heterostructures with almost atomically sharp transitions from one material to another (Fig. 1.4b).

MBE allows the growth of semiconductor heterostructures with atomic monolayers precision. Subsequent growth of materials with different band gaps creates a *conduction band offset* (and/or valence band offset). The formed potential barriers and wells allow the realization of structures for electron (or hole) confinement, hereby creating subbands in the quantum well (Fig. 1.5). The transitions between these subbands are called intersubband (ISB) transitions.

The possibility to use quantum confinement and ISB transition for novel devices was soon investigated. Kazarinov and Suris proposed already in 1971 an electrically pumped semiconductor laser based on ISB transitions in QWs [20, 21]. The first real device using quantum confinement was the resonant tunneling diode and it was realized in 1974 [22]. To use intersubband transitions for photodetection was first suggested in 1977 by Chang *et al.* [23]. One of the earliest experiments with intersubband transitions was then reported in 1985 [24]. Two years later Levine *et al.* reported the first quantum well infrared photodetector (QWIP) [25]. Electroluminescence from an ISB device was first observed by Helm *et al.* in 1989 [26]. The successful fabrication of an ISB laser presented a greater challenge, since the carrier lifetimes are very short and

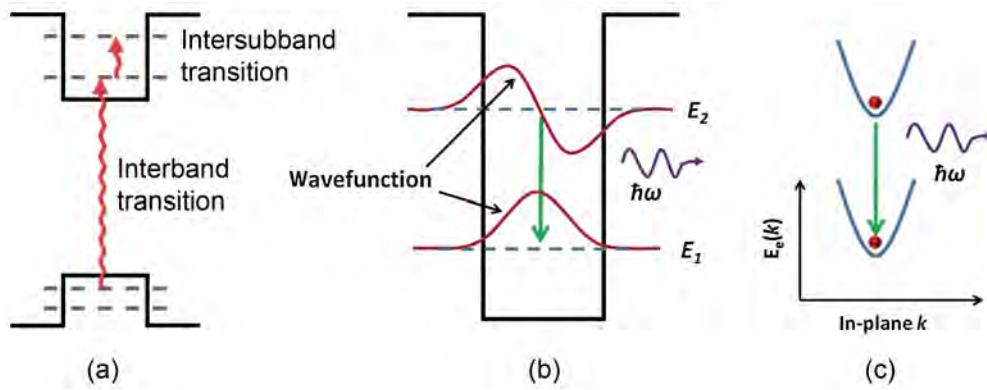


Figure 1.5: Interband and intersubband transitions. (a) An interband transition happens between valence and conduction band. Intersubband transitions occur between two subbands in the conduction band or in the valence band. (b) Two subbands in a quantum well and their electron envelope functions. An intersubband transition is possible only for light with an electric field polarized in quantization direction. (c) In-plane energy dispersion relations of the two subbands. (Images (b) and (c) published in [19])

inversion was difficult to achieve. To realize the first laser based on ISB transitions it took until 1994, when Faist *et al.* reported the first working quantum cascade laser (QCL) [27].

Today, mid-IR lasers are highly developed and commercially available. QCLs operate continuous wave, single mode at room temperature with optical output powers up to several Watts. Recently, a photonic crystal distributed feedback quantum cascade laser emitting at  $4.36 \mu\text{m}$  with a peak output power up to  $34 \text{ W}$  was reported [28]. Advanced resonator designs yielded QCLs with low threshold [29, 30], broadband emission [31, 32], narrow beam surface emission [33], tunable far field pattern [34] or on-chip beam steering capabilities [35, 36], hereby satisfying almost any application requirement.

Intersubband optoelectronic devices have two unique properties, which makes them distinctly different from band gap optoelectronic devices: 1) unipolar carrier transport, which means that only one type of carriers (holes or electrons) contribute to the charge transport and 2) polarization dependence of the electron-photon interaction.

The unipolar character of the carriers generally helps for the design of efficient devices. With only one type of carriers involved, there is no electron-hole recombination at surfaces, which greatly increases the design flexibility for any resonator cavity. Passivation of the exposed semiconductor surface is generally also not necessary. Additionally it allows reusing an electron after the emission of a photon. While an electron-hole pair is lost after recombination and photon emission, an electron can emit as many photons as there are ISB transitions. This concept is intensely used in QCLs, where one electron is emitting one photon per cascade [37, 38].

The polarization dependence of the interaction of electrons with photons originates from a quantum mechanical selection rule. To emit or absorb a photon the electric field needs to be polarized in the quantization direction. The result is, that ISB transitions are principally not allowed when the electric field is polarized in-plane with the quantum well, which is the case for surface-normal incident light. This is acceptable for lasers, which are often fabricated as edge emitters. If surface emission is necessary, it is achieved easily by  $2^{nd}$ -order diffraction gratings [39, 34]. For photodetectors, sensitivity to surface-normal incident light is important, especially since QWIPs are mainly used as FPAs for infrared imaging. This issue is solved by diffracting the light with a grating [40, 41, 42] or simply by random surface roughening [43].

While QCLs are clearly the most advanced lasers for the mid-IR range, this question is still not answered for mid-IR photodetectors. While MCTs provide the highest sensitivity, they lack uniformity and fabrication yield. Operation at wavelengths longer than  $\lambda = 15 \mu m$  is not possible with MCTs. QWIPs on the other hand show excellent uniformity over large areas, but are generally limited to operation at cryogenic temperatures. However, the research on QWIPs and, more generally, quantum confinement infrared photodetectors is ongoing and promising results have been reported.

**Quantum Confinement Infrared Photodetectors** Quantum confinement of carriers in semiconductors leads to the formation of subbands (or sublevels). The transitions between subbands are particularly interesting for optoelectronic applications, because it is possible to fully control the transition energy. After the first successful ISB absorption experiments it soon became clear that this new technology could be used for photodetectors [24]. The first *GaAs/AlGaAs* infrared photodetector based on ISB absorption was demonstrated by Levine *et al.* in 1987 [25]. This QWIP consists of a series of *n*-type doped quantum wells, where the carriers are confined only in one dimension while they can move freely in the other two directions. The operation principle is based on the photoexcitation of confined electrons in the quantum wells. Since the signal is measured as a photocurrent, such detectors are called *photoconductive* QWIPs [44]. Over the last two decades this relatively simple device was intensely studied and optimized [10, 11, 44, 45, 46]. Today, standard QWIPs consisting of simple quantum wells provide detectivities up to  $10^{11} \text{ cm Hz}^{1/2}/W$ , are well understood and commercially available. However, they lack certain properties which are desirable for a photodetector. As mentioned above, the two most critical drawbacks of standard QWIPs are 1) the lack of sensitivity to surface normal incident light and 2) need for operation at cryogenic temperatures to get reasonable signal-to-noise ratios. Therefore, QWIPs generally need to be processed into more complex structures to achieve satisfactory operation. A possible way to overcome these difficulties was presented by the introduction of the quantum dot infrared photodetector (QDIP). In a QDIP, the

carriers are confined in all three dimension, making QDIPs sensitive to surface normal incidence light [47]. Additionally, they promise to operate with less dark current, resulting in higher detector detectivity [47, 48, 49]. The concept of the QDIP was further improved by incorporating the quantum dots into a quantum well, leading to a hybrid structure called quantum dots-in-a-well (DWELL) infrared photodetector. The DWELL structure combines some advantages of the QWIP and the QDIP. A DWELL photodetector is sensitive to surface normal incidence light and, unlike in a QDIP, the energy level of the first excited state can be controlled very well [50, 51]. In recent years, promising results with DWELL devices were reported with superior detectivity and temperature performance compared to QWIPs and QDIPs [52, 53, 54]. A systematic study of state-of-the-art DWELL infrared photodetectors was presented by Barve *et al.*, reporting reasonable performance even at high temperatures [55]. However, the DWELL structure is significantly more complex than QWIPs or QDIPs and there is still a lot of room for improvement.

A different class of QWIP structures is presented by the *photovoltaic* QWIPs, which are based on a different detection principle [56]. A photovoltaic QWIP is designed with a built-in inversion asymmetry acting as an internal electric field. These photodetectors can be operated without a bias voltage, which results in a vanishing dark current. However, the signal generated from a photovoltaic QWIP is much less than from a photoconductive QWIP. The photovoltaic QWIP structure was improved by introducing the four-zone scheme, which further reduces the generated noise [57]. In the end both types of photodetectors have comparable detectivity, but the photoconductive QWIP is generally preferred since it generates larger photocurrents which are easier to amplify. Promising results were reported for an even further advanced type of photoconductive QWIP, the quantum cascade detector (QCD) [58, 59]. QCDs present an interesting approach to detect infrared radiation, but the development of QCDs is still at the beginning.

The research on QWIPs is mainly driven by the development of improved infrared imaging systems. While the first mid-IR cameras were single pixel arrays with an external scanning apparatus, modern FPAs are available with megapixel resolution mounted on integrated readout circuits [60, 61, 62]. Especially large arrays QWIP are advantageous over MCT detectors, since they provide excellent uniformity. When the detectivity reaches levels of about  $10^{10} \text{ cm Hz}^{1/2}/W$ , the FPA performance is usually limited by the uniformity [10]. The latest achievements in FPA research do not only improve detectivity, but add enhanced functionality like multicolor sensitivity [63, 64, 65] or high speed operation [66]. The greater goal for the coming years is something called the *infrared retina*, providing color sensitivity coupled with powerful on-chip signal processing similar to the human eye [67].

Interesting physics as well as potential applications were reported for a two-photon

QWIP. There, the QW is designed to contain two ISB transitions, generating a photocurrent electron only after the absorption of two photons [68]. This device could be operated at room temperature and was used in autocorrelation experiments, which potentially leads to novel pulse characterization methods for optical pulse sources.

An important market for future applications is certainly THz optoelectronics. For this interesting spectral region, neither the laser sources nor the photodetectors are close to a satisfactory operation and only few systems are commercially availability. Respectable results were achieved for THz QWIPs, based on single- or two-photon absorption [69, 70, 71, 72]. However, all these devices need to be operated at liquid helium temperatures, and a lot of progress is necessary before such detectors will be available as compact, reliable systems.

Surface plasmons are known for a long time already, but have recently seen a lot of attention for their fascinating properties in the control of light [73, 74]. Surface plasmon assisted waveguiding as well as enhanced absorption was reported for mid-IR photodetectors [75, 76, 77, 78, 79]. Even a plasmonic mid-IR camera system based on a DWELL photodetector providing enhanced detectivity was recently presented [54].

**Resonant Photodetection** The key element for any photodetector is an absorber, which converts the incoming radiation into a measurable signal. In a QWIP, the photons are absorbed by the confined electrons in the quantum wells. A high absorption will generate a strong photoresponse, which is then measured as photocurrent. Unfortunately, the absorption per quantum well of a standard mid-IR QWIP is below 1% [44]. To achieve reasonable absorption values, QWIPs require many quantum wells. Typical QWIPs are grown with 10 to 100 QWs, depending on the absorption wavelength, optical coupling scheme and application requirements. A large number of QWs ( $N$ ) is desirable, since the QWIP detectivity is proportional to  $\sqrt{N}$ . However, the growth of the heterostructure becomes more challenging with increasing thickness, therefore this approach is limited.

An elegant way to improve the performance of a photodetector without altering its electrical properties is by embedding it into a resonant cavity. Photons inside the cavity exhibit a longer lifetime. This increases the absorption probability and hereby the quantum efficiency of the detector. This principle is called resonant cavity enhancement (RCE) and is successfully used in photodetectors and spatial light modulators for optical telecommunication wavelengths [80, 81, 82]. A simple model for a resonant cavity enhanced photodetector consists of an absorbing region embedded in a Fabry-Perot resonator (Fig. 1.6a). The enhancement is frequency dependent and is influenced by the absorption coefficient  $\alpha$  and the reflectivities  $R_1$  and  $R_2$ . The higher the reflectivity, the higher is the enhancement at resonance, the narrower is the peak width and the lower the off-resonance quantum efficiency (Fig. 1.6b). This leads to a gain-bandwidth

trade-off, which has to be considered. Depending on the application, a narrow absorption peak width can be desirable or not. If a narrower absorption bandwidth is desirable or at least acceptable, RCE can be a powerful tool to improve detector performance. Mid-IR photodetectors implementing RCE were reported [83, 84, 85, 86] and are an on-going research topic.

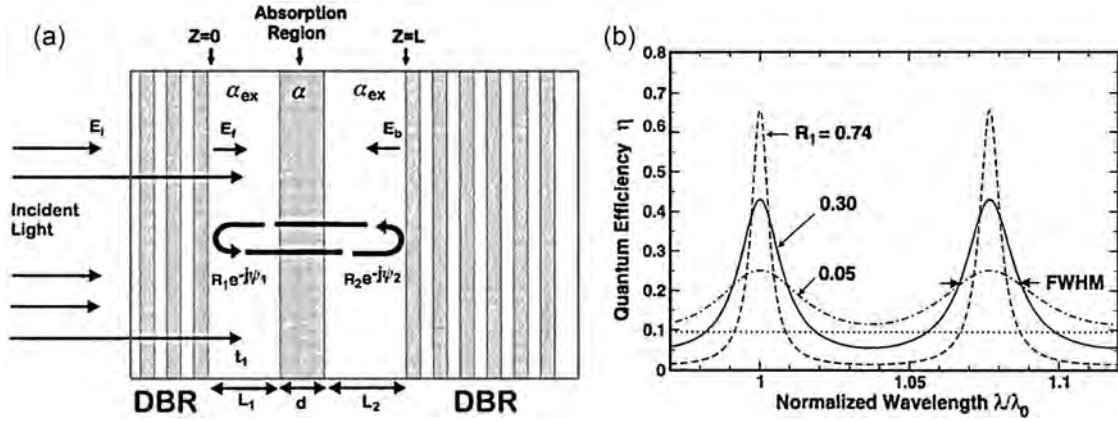


Figure 1.6: Resonant cavity enhancement. (a) Analytical model for a RCE photodetector with distributed Bragg reflectors (DBR) as mirrors. (b) Wavelength dependence of the quantum efficiency  $\eta$  for a RCE photodetector for different mirror reflectivities  $R_1$ . (Images published in [82])

## 1.2 Photonic Crystals

A photonic crystal (PC) is a structure with a periodic modulation of the refractive index. It is well known, that waves propagating through media with a periodic modulation of the material properties behave fundamentally different than waves in homogenous media [38]. These effects dominate the physical properties of the medium, particularly when the wavelength is on the scale of the modulation period. This fact is well known from solid-state physics and determines the physical properties of metals, semiconductors and insulators. This periodic modulation of the electronic potential is responsible for the formation of energy bands, band gaps and effective masses [87, 38].

Light in photonic crystals behaves in many ways similar to electrons in semiconductors. The periodic modulation gives rise to peculiar optical properties like photonic bands and photonic band gaps. These fascinating features enable the creation of new optical materials with superior properties and unforeseen novel applications [88, 89, 90, 91].

The simplest possible photonic crystal is a one-dimensional (1D) modulation of the refractive index. Such dielectric multi-layer stacks are known for a long time already as Bragg reflectors, and it is well understood that some frequencies are transmitted while others are reflected (Fig. 1.7a). Bragg mirrors are widely used to create optical cavities, confining the optical mode to a finite volume. This principle can be generalized to 2D and three-dimensional (3D) structures, allowing high mode confinement (Fig. 1.7b and 1.7c). Although the properties of 1D multi-layer stacks were known for over one century, it took until 1972 when Bykov proposed the use of periodic structures, that would serve to inhibit certain electromagnetic frequencies [92, 93]. Such a structure will suppress spontaneous emission, since no optical modes with the appropriate energy are available. These structures became known as photonic band gap (PBG) structures, since they exhibit frequency gaps in their dispersion relation.

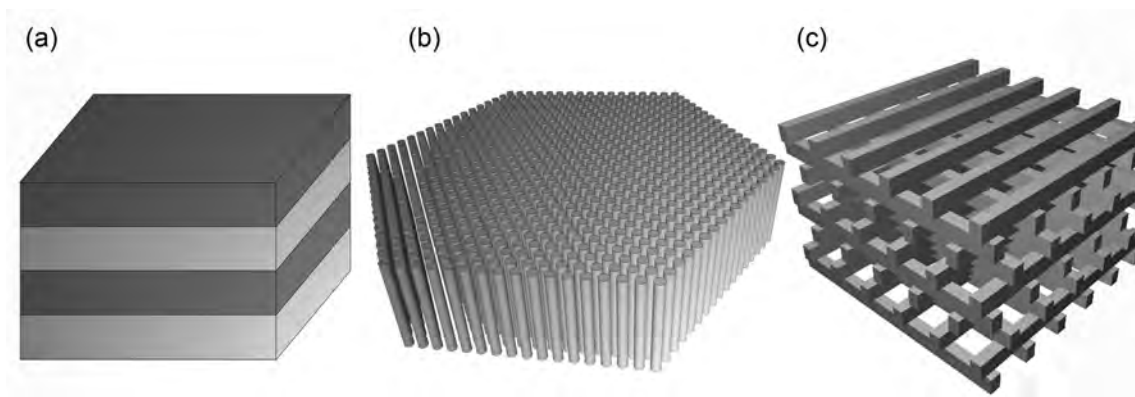


Figure 1.7: Photonic crystal structures. (a) A dielectric layer stack (or one-dimensional photonic crystal). (b) Two-dimensional photonic crystal, consisting of an array of dielectric cylinders. (c) “Woodpile” three-dimensional photonic crystal structure. (Image (c) published in [91])

The enormous interest in photonic crystals we experience today started with the papers of Yablonovitch [94] and John [95]. Yablonovitch proposed a three-dimensional periodic dielectric structure with a photonic band gap, which overlaps with the electronic band gap, hereby inhibiting spontaneous emission. John discussed the strong localization of light in strongly scattering dielectric media. After these first results, the theorists developed methods for the systematic investigation of electromagnetic waves in periodic media [96, 97]. In particular the plane wave expansion method (PWEM) became very important, since it allows accurate simulation of the photonic crystal dispersion relation while being computational efficient [98, 99, 100].

The first attempt to realize a PBG structure was made by Yablonovitch and Gmitter in 1989, who fabricated a face-centered-cubic lattice for microwave frequencies. However,

they did not observe a complete band gap [101]. Two years later they fabricated the same lattice structure by drilling holes into dielectric material. Transmission measurements for this new structure showed a complete band gap [102].

To get to higher frequencies, it was necessary to scale down the dimension of the photonic crystals. New structures were proposed, which also exhibit a complete photonic band gap. With a so-called “woodpile” photonic crystal structure (Fig. 1.7c), that was fabricated by stacking pre-patterned silicon wafers, a complete band gap was observed in the THz frequency range [103]. By further miniaturization, a “woodpile” photonic crystal was fabricated by Lin *et al.* with a minimum feature size of  $\sim 180\text{ nm}$  and a photonic band gap centered at  $\lambda = 1.6\ \mu\text{m}$  [104]. To get to the visible frequency range, researches tried to use self-organized structures with 3D colloidal photonic crystals, knowing that similar structures already exist in nature [105, 106].

**2D Photonic Crystals** A photonic crystal is a periodic structure, which in a strict definition means that it should extend to infinity in every dimension. Clearly this is not possible, otherwise the entire universe would have to be filled with periodically modulated dielectric material. Even with finite dimensions, the fabrication of 3D photonic crystals presents a huge challenge. Interacting with a confined volume inside a 3D photonic crystal is practically almost impossible. For this reason, researchers were investigating lower-dimensional photonic crystal structures, checking if these new structures would still preserve the desirable optical properties like photonic band gaps. Dielectric multi-layer stacks were already known to exhibit photonic band gaps, even though it was never called like this before. Joannopoulos *et al.* introduced 2D planar photonic crystal waveguides, which could guide light even around sharp bends with minimal losses [107]. The design was based on a 2D photonic crystal, consisting of infinitely long dielectric pillars with line defects, acting as waveguides (Fig. 1.7b) [108].

Based on these findings, all kinds of new applications were investigated like low-loss photonic waveguides and high-Q cavities [109, 110, 111, 112], all optical switches [113] and even optical logic gates [114]. It was found, that the photonic crystal did not have to be infinitely large in the modulation direction to produce the desirable effects, since the electromagnetic field decays rapidly within several lattice periods. However, in principle a “real” 2D photonic crystal still is infinitely large perpendicular to the confinement direction. The only physically existing structures, that approximately fulfill this requirement, are photonic crystal fibers for optical telecommunication (Fig. 1.8a). Photonic crystal fibers were developed to exhibit less dispersion and lower absorption than standard optical fibers, and are commercially available today [115, 116].

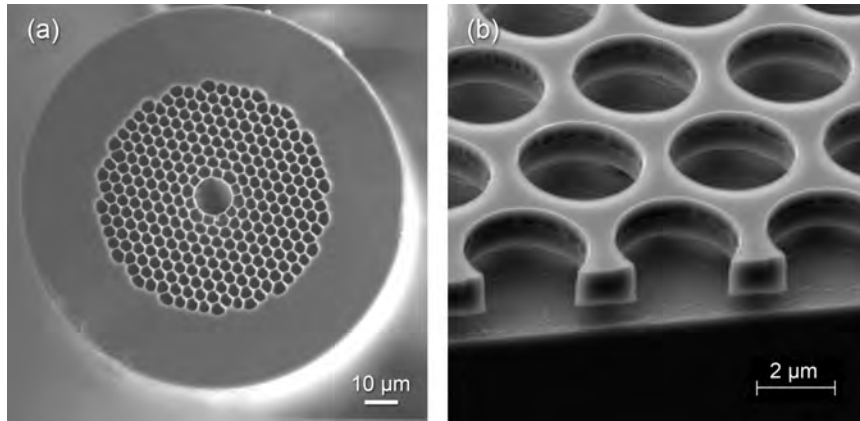


Figure 1.8: SEM images of 2D photonic crystals. (a) Photonic crystal fiber with a hollow-core waveguide. (b) Photonic crystal slab, fabricated from a GaAs heterostructure. (Image (a) published in [116], image (b) published in [117])

For practical reasons, the most important photonic crystal structures today are photonic crystal slabs (PCS) [118, 119, 120]. They are periodic in two dimensions, whereas in the third dimension they have a finite height (Fig. 1.8b). Since PCSs are much easier to fabricate, they have attracted a lot of attention, from research institutions but also from industry. Like infinitely high 2D photonic crystals, PCSs can have a band gap in the modulation direction [121]. They support guided modes, which do not couple to any free-space modes [122], and radiative modes that can couple to external electromagnetic fields [123]. These properties made photonic crystal slabs useful for countless applications.

High-Q cavities were presented using waveguides structures in PCSs with Q-factors up to 2800 [124]. By further improving the cavity design, ultra high-Q cavities with Q-factors up to  $\sim 10^6$  became possible [125, 126]. The possibility to fully design the dispersive properties of the material opened the way for *slow light* generation with PCS waveguides [127]. In these slow light waveguides, the interaction with the surrounding material is hugely increased, such that even third-order nonlinear effects can be observed (Fig. 1.9) [128, 129].

An exciting and long desired application finally became possible by combining the theories of photonic crystals, transformation optics and conformal mapping: *Invisibility cloaking*. It is possible to precisely control the flow of electromagnetic waves, an object can be hidden in some finite volume by bending the light around the hidden space.

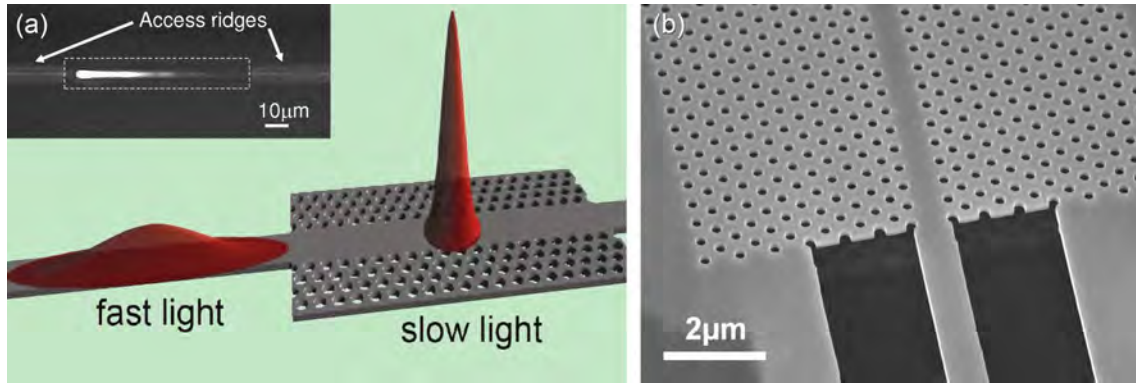


Figure 1.9: Slow light in silicon photonic crystal waveguides. (a) Illustration of spatial pulse compression. Inset: Green light emission from a PC waveguide, created by nonlinear interaction. (b) SEM image of the PC waveguide. (Published in [129])

The distortion of the electromagnetic fields is represented as a coordinate transformation, which is then used to generate values of electrical permittivity and magnetic permeability [130].

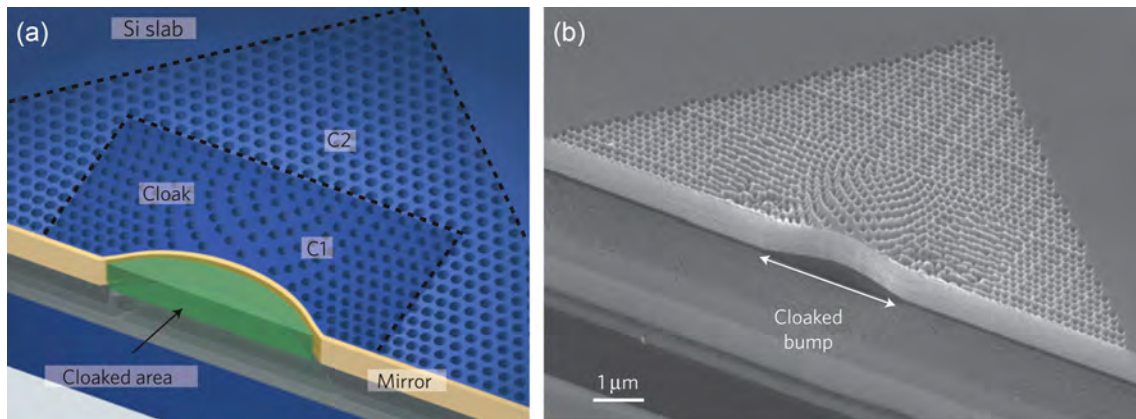


Figure 1.10: Invisibility cloaking. (a) Schematic device structure of the optical carpet cloak. It is designed to conceal an object that is placed under a curved reflecting surface using quasi-conformal mapping. (b) SEM image of the carpet cloak. (Published in [131])

A special case of cloaking is presented by *carpet cloaking*, where an object is placed under a curved reflecting surface. The curved surface is concealed by imitating the reflection of a flat surface with quasi-conformal mapping (Fig. 1.10). With this method, it was possible realize a carpet cloak, consisting only of isotropic dielectric materials, with a cloaking bandwidth from 1400 – 1800 nm [131, 132].

**Photonic Crystal Light Emitters** In recent years, light emitting diodes (LED) have revolutionized energy-efficient lighting and will most likely replace conventional illumination with light bulbs entirely. LEDs have the potential to become highly efficient light sources, because the internal quantum efficiency of LEDs is close to unity. However, the total efficiency is significantly lower, limited by total internal reflection and absorption in the substrate. This topic is particularly important for Gallium Nitride (GaN) LEDs, which are used for the generation of full spectrum white light [133]. In the past, 2D PCs have been successfully used to overcome the low extraction efficiency of LEDs [134, 135, 136, 137]. The PC layer provides excellent optical mode control compared to conventional LEDs, efficiently coupling PC modes to external free-space modes with an efficiency up to 73% [138]. Although these results are promising, the technology is complex and has to compete with much simpler techniques like surface roughening [139, 140] or pyramidal structures [141] for efficient light out-coupling.

Very promising results were reported for lasers, designed with a PC resonator. Photonic crystals can be used in two different configurations to work as a laser resonator: 1) The PC is designed to exhibit a photonic band gap at the desired laser frequency, acting as excellent mirrors for a tiny laser cavity (Fig. 1.11).

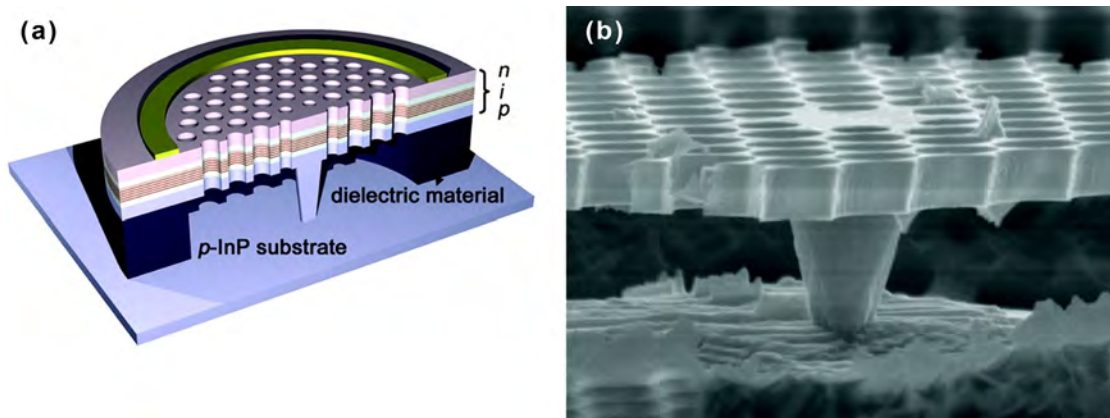


Figure 1.11: Photonic crystal laser. (a) Schematic device structure. The photonic crystal is underetched to limit the current flow to the cavity region. (b) SEM image of the photonic crystal active area. (Published in [142])

Such lasers have the potential for ultra-low threshold currents, but current supply is generally a problem [143, 144, 142]. 2) The PC is designed to show a photonic flat band region in the gain spectral region of the laser material. In this case the optical mode is extended over the entire photonic crystal, and the whole PC area emits radiation [145, 146, 147]. For such PC lasers surface-emission continuous wave operation at room temperature was reported [148].

PC lasers can provide additional functionality. The sensitivity of the PC resonant properties to the refractive index of the surrounding medium makes them ideal for chemical sensing [149, 150, 151]. With clever PC design and a deep understanding of the PC mode propagation, it is even possible to realize electronically controlled on-chip beam steering of a PC laser [152]. In the past, most PC lasers were demonstrated working at visible or near-IR frequencies, but now researchers are also focusing on PC lasers for longer wavelengths. For the mid-IR spectral range, PC-QCLs were reported which show surface emission [153, 154] or can provide optical output powers up to 34 W at room temperature [28]. Recently, PC lasers were also reported in the THz spectral range [155, 156, 157].

**Photonic Crystal Photodetectors** The fascinating property of photonic crystals to control the flow of electromagnetic waves makes them also interesting for photodetectors. PCs can be used to diffract the light such, that it propagates along the absorption region, increasing the absorption length. Additionally, the resonant properties of photonic crystals can be used to increase the photon lifetime in the absorption region. This concept was already briefly discussed as resonant cavity enhancement in the last section. The resonant features of photonic crystals were successfully exploited to enhance QDIPs in the mid-IR region [158] and photodiodes in the near-IR spectral range [159]. The first QWIP, that was combined with a photonic crystal, was reported by Schartner *et al.* [160]. Since QWIPs are insensitive to surface-normal incidence radiation, the PC fulfilled two tasks at once: 1) diffraction of the light to match the necessary polarization of the light and 2) resonant cavity enhancement. Since the implemented photonic crystals were 2D-PCs, the vertical mode confinement had to be taken care of separately. This was achieved by surface-plasmon waveguiding [161, 162, 54]. The PC can also be used to increase functionality. The narrow linewidth of the resonances was used to create wavelength-selective photodetectors, where the PC acts as a filter [163, 164]. A PC photodetector can also be used as a tool for direct band structure mapping to analyze the PC properties [165, 166, 167]. Even defect modes in PC structures can be studied with this versatile tool [168, 169]. Increased photodetector performance was shown by resonant cavity enhancement, using either the entire photonic crystal [170, 78] or only PC defect modes [171, 172].

## 2 Quantum Well Infrared Photodetectors

QWIPs generally consist of a series of quantum wells. The most common type of QWIP is the photoconductive QWIP, where a bias voltage is applied to the detector and the signal is measured as photocurrent. This is in contrast to the photovoltage QWIP, where the detector is operated unbiased and the signal is measured as photovoltage. Since the research conducted for this thesis is based on photoconductive QWIPs, these will be discussed in this section in greater detail. A good introduction to quantum well infrared photodetectors can also be found in *Quantum Well Infrared Photodetectors: Physics and Applications* by H. Schneider and H. C. Liu [44].

The basic elements of a QWIP are quantum wells, which are separated by barriers (Fig. 2.1a). Well width and barrier height are designed to exhibit one confined ground state inside the well and a first excited state which aligns with the top of the barrier. The barriers are made sufficiently thick to prevent tunneling between the wells. The wells are  $n$ -doped such that the ground state is filled with electrons. Typical QWIPs consists of 20 to 50 quantum wells. When a bias voltage is applied to the QWIP, the entire conduction band profile is tilted. Without excitation the electrons in the quantum wells will just stay in the ground state. When the electrons are excited by a suitable light source, they can escape into the continuum. At the surface of the QWIP, the electrons are extracted via the metal contacts and measured as photocurrent (Fig. 2.1b).<sup>1</sup>

A common material system for QWIPs is gallium arsenide as well material and aluminum gallium arsenide (AlGaAs) as barrier material. The choice of the material system depends of the intended application and on the wavelength range. All QWIPs used for the research presented here were based on the GaAs/AlGaAs material system and designed for a wavelength range around  $8\ \mu\text{m}$ .

---

<sup>1</sup>QWIPs, that are designed in the conduction band containing quantum wells filled with electrons are called  $n$ -type QWIPs. It is also possible to design a QWIP in the valence band with quantum wells, that are filled with holes. Such a QWIP is then called  $p$ -type. However,  $p$ -type QWIPs are only of minor importance, since the mobility of the holes is low and the performance limited.

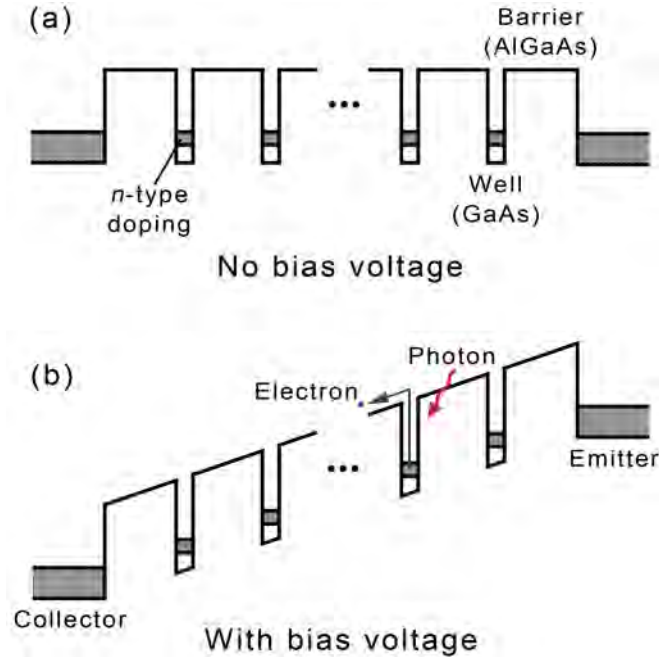


Figure 2.1: Conduction band profile of an  $n$ -type photoconductive QWIP. (a) The QWIP consists of a series of quantum wells with electric contacts on top and bottom. Without excitation the electrons in the quantum wells stay in the ground state. (b) When a bias voltage is applied, the conduction band profile is tilted. Excited electrons are extracted via the contacts and measured as photocurrent. (Published in [44])

## 2.1 Electronic Intersubband Transitions

The electronic transition between confined states in a quantum well (or other low-dimensional quantum confined structure) is called an intersubband transition (ISBT). The following introduction will focus on ISBTs in QWs, in particular transitions in the conduction band (CB). For a detailed discussion of the physics in low-dimensional semiconductor structures refer to [173, 37, 38].

The electronic states in quantum confined structures can be found by solving Schrödinger's equation. A good model for the CB in GaAs/AlGaAs heterostructures is the effective mass approximation under consideration of only a single band [44]. Within this model, the wave functions are described as envelope functions, which represent the slowly varying mesoscopic part of the locally strong oscillating microscopic wave functions. This is possible, because the quantum well dimensions are significantly larger than the semiconductor crystal lattice constant (e.g.  $0.565 \text{ nm}$  in GaAs).

The Schrödinger equation then reads

$$-\vec{\nabla} \frac{\hbar^2}{2m^*} \vec{\nabla} \Psi + V\Psi = E\Psi$$

where  $\hbar = \frac{h}{2\pi}$  with  $h = 6.62606957 \times 10^{-34} Js$  being the Planck constant,  $m^*$  is the effective mass,  $V$  is the potential of the CB edge,  $\Psi$  is the wave function and  $E$  is the energy of the electron<sup>2</sup>. Defining the confinement direction of the quantum wells as the  $z$ -axis, the effective mass  $m^*$  and the potential  $V$  depend only on  $z$ . In this case the wave function is separable into an in-plane part  $\psi^{\parallel}(x, y)$ , depending on  $(x, y)$ , and an out-of-plane part  $\psi^{\perp}(z)$ , depending only on  $z$ .

$$\Psi(\vec{r}) = \psi^{\parallel}(x, y) \psi^{\perp}(z)$$

The in-plane component  $\psi^{\parallel}(x, y)$  represents the 2D movement of the electrons within a subband of the heterostructure. The solutions are simply plane waves with

$$\psi_{\parallel} \sim e^{i\vec{k}_{\parallel}\vec{r}_{\parallel}} \quad \text{and} \quad E_{\parallel} = \frac{\hbar^2 k_{\parallel}^2}{2m^*}$$

where  $\vec{k}_{\parallel}$  is the in-plane wave vector. The out-of-plane component  $\psi^{\perp}(z)$  describes the quantized electron states in the heterostructure, which are found by solving the much simpler one-dimensional Schrödinger equation

$$-\partial_z \frac{\hbar^2}{2m^*(z)} \partial_z \psi^{\perp}(z) + V(z)\psi^{\perp}(z) = E_{\perp}\psi^{\perp}(z)$$

The boundary conditions at the heterostructure interfaces require that the wave function is continuous and that the electron momentum is conserved. Since in general each material of the heterostructure has a different effective mass  $m^*$ , the boundary condition are

$$\psi_a^{\perp} = \psi_b^{\perp} \quad \text{and} \quad \frac{1}{m_a^*} \partial_z \psi_a^{\perp} = \frac{1}{m_b^*} \partial_z \psi_b^{\perp}$$

where  $a$  and  $b$  are two types of semiconductor crystal in the heterostructure. For the case of a single QW between two infinitely high barriers, the solutions are

$$\psi_n^{\perp} \sim \sin\left(\frac{\pi n z}{L_w}\right) \quad \text{and} \quad E_{\perp, n} = \frac{\hbar^2}{2m^*} n^2 \frac{\pi^2}{L_w^2}$$

---

<sup>2</sup>The effective mass of electrons in GaAs  $m_{GaAs}^* = 0.067 m_0$  is significantly lower than the mass of a free electron  $m_0 = 9.10938 \times 10^{-31} kg$ .

$$\text{for } \begin{cases} V = 0 & \text{when } 0 \leq z \leq L_w \\ V = \infty & \text{elsewhere} \end{cases}$$

where  $n$  is a positive integer,  $m^*$  is the effective mass in the well and  $L_w$  is the well width. Knowing this, the reason for the term *subband* becomes obvious. Electrons in a quantum well are confined in one dimension, but can move freely in the other two dimensions. For each confined state electrons can exhibit any in-plane momentum in the subband, having a total energy of  $E(k_{\parallel}) = E_{\perp,n} + E_{\parallel}$ . The ISBT energy from state  $\langle n \rangle$  to state  $\langle n' \rangle$  is given by  $E_{n'} - E_n$ .

The probability for an ISBT from state  $\Psi_i$  to  $\Psi_f$  is calculated using Fermi's golden rule

$$W = \frac{2\pi}{\hbar} \sum_{f,i} |M|^2 (f_i - f_f) \delta(E_f - E_i - \hbar\omega) \quad (2.1)$$

where  $W$  is the transition rate (probability of a transition per unit time),  $f_i$  and  $f_f$  are the Fermi factors, and  $\omega$  is the angular photon frequency.  $M$  is the transition matrix element between the state  $\Psi_i$  and  $\Psi_f$ , which is defined as

$$M = \langle \Psi_f | \hat{H}_{per} | \Psi_i \rangle$$

where  $\hat{H}_{per}$  is the perturbation operator. The matrix element  $M$  determines the ISB absorption and is a measure for the coupling strength between the initial and final state. The derivation of the perturbation operator  $\hat{H}_{per}$  and the corresponding matrix element can be found in [174, 37]. For an ISBT between confined states in a quantum well, the matrix element reads

$$M \approx \frac{e}{m^*} \left( \frac{\hbar}{2\epsilon_0 n_{mat} \omega c} \phi \right)^{1/2} \delta_{k_{\parallel}^i, k_{\parallel}^f} \hat{\epsilon} \cdot \vec{e}_z \langle \Psi_f | p_z | \Psi_i \rangle \quad (2.2)$$

where  $\epsilon_0$  is the vacuum permittivity,  $n_{mat}$  is the material refractive index,  $\omega$  is the angular photon frequency,  $\phi$  is the incident photon flux,  $\hat{\epsilon}$  is the polarization unit vector of the incident radiation,  $\vec{e}_z$  is the unit vector in  $z$ -direction and  $p_z$  the electron momentum operator in  $z$ -direction. The inner product  $\hat{\epsilon} \cdot \vec{e}_z$  is particularly interesting, as it becomes zero if the polarization of the electric field is in-plane with the quantum well. This causes that light is absorbed or emitted only if the electric field is polarized in quantization direction. This fact is known as the *ISBT selection rule* [175, 37].

**Intersubband Absorption Measurements** Direct measurement of ISBTs is possible e.g. by optical transmission spectroscopy on quantum well samples. Transmission mea-

measurements are usually performed by taking a transmission spectrum and normalizing it by a reference. Here the ISBT selection rule helps in acquiring a valid reference measurement. The quantum wells are illuminated by linear polarized light such that once the electric field is perpendicular and once it is in-plane with the quantum wells (Fig. 2.2a). Since in-plane polarized light is not absorbed, it serves as a reference spectrum. Normalization of the absorption spectrum by the reference spectrum then yields the intersubband absorption spectrum (Fig. 2.2b).

For practical reasons, such ISB absorption measurements are usually performed by shining the light onto the QWs under an angle of incidence of about  $45^\circ$ . The polarization of the light can be adjusted such that the electric field in confinement direction of the quantum wells is zero or maximum. The maximum value depends on the incident field strength and on the angle of incidence. It is common in the ISB community to call the polarization with maximum electric field in confinement direction transverse-magnetic (TM) polarization, since there is no magnetic field component in confinement direction of the quantum well. Analogously, the polarization with zero electric field in confinement direction is called transverse-electric (TE) polarization.<sup>3</sup>

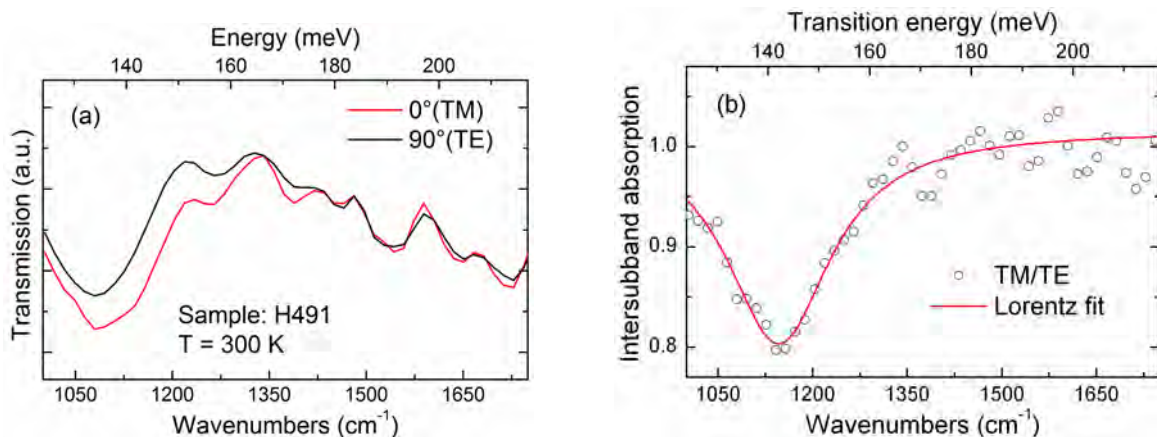


Figure 2.2: Measured intersubband absorption spectrum of a quantum well sample. (a) Transmission spectra measured with TM-polarized and TE-polarized light. (b) Intersubband absorption spectrum, calculated by normalization of the TM-polarized absorption spectrum by the TE-polarized absorption spectrum. The measured sample consists of 40 doped quantum wells with  $4.5 \text{ nm}$  GaAs wells width and  $45 \text{ nm}$   $\text{Al}_{0.3}\text{Ga}_{0.7}\text{As}$  barrier width.

<sup>3</sup>The naming convention for light polarization in the ISB community can sometimes be misleading. It should be noted, that electromagnetic plane waves in free-space are always transverse-electromagnetic (TEM) waves. The notation TM-polarization or TE-polarization refers to the direction transverse to the plane of incidence, but does not reflect the propagation properties of the wave itself. Inside a waveguide the situation gets even more complex.

## 2.2 Photocurrent

The fact, that electrons in a quantum well can be excited by the absorption of photons is the basic element of a QWIP. However, to externally measure a photocurrent the electrons need to be extract by applying an electric field to the quantum well. The efficiency of this absorption and extraction process depends on various parameters, which will be discussed here.

Assuming that the detector is illuminated with a photon flux  $\phi$  (number of photons per unit time), the photocurrent  $I_{ph}$  is simply

$$I_{ph} = e\phi\eta g_{ph} \quad (2.3)$$

where  $e$  is the elementary charge,  $\eta$  is the absorption efficiency and  $g_{ph}$  is the photoconductive gain.  $\eta$  and  $g_{ph}$  are the probabilities for a photon to add an electron to the photocurrent.  $\eta$  represents the optical part of the conversion process, while  $g_{ph}$  depends on the electronic transport properties.

The absorption efficiency  $\eta$  depends on the coupling efficiency of light into the detector and on the transition matrix element  $M$ . The light coupling scheme is a key factor affecting QWIP performance and will be covered in detail in the following sections. The easiest way to couple light into a QWIP is by illumination under a  $45^\circ$  angle of incidence through a wedged facet. A typical photocurrent spectrum of a QWIP for such a configuration is shown in figure 2.3. The drawback of this light coupling scheme is that it does not permit surface-normal incident detection and uses only half of the incident optical power.

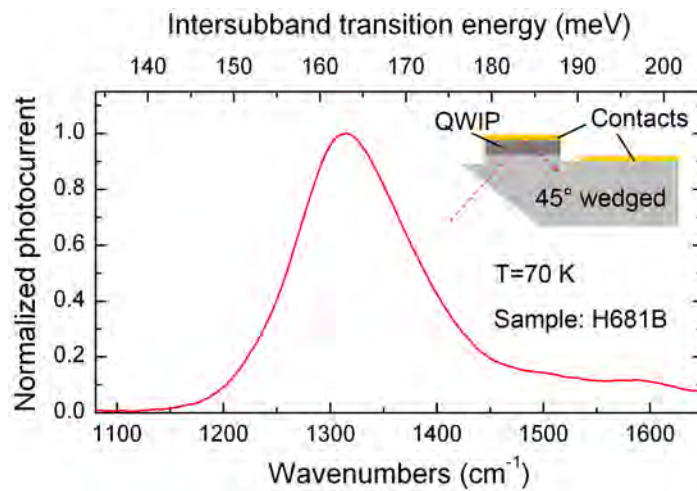


Figure 2.3: Typical photocurrent spectrum of a QWIP. (Inset): The detector is illuminated through a  $45^\circ$  wedged facet, hereby providing an electric field with the necessary polarization to cause an ISBT.

### 2.2.1 Absorption Efficiency

One can calculate the absorption efficiency  $\eta^{(1)}$  for a single quantum well from the intersubband transition rate  $W$

$$\eta^{(1)} \equiv \frac{W}{\phi A \cos \theta}$$

where  $A$  is the detector area and  $\theta$  is the angle of incidence with respect to the growth axis. Assuming weak excitation and low temperature, the Fermi factors become  $f_i \approx 1$  and  $f_f \approx 0$ . In this case the carrier concentration in the ground state  $n_{2D}$  only depends on the doping density  $N_D$  (assuming all dopants are ionized) and  $n_{2D}$  is simply

$$n_{2D} = N_D A$$

Using equations 2.1 and 2.2 the absorption efficiency  $\eta^{(1)}$  can be written as

$$\eta^{(1)} = \frac{e^2 \hbar}{4\epsilon_0 n_{mat} m^* c} \frac{\sin^2 \theta}{\cos \theta} N_D A f \delta(E_f - E_i - \hbar\omega) \quad (2.4)$$

where the oscillator strength  $f$  is defined as

$$f \equiv \frac{2}{m\hbar\omega} |\langle \Psi_f | p_z | \Psi_i \rangle|^2$$

To model the finite line width of an intersubband transition (caused by the finite life time in the excited state), the  $\delta$ -function in equation 2.4 is substituted by a Lorentzian

$$\delta(E_f - E_i - \hbar\omega) \rightarrow \frac{1}{\pi} \frac{\Delta E}{(\hbar\omega - (E_f - E_i)) + \Delta E^2}$$

where  $\Delta E$  is the half width at half maximum of the Lorentzian line shape. Finally the absorption efficiency for a single quantum well is given by

$$\eta^{(1)} = \frac{e^2 \hbar}{4\epsilon_0 n_{mat} m c} \frac{\sin^2 \theta}{\cos \theta} N_D A f \frac{1}{\pi} \frac{\Delta E}{(\hbar\omega - (E_f - E_i)) + \Delta E^2} \quad (2.5)$$

The total absorption efficiency  $\eta$  of a quantum well stack consisting of  $N$  quantum wells is then in good approximation

$$\eta = N \eta^{(1)} \quad (2.6)$$

Typical values for the absorption efficiency per quantum well  $\eta^{(1)}$  in standard QWIPs are below 1%. The calculated absorption efficiency for a single *GaAs/AlGaAs* QW for different well widths is shown in Fig. 2.4.

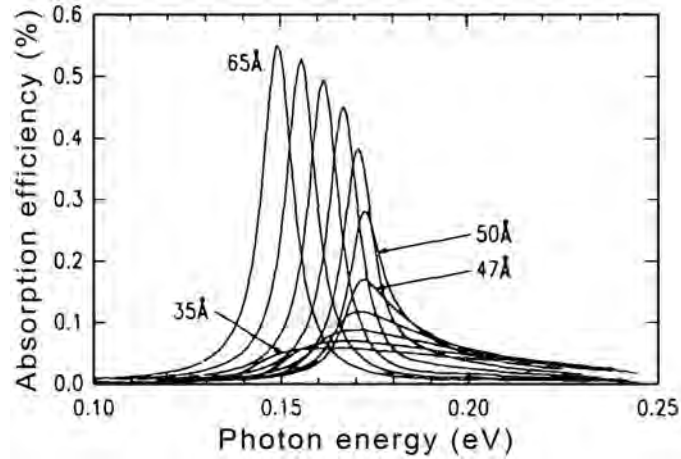


Figure 2.4: Calculated absorption efficiency for one well  $\eta^{(1)}$  for different well widths. QW material compositions are *GaAs/Al<sub>0.33</sub>Ga<sub>0.67</sub>As*, carrier density in the well is  $9 \times 10^{11} \text{ cm}^{-2}$ . (Published in [176])

## 2.2.2 Photoconductive Gain

The photoconductive gain  $g_{ph}$  is the probability that an excited electron contributes to the photocurrent. Although it might be counterintuitive at first, it is possible that  $g_{ph}$  becomes larger than one. Whenever an electron is excited and extracted as photocurrent, an extra electron is injected from the contact to balance the loss of electrons from the quantum well. In general the capture probability  $p_c \leq 1$  and the injected electrons sometimes pass over the quantum well. Therefore, more electrons need to be injected to balance the for the extracted electrons and  $g_{ph}$  can become larger than one (Fig. 2.5).

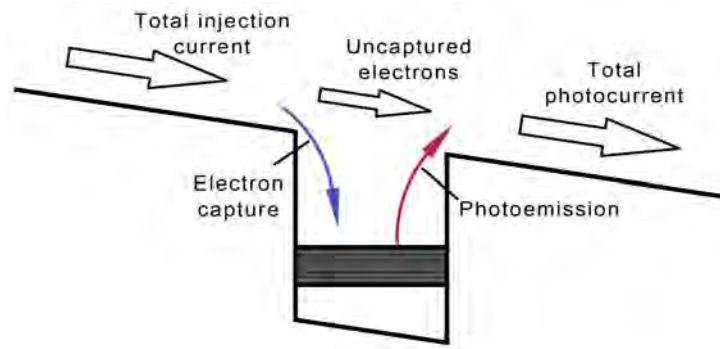


Figure 2.5: Photoconductive gain. To balance the loss of electrons from the quantum well, electrons are injected from the top emitter contact. Since in general the capture probability  $p_c \leq 1$ , extra electrons need to be injected and the total photocurrent can become larger than only the photoemission current.

The exact value of  $g_{ph}$  is determined by the ratio of capture probability  $p_c$  and escape probability  $p_e$

$$g_{ph} = \frac{p_e}{N p_c}$$

where  $N$  is the number of quantum wells. The number of quantum wells appears only in the denominator, as it obviously increases the capture probability  $p_c$ , but not the escape probability  $p_e$ . The escape probability  $p_e$ , on the other hand, depends on the ISB transition design (Fig. 2.6).

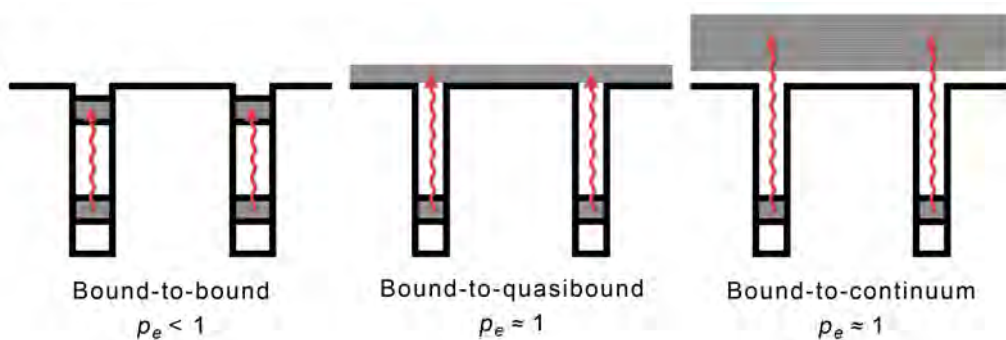


Figure 2.6: The escape probability  $p_e$  of an excited electron from the quantum well depends on the ISB transition design.

The escape probability  $p_e$  for an excited electron from the well into the continuum is given by

$$p_e = \frac{\tau_{relax}}{\tau_{relax} + \tau_{escape}}$$

where  $\tau_{relax}$  is the intersubband relaxation time and  $\tau_{escape}$  is the escape time. Similarly the capture probability reads

$$p_c = \frac{\tau_{trans}}{\tau_{trans} + \tau_c}$$

where  $\tau_{trans}$  is the transit time to across one quantum well region (well + barrier) and  $\tau_c$  is the capture time. If the intersubband transition is designed as a bound-to-continuum or bound-to-quasibound transition, excited electrons easily escape the quantum well and  $p_e \approx 1$ .

An estimation of  $g_{ph}$  is possible by assuming a typical capture time  $\tau_c \approx 5 ps$  for *GaAs/AlGaAs* heterostructures [44]. The dominant process for the capture of electrons while passing through the device is LO phonon scattering [37]. The transit time can be estimated by  $\tau_{trans} \approx L_p/v$ , where  $L_p$  is the thickness of one quantum well region and  $v$  is the drift velocity of the electrons. This finally yields the desired expression for the photoconductive gain

$$g_{ph} = \frac{p_e}{N p_c} \approx \frac{\tau_c v}{N L_p} \quad (2.7)$$

Using typical numbers for the drift velocity of  $v_{sat} = 10^7 cm/s$  in GaAs, a typical thickness  $L_p = 50 nm$  and  $N = 50$  periods for a typical QWIP yields  $g_{ph} = 0.2$ , which is consistent with experimental results (Fig. 2.7) [177]. Equation 2.7 shows that the magnitude of the photoconductive gain depends on the semiconductor material ( $\tau_c$ ,  $v$ ) and on the design parameters ( $N$ ,  $L_p$ ). The drift velocity  $v$  also depends on the applied bias voltage by following relation

$$v(E) = \frac{\mu E}{\sqrt{1 + (\mu E/v_{sat})^2}} \quad (2.8)$$

where  $\mu$  is the electron mobility (e.g.  $\mu_{AlGaAs} \approx 10^3 cm^2/(Vs)$  for weakly doped  $Al_{0.3}Ga_{0.7}As$ ).

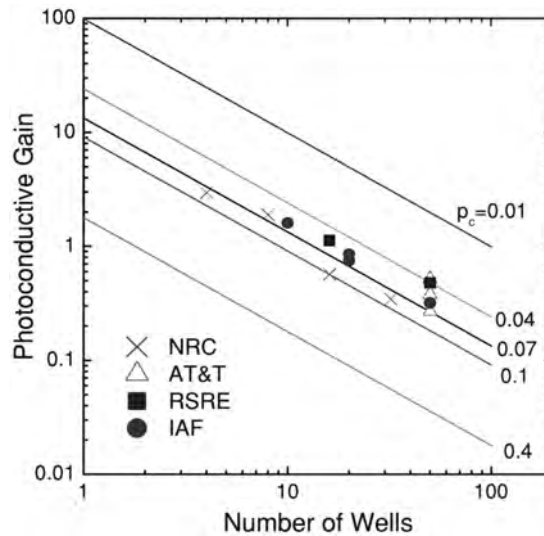


Figure 2.7: Comparison of calculated and measured photoconductive gain values. The lines correspond to simulated gain values for different capture probabilities. The experimental values (crosses, triangles, squares, bullets) are collected from different research groups. (Published in [177, 44])

### 2.2.3 Responsivity

The responsivity  $\mathcal{R}$  is defined as the amount of photocurrent  $I_{ph}$  generated at an incident optical power of  $P_{opt} = \hbar\omega\phi$  [178]. Using equation 2.3 this can be written as

$$\mathcal{R} = \frac{I_{ph}}{P_{opt}} = \frac{e}{\hbar\omega} \eta g_{ph} \quad (2.9)$$

The responsivity is an important figure of merit for the detector performance. For a high responsivity it is important to efficiently absorb photons to excite electrons, but at the same time extract the excited electrons from the quantum wells to the contacts. If both electronic states are confined in the quantum well (bound-to-bound transition), the matrix element  $M$  is large, but the escape probability  $p_e < 1$ . On the other hand, if the quantum well supports only one confined state such that the electron is excited directly into the continuum (bound-to-continuum transition), then the escape probability  $p_e \approx 1$ , but the matrix element  $M$  is small.

The optimum electronic design is a quantum well, which support two confined states, where the excited state is very close to the barrier energy (bound-to-quasibound transition). Figure 2.8a shows the electronic states in a QWIP for a bound-to-quasibound case. Responsivity simulations and measurements for varying quantum well widths are shown in Fig. 2.8b.

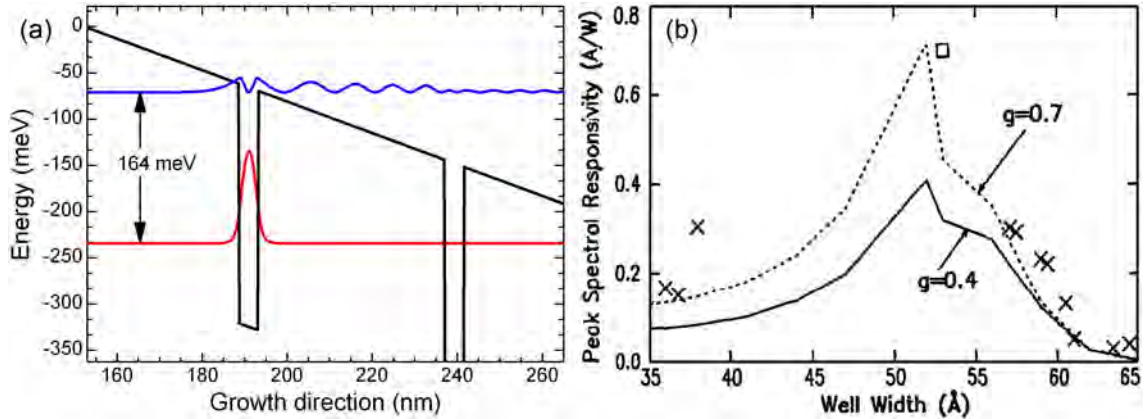


Figure 2.8: Optimum ISBT energy for high responsivity values. (a) Bound-to-quasibound transition. The quantum well dimensions are designed to support two electronic states. The excited state is close to the conduction band energy of the barrier, hence the escape probability  $p_e \approx 1$ . (b) Calculated peak spectral responsivity for a photoconductive gain  $g = 0.4$  (solid line) and  $g = 0.7$  (dashed line). The simulations are compared to experimental results (crosses and squares). The responsivity peaks at a certain well width, when the excited state is close to the barrier energy (Published in [176])

From equations 2.7 and 2.8 we know, that the photoconductive gain  $g_{ph}$  changes with the bias voltage. With increasing bias voltage, the photoconductive gain  $g_{ph}$  and, hereby, the responsivity  $R$  increases until the drift velocity of the electrons  $v(E)$  saturates. However, this behavior depends on whether the electronic transition is a bound-to-bound or a bound-to-continuum case. For a bound-to-continuum transition, the electrons only need to drift towards the contacts. Once the drift velocity of the electrons  $v(E)$  saturates, no further increase of the responsivity is expected (squares in Fig. 2.9).

For a bound-to-bound transition, the electron need to escape from the confined state, which at cold temperatures is most likely by electron tunneling. With increasing electric field, the tunneling probability and hereby the responsivity  $R$  increases, even when the drift velocity  $v(E)$  is already saturated (downward triangles in Fig. 2.9). The bound-to-quasibound case is lying somewhere in between.

It is important to understand that the responsivity cannot be increased by simply increasing the number of quantum wells  $N$ . We have seen that the absorption efficiency

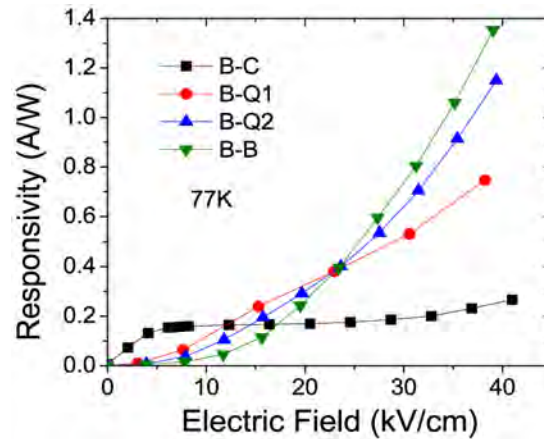


Figure 2.9: Responsivity for different intersubband transition cases. The responsivity exhibits a characteristic increase with the electric field, depending whether it is a bound-to-bound (B-B), a bound-to-quasibound (B-Q1, B-Q2) or a bound-to-continuum (B-C) transition. Note: The shown data was measured from a quantum-dot-in-a-well photodetector, but the same principles hold for QWIPs. (Published in [179]).

$\eta$  is proportional to  $N$  (Eq. 2.6), while the photoconductive gain  $g_{ph}$  is indirect proportional to  $N$  (Eq. 2.7). This means that the responsivity is independent of the number of quantum wells (Fig. 2.10). However, for noise considerations a large number of quantum wells is still desirable, which will be discussed later.

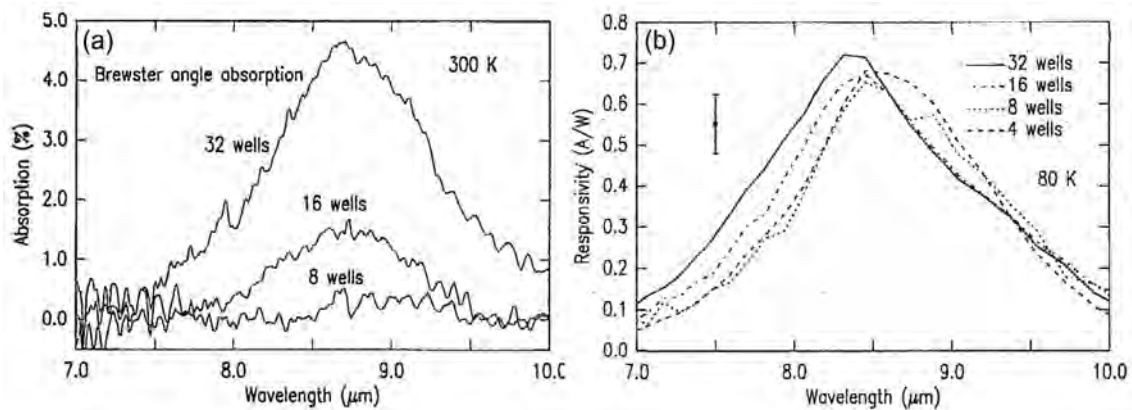


Figure 2.10: Responsivity for different numbers of quantum wells. (a) Absorption spectra for QWIP samples with 8, 16, and 32 quantum wells. (b) Spectral responsivity for different QWIPs with 4, 8, 16, and 32 quantum wells (Published in [176]).

## 2.3 Detector Performance

Good detector performance is generally desirable, but performance is not uniquely defined. Depending on the application, different detector characteristics such as signal-to-noise ratio, response time, temperature range or pixel size can be optimized. During this thesis the focus was mainly on optimization of the signal-to-noise ratio by resonant absorption enhancement. Ways to optimize the different QWIP figures-of-merit can be found in the existing literature [83, 5, 64, 65, 67, 78, 11].

A key parameter is certainly the responsivity  $\mathcal{R}$ , which was discussed in the last section. However, it is important to understand that a high responsivity is meaningless if the detector noise is dominating the system. A useful figure of merit for the detector performance is a signal-to-noise ratio, for photodetectors this is the specific detectivity  $D^*$ . In this section the important noise sources in QWIPs are introduced. Equipped with this knowledge the specific detectivity  $D^*$  will be derived.

### 2.3.1 Detector Noise Sources

In photoconductors the following noise sources are generally present:  $1/f$  noise, Johnson noise (= resistor noise), dark current noise and photon noise (= noise from photocurrent fluctuations). In QWIPs the performance is usually limited by the latter two contributions, therefore the focus will be on dark current and photon noise.

**Dark Current Noise** The dark current  $I_d$  in QWIPs mainly originates from electrons, which are thermally excited from the quantum well ground state into the continuum. An additional dark current path is formed by inter-well tunneling, which usually is suppressed by designing sufficiently thick barriers (Fig 2.11).

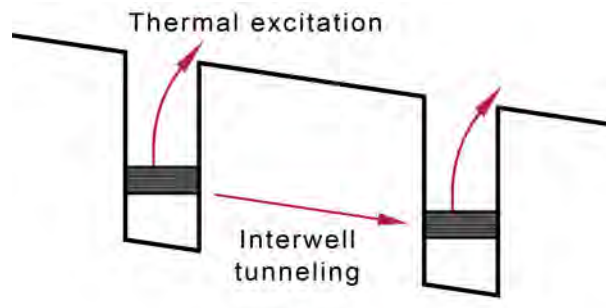


Figure 2.11: Dark current in QWIPs is caused by thermal excitation and by inter-well tunneling.

The thermally excited dark current  $I_d$  is calculated using the model presented by Kane *et al.* [37] and can be written as

$$I_d = eN_{3D}v(E)A \quad (2.10)$$

where  $N_{3D}$  is the 3D carrier density in the continuum,  $v(E)$  is the drift velocity of the electrons perpendicular to the quantum wells (from Eq. 2.8) and  $A$  is the device area. Using the 3D carrier density is justified since  $\approx 90\%$  of the device volume consists of barrier material. Also the current flows across the quantum wells and not in-plane as 2D confined carriers. Superlattice effects do not play any role, since the barriers are thick and the quantum wells are just weakly coupled. The 3D carrier density  $N_{3D}$  is the well-known expression for bulk semiconductors

$$N_{3D} \approx \frac{1}{\sqrt{2}} \left( \frac{m_b^* k_B T}{\pi \hbar^2} \right)^{3/2} \cdot \exp(-E_{act}/k_B T) \quad (2.11)$$

where  $m_b^*$  is the effective barrier electron mass [38]. The thermal activation energy  $E_{act}$  equals the energy difference between the top of the barrier and the Fermi level  $E_{act} = E_b - E_F$ . In QWIPs the quantum wells are usually doped very high to have a large absorption efficiency. Then the Fermi level is degenerate and simply given by

$$E_F = \left( \frac{\pi \hbar^2}{m_w^*} \right) N_D \quad (2.12)$$

From equation 2.11 one can see, that the 3D carrier density  $N_{3D}$  increases exponentially with the doping density  $N_D$ , as the thermal activation energy is lowered (Fig. 2.12a). Similarly, the 3D carrier density  $N_{3D}$  also increases exponentially with the thermal energy  $k_B T$  as the temperature  $T$  increases (Fig. 2.12b). This result shows the strong influence of the doping density and temperature on the dark current.

Since temperature changes are usually slow, the dark current  $I_d$  is a direct current and can be compensated using a current source. The dark current noise  $i_{n,dark}^2$  (square average) originates from fluctuations in the dark current  $I_d$ . The nature of the dark current noise is generation-recombination (g-r) noise (or in the case of a QWIP emission-capture noise) [3, 44]. The standard expression for g-r noise is

$$i_{n,dark}^2 = 4eg_{noise} I_d \Delta f \quad (2.13)$$

where  $g_{noise}$  is the noise gain and  $\Delta f$  is the measurement bandwidth [44]. A good approximation for the noise gain is given by the photoconductive gain  $g_{noise} = g_{ph}$ . If the QWIP is connected to a standard readout circuit, the measurement bandwidth is determined by the integration time of the read-out circuit  $\tau_{int} = 1/(2\Delta f)$ . If the

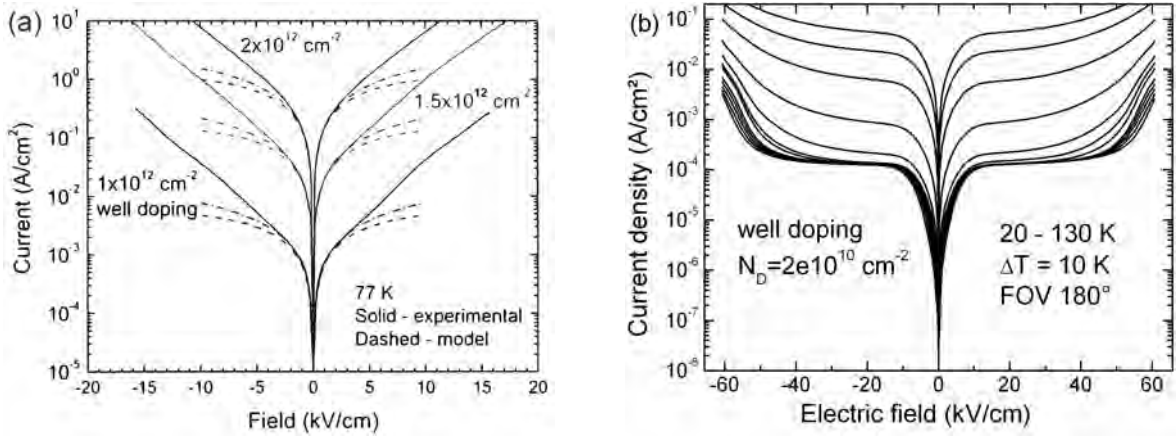


Figure 2.12: Dark current characteristics. (a) Dark current density for different well doping densities (solid lines). The dashed and dash-dotted lines are calculated using the analytical model. (b) Dark current density for different temperatures (sample H540A). Figures (a) and (b) were measured with different samples. (Image (a) published in [44])

dark current noise is measured with a spectrum analyzer,  $\Delta f$  is simply the input filter bandwidth.

**Background Photon Noise** Just like signal photons, the ambient black-body radiation is absorbed by the QWIP, generating a background photocurrent  $I_{BG}$ . The magnitude of  $I_{BG}$  depends on the background temperature, and on the field of view (FOV) under which the background radiation can hit the detector. The background noise current  $i_{n,bg}^2$  (square average) can be calculated simply by replacing the dark current  $I_d$  in equation 2.13 with the background photocurrent  $I_{BG}$

$$i_{n,bg}^2 = 4eg_{noise} I_{BG} \Delta f \quad (2.14)$$

The detector operation is limited by the background photon noise at low chip temperatures as well as for high background radiation. To reduce the background noise current, the field of view can be reduced by placing a cold aperture in front of the detector. For imaging applications, a FOV of  $\approx 90^\circ$  is a typical value. If the signal is narrow band (e.g. for data transmission applications), a further option is to use bandpass optical filters.

### 2.3.2 BLIP Temperature

Depending on the temperature, QWIPs are limited either by dark current noise or background photon noise. The temperature range, where the background photon noise

is dominating over the dark current noise, is called the background limited performance (BLIP) regime. With increasing temperature, the total noise current becomes dominated by the exponentially increasing dark current noise, and the device then operates in the detector limited performance (DLIP) regime. The temperature, where the detector switches from the BLIP regime to DLIP regime, is called  $T_{BLIP}$  and is an important QWIP performance figure (Fig. 2.13a).

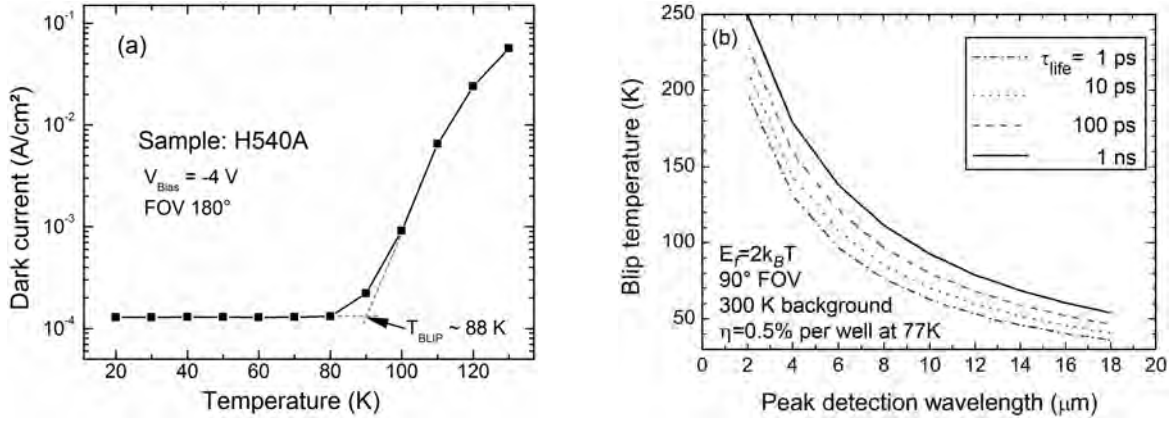


Figure 2.13: BLIP temperature. (a) Below  $T_{BLIP}$  the current is dominated by background black-body radiation. Above  $T_{BLIP}$  the dominant dark current source is thermal carrier excitation, and the dark current increases exponentially. (b) Calculated  $T_{BLIP}$  vs. peak detection wavelength for  $L_p = 50 \text{ nm}$  and different capture times  $\tau_c$ . (Image (b) published in [44])

$T_{BLIP}$  is calculated by finding the temperature, where the dark current equals the background photocurrent  $I_d = I_{BG}$ . This condition is equivalent to when the dark current noise equals the background photon noise. Using equation 2.9 together with equation 2.7 to express  $I_{BG}$ , and equation 2.10 together with equation 2.11 to express  $I_d$ , the BLIP temperature can be found by solving the following transcendental equation

$$\frac{1}{\sqrt{2}} \left( \frac{m_b^* k_B T_{BLIP}}{\pi \hbar^2} \right)^{3/2} \cdot L_p A \exp(-E_{act}/k_B T_{BLIP}) = \frac{\eta}{N} \tau_c \phi_{BG}$$

where  $\phi_{BG}$  is the background photon flux,  $\eta$  is the total absorption efficiency and  $N$  is the number of quantum wells. The most sensitive parameter for the BLIP temperature is the activation energy  $E_{act} = E_b - E_F$ , since it is in the exponent. Therefore,  $T_{BLIP}$  is mostly determined by the detection wavelength, which defines a certain barrier height  $E_b$  (Fig. 2.13b). Similarly important is the influenced of the doping on  $T_{BLIP}$ , since this affects the Fermi energy  $E_F$ . From equation 2.12 we know, that  $E_F \propto N_D$ , which means that  $T_{BLIP}$  also changes exponentially with the doping  $N_D$ .

The BLIP temperature of QWIPs is generally lower than of standard InSb or HgCdTe

band gap infrared photodetectors, which would be approximately at the solid black line in figure 2.13b. The main reason is the fast carrier capturing mechanism in QWIPs, which is advantageous for high speed applications but is counterproductive for the detectors signal-to-noise performance. Since at a certain wavelength and with a certain material system most parameters are fixed e.g. the transition matrix element  $M$  or the effective mass  $m_b^*$ , the optimization potential is limited. A possibility to realize QWIPs with a temperature performance comparable to band gap detectors would be to increase the absorption efficiency by two orders of magnitude using resonant cavity enhancement [80, 10, 44].

### 2.3.3 Detectivity

A very important figure to characterize the photodetector performance is the specific detectivity  $D^*$ . For a general photodetector it is defined as

$$D^* = \frac{\mathcal{R}}{\sqrt{\mathcal{S}_n}} \sqrt{A}$$

where  $\mathcal{R}$  is the responsivity and  $\mathcal{S}_n$  is the noise power spectral density (in units of watts per hertz [ $dBmW/Hz$ ]). The specific detectivity  $D^*$  is a kind of signal-to-noise ratio, normalized by the detector area  $A$  and the electrical bandwidth  $\Delta f$ , which allows comparing detectors of different size and between different material systems. For a photocurrent detector (e.g. QWIP),  $\mathcal{S}_n$  is related to the noise current  $i_n^2$  by

$$\mathcal{S}_n = \frac{i_n^2}{\Delta f}$$

which is called the current noise power spectral density. The specific detectivity for a photocurrent detector then reads

$$D^* = \frac{\mathcal{R}}{i_n} \sqrt{A \Delta f} \quad (2.15)$$

If the detector is operated below  $T_{BLIP}$ , then the noise current  $i_n^2$  is dominated by background photon noise. Using Eqs. (2.14) and (2.9), the background limited specific detectivity reads

$$D_{BLIP}^* = \frac{\lambda}{2hc} \sqrt{\frac{\eta}{\phi_{BG}}} \sqrt{A}$$

where  $\phi_{BG}$  is the background photon flux [44]. It is important to keep in mind, that every surface with a non-zero temperature is generating background photon flux, hence, the field of view is generally  $180^\circ$  (assuming that the detector is cold). A common way

to reduce  $\phi_{BG}$  and hereby increase  $D_{BLIP}^*$  is to reduce the FOV of the photodetector by a cold shield.

When the detector is operated above  $T_{BLIP}$ , then the noise current  $i_n^2$  is dominated by dark current noise. The dark current limited specific detectivity can be derived by inserting Eqs. (2.10), (2.11) and (2.13) into (2.15)

$$D_{DLIP}^* = \frac{\lambda}{2hc} \frac{\eta}{\sqrt{N}} \sqrt{\frac{\tau_c}{N_{3D}L_p}} \quad (2.16)$$

From Eq. (2.16) we can derive the general behavior for a QWIP: A longer wavelength  $\lambda$ , higher absorption  $\eta$  and long capture time  $\tau_c$  lead to a higher  $D^*$ . On the other hand, a large number of quantum wells  $N$  will decrease the detector limited specific detectivity (given a certain absorption efficiency  $\eta$ ). The wavelength  $\lambda$  and capture time  $\tau_c$  are mostly determined by the application and material system, but the number of wells  $N$  and the total absorption  $\eta = N\eta^{(1)}$  and can be engineered. An optimal detector will have 100% absorption efficiency with a minimum number of quantum wells, ideally with only a single quantum well. With certain restrictions (narrow bandwidth, low losses) this is indeed possible and can be achieved by resonant cavity enhancement.



# 3 Photonic Crystal Resonators

Photonic crystals (PCs) are structures with a periodic modulation of the refractive index. These structures exhibit fascinating properties for the control of light, allowing to build novel photonic materials with designable optical properties. In this chapter the theoretical description of photonic crystals will be presented. With this background, two modeling techniques for photonic crystals will be discussed: the revised plane wave method and the finite difference time domain simulation. At the end of this chapter, the focus will be on the resonant properties of photonic crystals.

## 3.1 Theory of Photonic Crystals

To theoretically describe photonic crystals a general understanding of the properties of periodic media is helpful. The most common way to treat periodic structures is in  $k$ -space, therefore, the reciprocal lattice will be introduced. From a very simple device structure, a dielectric layer stack or Bragg mirror, the important concept of the photonic band structure will be derived. With this background the properties of two-dimensional photonic crystals and photonic crystal slabs will be discussed in detail.

### 3.1.1 Periodic Media

Waves in media with a periodic modulation of the material properties behave fundamentally different than waves in homogenous media, in particular when the wavelength is on the scale of the modulation period. This fact is well known from solid-state physics and determines the physical properties of metals, semiconductors and insulators. For conventional solids, the periodic modulation is given by the periodicity of the electrostatic potential. The wave is represented by a quantum-mechanical electron wave function. The periodic potential is responsible for the formation of energy bands, band gaps and effective masses [87, 3, 38].

The theoretical description of photonic crystals is in many ways similar to the theory of semiconductors in solid-state physics. Electromagnetic waves, that propagate through media with a periodic modulation of the refractive index exhibit similar effects

e.g. photonic bands, photonic band gaps and energy dependent group velocities. For this reason, the theoretical description of photonic crystals inherited many formalisms known from solid-state physics. In the following sections important photonic crystal characteristics like crystal lattice vectors, Brillouin zone, photonic band structure, etc. will be derived [88, 91].

**Crystal Structures** A crystal is a solid structure, composed of unit cells which are arranged in a repeating fashion. Many physical and chemical properties of solids depend on the inner crystal structure [180]. The geometry of a crystal can be defined by its *primitive lattice vectors*  $a_i$  and its *primitive unit cell* (Fig. 3.1). The lattice vectors define the spatial lattice structure (or space lattice), which consists of an ordered collection of *lattice points*. The unit cell is a fundamental building block, which by periodic arrangement can be used to reconstruct the entire crystal. Therefore, for a complete analysis of the whole crystal it is sufficient to consider only the points within on single unit cell.

A lattice vector  $a_i$  is a special translation vector, that connects any point  $r$  in the crystal to another point  $r'$  such, that the crystal looks identical again

$$\vec{r}' = \vec{r} + m_1\vec{a}_1 + m_2\vec{a}_2 + m_3\vec{a}_3 = \vec{r} + \vec{R} \quad m_1, m_2, m_3 \in \mathbb{Z} \quad (3.1)$$

If the lattice vectors  $a_i$  are chosen such, that with a suitable choice of integers  $\{m_i\}$  any two lattice points can be connected, then the set of lattice vectors is called *primitive* [38]. The primitive lattice vectors are not unique, and different sets  $\{a_1, a_2\}$  or  $\{a_1', a_2'\}$  are possible and equally valid (Fig. 3.1a).

A unit cell is called *primitive*, when it contains the smallest possible volume (or area or length) to describe the entire crystal. It can be constructed by taking the primitive lattice vectors as boundaries of the cell. A primitive unit cell can occupy a one-, two- or three-dimensional space [88].

The lattice itself is only an abstract representation of the crystal. To fully characterize the crystal, the contents of the unit cell must be specified (Fig. 3.1b). For a solid-state crystal this would be the electrostatic potential distribution of the atoms within the unit cell. For a photonic crystal this is the refractive index distribution (which in general is a tensor field). For the square lattice in Fig. 3.1b this could be the refractive index for silicon for the dark shaded region and the refractive index of air for the bright regions.

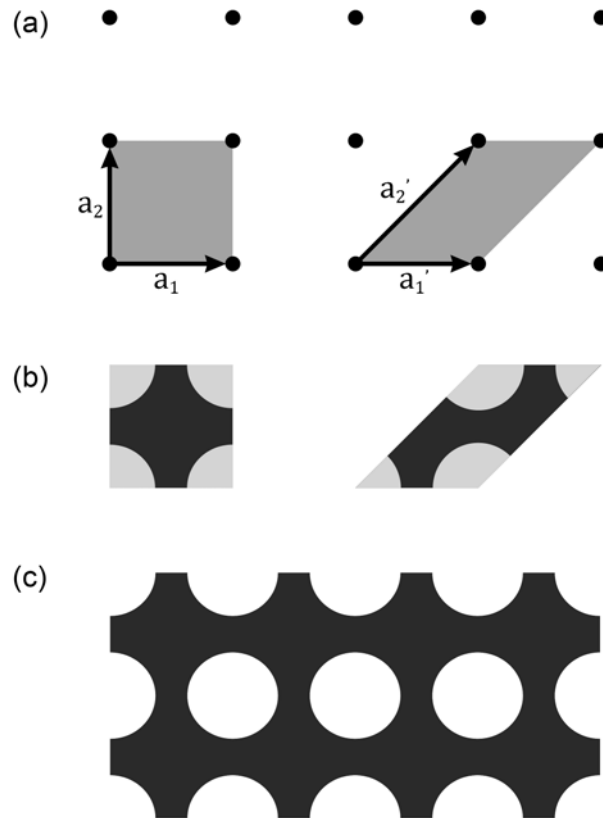


Figure 3.1: Square lattice. (a) Two-dimensional square crystal lattice with primitive lattice vectors  $\{a_1, a_2\}$  and the primitive unit cell (shaded region). The primitive lattice vectors are not unique, different sets  $\{a'_1, a'_2\}$  are possible and equally valid [91]. (b) Primitive unit cell for a square lattice of holes. (c) Several periods of the crystal structure, constructed by repetition of the unit cell using the primitive lattice vectors  $\{a_1, a_2\}$ .

An important lattice structure is the hexagonal lattice, since it has the highest filling factor for circular objects [91]. Two sets of lattice vectors for the hexagonal lattice are shown in Fig. 3.2a, together with the corresponding unit cells. The set of lattice vectors  $\{a_1, a_2\}$  is primitive. The set  $\{a'_1, a'_2\}$  is not primitive, since the lattice point in between (white arrow) cannot be reached by any choice of integers  $\{m_i\}$ . The corresponding unit cell therefore needs to contain twice as much of information as necessary to describe the whole crystal. While this is clearly unnecessary since it adds unnecessary complexity, it is sometimes preferred for numerical simulation because the lattice vectors are orthogonal.

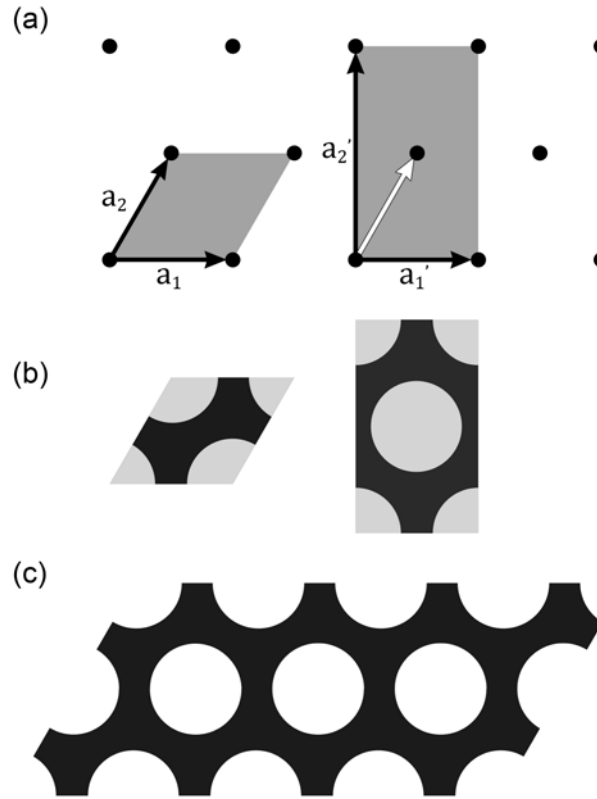


Figure 3.2: Hexagonal lattice. (a) Two-dimensional hexagonal crystal lattice with two sets of lattice vectors  $\{a_1, a_2\}$  and  $\{a'_1, a'_2\}$  and the corresponding unit cells (shaded region). The set  $\{a_1, a_2\}$  are primitive lattice vectors. The set  $\{a'_1, a'_2\}$  is not primitive, since the lattice point in between (white arrow) cannot be reached [91]. (b) Corresponding unit cells. The right unit cell contains twice as much information as necessary. (c) Several periods of the hexagonal crystal structure.

A different, yet very important unit cell is the *Wigner-Seitz cell* ( $\Omega_i$ ). It is defined as the set of all points closer to a specific lattice point than to all other lattice points

$$\Omega_i = \{\vec{r} \mid \|\vec{r} - \vec{r}_i\| < \|\vec{r} - \vec{r}_j\| \wedge j \neq i\}$$

The Wigner-Seitz cell is constructed by drawing a line between a selected point and all its neighboring points. At the center of these lines another perpendicular line is drawn. The innermost boundary of all these perpendicular lines forms the Wigner-Seitz cell (Fig. 3.3c). This algorithm allows identifying the primitive unit cell for any crystal structure, independent of its complexity. The Wigner-Seitz cell is equally valid as the conventional primitive cells from Fig. 3.1 or Fig. 3.2. Additionally, if transformed into

reciprocal space it corresponds to the Brillouin zone, which will be discussed later.

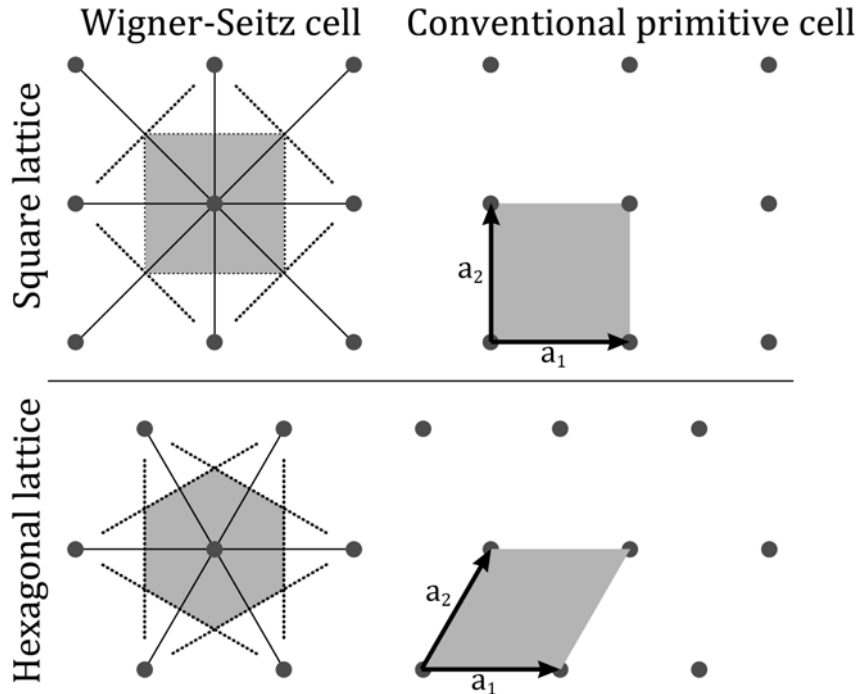


Figure 3.3: Wigner-Seitz cell (left) and conventional primitive cell (right) for square and hexagonal lattices. The Wigner-Seitz cell contains all points closer to a selected lattice point than to any other lattice point [91].

**Reciprocal Lattice** The periodicity of the crystal lattice allows the transformation of the crystal structure into the reciprocal space. This transformation into reciprocal space is advantageous, since many problems connected to periodic media can be solved more efficiently in reciprocal space than in real space. The reciprocal space is a Fourier space, where the crystal is represented as Fourier expansion of the periodic modulation in real space. For a periodic dielectric permittivity  $\varepsilon(\vec{r})$  this would be

$$\varepsilon(\vec{r}) = \sum_G \varepsilon(\vec{G}) e^{-j\vec{G}\cdot\vec{r}}$$

where  $\vec{G}$  is an infinite set of vectors in reciprocal space, that correspond to spatial frequencies. Since the structure is periodic in real space,  $\vec{G}$  must be a set of discrete frequencies. Knowing, that the periodicity in real space must be preserved in reciprocal space, helps to define  $\vec{G}$  by showing that

$$\varepsilon(\vec{r} + \vec{R}) = \sum_{\vec{G}} \varepsilon(\vec{G}) e^{-j\vec{G} \cdot (\vec{r} + \vec{R})} \stackrel{!}{=} \varepsilon(\vec{r})$$

which can be easily fulfilled only by

$$e^{-j\vec{G} \cdot \vec{R}} = 1$$

which is equivalent to the condition  $\vec{G} \cdot \vec{R} = 2\pi n$ , where  $n$  is an arbitrary integer. Using the definition of the lattice vector  $\vec{R}$  (Eq. 3.1), we can satisfy the periodicity condition by

$$\vec{G} = n_1 \vec{g}_1 + n_2 \vec{g}_2 + n_3 \vec{g}_3 \quad n_1, n_2, n_3 \in \mathbb{Z}$$

The vectors  $\vec{G}$  are called *reciprocal lattice vectors* [91]. They connect any lattice point in the reciprocal lattice to any other lattice point. The vectors  $\vec{g}_i$  are called fundamental vectors (in the reciprocal lattice) and can be calculated from the real space primitive lattice vectors by

$$\begin{aligned} g_1 &= 2\pi \frac{a_2 \times a_3}{a_1 \cdot (a_2 \times a_3)} \\ g_2 &= 2\pi \frac{a_3 \times a_1}{a_2 \cdot (a_3 \times a_1)} \\ g_3 &= 2\pi \frac{a_1 \times a_2}{a_3 \cdot (a_1 \times a_2)} \end{aligned}$$

Often, the reciprocal space is also called *k-space*, since the wave vector  $\vec{k}$  of a plane wave is defined in the reciprocal space. The wave vector  $\vec{k}$  represents the spatial frequency of the plane wave

$$A(\vec{r}, t) = A e^{-j(\omega t - \vec{k} \cdot \vec{r})}$$

In the context of solid state physics, the reciprocal space is also called momentum space, due to the relationship of the momentum  $\vec{p}$  of a particle and the wave vector  $\vec{k}$  of the corresponding wave function  $\Psi(\vec{k})$ . This relation makes use of the wave-particle duality, and illustrates the big advantage of solving problems in the reciprocal space over the real space. The coordinates in reciprocal space do not only represent the geometry but also contain a lot of physical properties, which greatly simplifies the analysis of periodic media.

**Brillouin Zone** Analog to the construction algorithm of the Wigner-Seitz cell in real space, a primitive unit cell can be constructed in reciprocal space (light shaded area

in Fig. 3.4b). This cell has great significance for the analysis of periodic media and is called the *first Brillouin zone* (FBZ). For a complete analysis of the crystal properties it is sufficient to study only the FBZ, which greatly simplifies the analysis. It is a useful convention to label the high symmetry points in the FBZ. For a hexagonal lattice these points are  $\Gamma$  at the center of the FBZ,  $K$  at half way to the nearest neighbor, and  $M$  half way to the next-nearest neighbor [91].

The dark shaded area in Fig. 3.4b is called the *irreducible Brillouin zone* (IBZ). All points within the FBZ can be mapped onto the IBZ by symmetry operations, such as rotations or mirror operations. The size of the IBZ depends on the symmetry of the crystal; the higher the symmetry, the more symmetry operations can be applied and the smaller is the IBZ. This allows to visualize the most important properties of the entire crystal in a single 2D-plot. An example is the band structure of semiconductors, which is plotted only along the high symmetry points and yet contains all the important information.

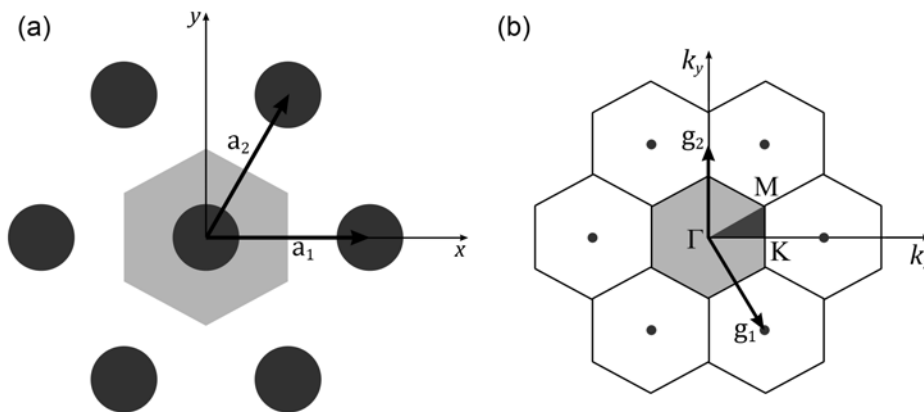


Figure 3.4: Real and reciprocal space. (a) Hexagonal lattice in real space and Wigner-Seitz cell (light gray shaded area). The vectors  $\{a_1, a_2\}$  are the primitive lattice vectors. (b) Hexagonal lattice in reciprocal space. The vectors  $\{g_1, g_2\}$  are the fundamental lattice vectors in the reciprocal space. The first Brillouin zone (light gray shaded area) contains all information to describe the properties of the entire crystal. All points of the first Brillouin zone can be mapped onto the irreducible Brillouin zone (dark gray shaded area) by symmetry operations [91].

### 3.1.2 Electromagnetism

The last section was a general introduction about periodic media and crystal properties, which is valid both for solid-state crystals and photonic crystals. This section here focuses specifically on the propagation properties of electromagnetic waves in periodic media. The theoretical background is provided by Maxwell's equations. This is different from solid-state physics, where the electron wave functions are solutions of Schrödinger's equation. For a detailed discussion about this topic, refer to some of the excellent textbooks about electrodynamics [181, 182].

In their general form Maxwell's equations read

$$\begin{aligned}
 \vec{\nabla} \times \vec{E}(\vec{r}, t) &= -\partial_t \vec{B}(\vec{r}, t) \\
 \vec{\nabla} \cdot \vec{B}(\vec{r}, t) &= 0 \\
 \vec{\nabla} \times \vec{H}(\vec{r}, t) &= \vec{J}(\vec{r}, t) + \partial_t \vec{D}(\vec{r}, t) \\
 \vec{\nabla} \cdot \vec{D}(\vec{r}, t) &= \rho(\vec{r}, t)
 \end{aligned} \tag{3.2}$$

where  $\vec{E}$  and  $\vec{H}$  are the electric and magnetic fields, respectively.  $\vec{D}$  is the electric displacement field,  $\vec{B}$  is the magnetic flux density,  $\vec{J}$  is the electric current density and  $\rho$  is the charge density. All these physical quantities are time-dependent vector or scalar fields, which implies that their values depend on their spatial and temporal coordinates. To improve readability of the following equations, the spatial and temporal dependence is left away, always keeping in mind that

$$\begin{aligned}
 \vec{E} &= \vec{E}(\vec{r}, t) & \vec{B} &= \vec{B}(\vec{r}, t) \\
 \vec{H} &= \vec{H}(\vec{r}, t) & \vec{D} &= \vec{D}(\vec{r}, t) \\
 \vec{J} &= \vec{J}(\vec{r}, t) & \rho &= \rho(\vec{r}, t)
 \end{aligned}$$

Maxwell's equations in this form describe only the coupling of the fields with the flux densities, i.e. the electric field  $\vec{E}$  with the magnetic flux density  $\vec{B}$ , as well as the coupling of the magnetic field  $\vec{H}$  with the electric displacement field  $\vec{D}$  (or electric flux density). At this point, no interaction with any matter is included. To implement the interaction of the fields with a medium, the material equations (3.3) are inserted

$$\begin{aligned}
 \vec{D} &= \tilde{\varepsilon}(\vec{E}, \vec{r}, t) \cdot \vec{E} \\
 \vec{B} &= \tilde{\mu}(\vec{H}, \vec{r}, t) \cdot \vec{H}
 \end{aligned} \tag{3.3}$$

where  $\underline{\underline{\varepsilon}}(\vec{E}, \vec{r}, t)$  is the electric permittivity tensor, and  $\underline{\underline{\mu}}(\vec{H}, \vec{r}, t)$  is the magnetic permeability tensor. In linear ( $\underline{\underline{\varepsilon}}$  independent of  $\vec{E}$ ,  $\underline{\underline{\mu}}$  independent of  $\vec{H}$ ), isotropic (scalar quantities  $\underline{\underline{\varepsilon}} = \varepsilon$ ,  $\underline{\underline{\mu}} = \mu$ ) and time-invariant ( $\varepsilon, \mu$  time independent) media, the material equations simplify to

$$\begin{aligned}\vec{D} &= \varepsilon(\vec{r}) \vec{E} \\ \vec{B} &= \mu(\vec{r}) \vec{H}\end{aligned}\tag{3.4}$$

The material properties are split into absolute values in vacuum (vacuum permittivity  $\varepsilon_0 = 8.8541... \cdot 10^{-12} \text{ Fm}^{-1}$ , vacuum permeability  $\mu_0 = 4\pi \cdot 10^{-7} \text{ Hm}^{-1}$ ), and into the relative values  $\varepsilon_r$  and  $\mu_r$ . A good approximation for most common optical materials is to set the relative permeability  $\mu_r = 1$ . The final form of the material equations for most optical materials then reads

$$\begin{aligned}\vec{D} &= \varepsilon_0 \varepsilon_r(\vec{r}) \vec{E} \\ \vec{B} &= \mu_0 \vec{H}\end{aligned}$$

Inserting these simplified material equations into Maxwell's equations, and assuming the absence of any electric charges or currents ( $\rho = 0$ ,  $\vec{J} = \vec{0}$ ), Maxwell's equations can be greatly simplified to contain only the electric and magnetic field

$$\vec{\nabla} \times \vec{E} = -\mu_0 \partial_t \vec{H}\tag{3.5}$$

$$\vec{\nabla} \cdot \vec{H} = 0\tag{3.6}$$

$$\vec{\nabla} \times \vec{H} = \varepsilon_0 \varepsilon_r(\vec{r}) \partial_t \vec{E}\tag{3.7}$$

$$\vec{\nabla} \cdot (\varepsilon(\vec{r}) \vec{E}) = 0\tag{3.8}$$

A general solution for Maxwell's equations (3.8) can be found by applying the curl operator ( $\nabla \times$ ) to Eq. 3.5 and substituting the right part with Eq. 3.7

$$\vec{\nabla} \times (\vec{\nabla} \times \vec{E}) = -\mu_0 \varepsilon_0 \varepsilon_r(\vec{r}) \partial_t^2 \vec{E}\tag{3.9}$$

Similarly, an eigenvalue equation for the magnetic field  $\vec{H}$  can be derived

$$\vec{\nabla} \times (\vec{\nabla} \times \vec{H}) = -\mu_0 \varepsilon_0 \varepsilon_r(\vec{r}) \partial_t^2 \vec{H}\tag{3.10}$$

These eigenvalue equations (3.9) and (3.10) allow calculation of the electric field  $\vec{E}$  and  $\vec{H}$  in any linear, isotropic and time-invariant medium. This includes periodic media like Bragg mirrors or photonic crystals [91].

**Electromagnetic Waves in Homogeneous Media** The eigenvalue equations (3.9) and (3.10) can further be simplified using the vector identity

$$\vec{\nabla} \times (\vec{\nabla} \times \vec{E}) = \vec{\nabla} (\vec{\nabla} \cdot \vec{E}) - \nabla^2 \vec{E}$$

In a homogeneous medium ( $\varepsilon_r(\vec{r}) = \text{const.}$ ) with no electric charges ( $\rho = 0$ ), the term  $\vec{\nabla} \cdot \vec{E}$  becomes zero. Together with the definition of the speed of light in vacuum

$$c_0 = \frac{1}{\sqrt{\mu_0 \varepsilon_0}}$$

Eq. (3.9) can be simplified to

$$\nabla^2 \vec{E} = \frac{1}{c^2} \partial_t^2 \vec{E} \quad (3.11)$$

with the speed of light in a homogeneous medium

$$c = \frac{c_0}{\sqrt{\varepsilon_r}} = \frac{c_0}{n}$$

where  $n$  is the refractive index of the material. Equation (3.11) is known as the *Helmholtz* equation and is of great importance in the entire field of optics [178].

It is important to notice, that this simplification is valid only for homogeneous media. For inhomogeneous media, it can be applied as an approximation, if the wavelength is much larger than the modulation period of  $\varepsilon_r(\vec{r})$ . From Eq. (3.8) we know that

$$\vec{\nabla} \cdot (\varepsilon(\vec{r}) \vec{E}) = \varepsilon(\vec{r}) \vec{\nabla} \cdot \vec{E} + \vec{E} \cdot \vec{\nabla} \varepsilon(\vec{r}) = 0$$

We see that  $\vec{\nabla} \cdot \vec{E}$  can only be zero, when also the gradient of  $\vec{\nabla} \varepsilon(\vec{r})$  is zero. This, however, is not true for inhomogeneous media like Bragg mirrors or photonic crystals, where the wavelength is on the order of the modulation period. To evaluate these structures, the Helmholtz equation cannot be applied [91].

A general ansatz to solve the Helmholtz equation is simply a plane wave.

$$\vec{E}(\vec{r}, t) = \vec{E}_0 e^{j(\omega t - \vec{k} \cdot \vec{r})} \quad (3.12)$$

where  $\omega$  is the oscillation frequency and  $\vec{k}$  the wave vector, which is oriented perpendicular to the phase fronts. Inserting Eq. (3.12) into the Helmholtz equation (3.11)

shows that it indeed is a general solution and yields the dispersion relation for the plane wave in a homogeneous medium (Fig. 3.5).

$$|\vec{k}|^2 = \frac{\omega^2}{c^2} \quad (3.13)$$

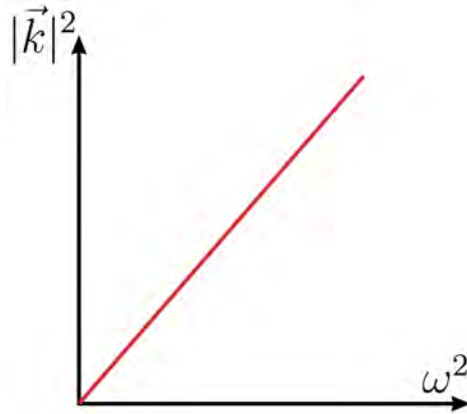


Figure 3.5: Dispersion relation for a plane wave in a homogeneous medium.

**Bloch Theorem** The periodicity of  $\varepsilon(\vec{r})$  and  $\mu(\vec{r})$  in periodic media can be expressed as

$$\begin{aligned} \varepsilon(\vec{r}) &= \varepsilon(\vec{r} + \vec{R}) \\ \mu(\vec{r}) &= \mu(\vec{r} + \vec{R}) \end{aligned} \quad (3.14)$$

where  $\vec{r}$  points to some arbitrary point in the lattice, and  $\vec{R}$  is an arbitrary lattice vector (Eq. 3.1). From these expressions, we can assume that the solutions of the eigenvalue Eqs. (3.9) and (3.10) will also reflect the periodicity of the material. This allows us to write the eigenfunctions as a product of a plane wave and a periodic function

$$\begin{aligned} \vec{E} &= e^{-j\vec{k}\cdot\vec{r}} \vec{E}_k(\vec{r}) \\ \vec{H} &= e^{-j\vec{k}\cdot\vec{r}} \vec{H}_k(\vec{r}) \end{aligned} \quad (3.15)$$

where  $\vec{E}_k(\vec{r})$  and  $\vec{H}_k(\vec{r})$  are periodic functions with the periodicity of the crystal lattice

$$\begin{aligned}\vec{E}_k(\vec{r}) &= \vec{E}_k(\vec{r} + \vec{R}) \\ \vec{H}_k(\vec{r}) &= \vec{H}_k(\vec{r} + \vec{R})\end{aligned}\tag{3.16}$$

The resulting eigenfunctions  $\vec{E}$  or  $\vec{H}$  are simply plane waves  $e^{-j\vec{k}\cdot\vec{r}}$ , which are modulated with (complex amplitude) functions  $\vec{E}_k(\vec{r})$  or  $\vec{H}_k(\vec{r})$ , that have the same periodicity as the lattice. This idea is known as the *Bloch theorem*, well-known from solid-state physics [38, 87, 91]. The modulation functions  $\vec{E}_k(\vec{r})$  and  $\vec{H}_k(\vec{r})$  are called *Bloch functions*, the resulting eigenfunctions  $\vec{E}$  and  $\vec{H}$  are called *Bloch waves*.

## 3.2 1D Photonic Crystals

The simplest possible photonic crystal consists of alternating layers of materials with different refractive indices (Fig. 3.6). The ideal one-dimensional photonic crystal extends to infinity in all three dimensions. It is called one-dimensional, because refractive index is periodically modulated only in  $z$ -direction, in the  $xy$ -direction the structure is translation invariant. Such device structures are known already for several decades, usually as multi-layer film or *Bragg mirror* [183]. They are intensively used as optical filters or high-quality mirrors in optical systems.

The traditional approach to describe such structures is to send a plane wave through the infinite multi-layer stack and consider the multiple reflections at each interface. The structure is entirely described in real space. An excellent overview about multi-layer films following this approach is presented in [178]. Here we describe the structure in reciprocal space. We will introduce *photonic band structures* and *photonic band gaps* for the analysis of the wave propagation properties of these structures. These ideas can then easily be generalized for the analysis of two- and three-dimensional photonic crystals.

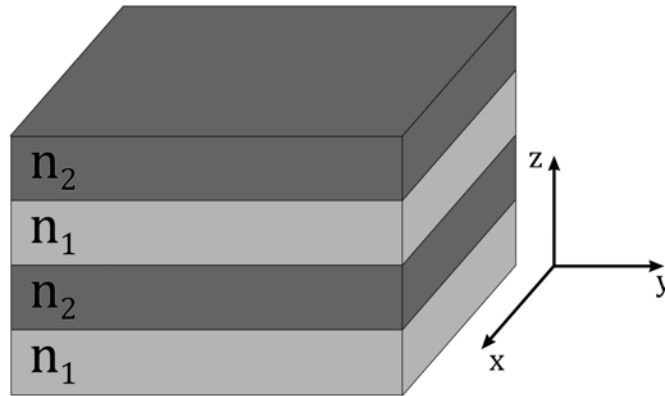


Figure 3.6: One-dimensional photonic crystal, consisting of alternating layers of materials with two different refractive indices  $n_1$  and  $n_2$ .

Since we are looking at a periodic structure, we can apply the *Bloch theorem* to express the electromagnetic eigenmodes. The material is periodic in  $z$ -direction and homogeneous in  $xy$ -direction, so we separate the wave vector  $\vec{k}$  into a wave vector component  $k_z$  for the direction perpendicular to the index modulation and  $\vec{k}_{\parallel}$  for the in-plane direction. Using Eq. (3.15) we can write the eigenmodes of the magnetic field as

$$\vec{H}_{\vec{k}_{\parallel}, k_z} = e^{-j\vec{k}_{\parallel} \cdot \vec{\rho}} e^{-jk_z z} \vec{H}_{\vec{k}_{\parallel}, k_z}(z)$$

where  $\vec{\rho}$  is the in-plane radius. The Bloch function  $\vec{H}(z)$  is  $z$ -periodic, which means that it is sufficient to restrict  $k_z$  to the first Brillouin zone  $-\pi/a < k_z < \pi/a$ , and still be able to fully describe the optical properties of the structure. However, the in-plane wave vector  $\vec{k}_{\parallel}$  still can take any arbitrary value.

### 3.2.1 Photonic Band Structure

For now we consider  $\vec{k}_{\parallel} = \vec{0}$ , which means that the wave is propagating through the multi-layer stack in  $z$ -direction and perpendicular to the layers. The dispersion relation for a layer stack, where the dielectric constant of all layers is identical, is shown in Fig. 3.7a [88]. This structure is identical to a homogeneous medium. The dispersion relation must be the same as for a homogeneous material (Fig. 3.5), just that here we have artificially added the periodicity  $a$ . From Eq. (3.13) we know, that the dispersion relation of a homogeneous medium is simply a straight line, where the gradient is the vacuum speed of light  $c_0$  reduced by the refractive index  $n$ .

$$\omega(k) = \frac{c_0}{n} |k|$$

The artificially added periodicity causes the electromagnetic eigenmodes to be  $\frac{2\pi}{a}$ -periodic for varying wave vector  $k_z$ , hence, the dispersion relations overlap (Fig. 3.7a). It looks like the lines are folded back into the first Brillouin zone. This visualizes why it is sufficient to consider only the first Brillouin zone. However, one has to keep in mind that the “back-folding” is only a kind of visualization. To get the real wave vector  $k$  of the propagating wave, the value  $\frac{2\pi}{a}$  has to be added as many times as the dispersion line was folded back.<sup>1</sup>

Now we consider wave propagation through an identical structure, except with alternating refractive indices of  $n_1$  and  $n_2$  (Fig. 3.7b). The dispersion relation now looks very different. It consists of horizontal bands, which are interrupted by frequency gaps. Each point on a *photonic band* corresponds to an *eigenmode* of the multi-layer structure. The gaps are called *photonic band gaps*. In a band gap, no wave propagation is possible, regardless of the wave vector  $k_z$ . The analogon in solid-state physics is the electronic band gap, which is the reason for the existence of semiconductors [87, 38, 88].

The dispersion diagram is usually plotted only for the region of the first Brillouin zone, since everything outside is just a repetition. This diagram is then called the *photonic band structure*. Again, the analogon in solid-state physics is the electronic band structure. The band structure visualizes the most important properties of the periodic medium in one single graph, and is therefore the most important tool for characterization of periodic media.

---

<sup>1</sup>Often the “back-folding” of the dispersion relation is treated like a physical process. In reality it is only a way to simplify the representation of the dispersion relation, which easily leads to confusion. Luckily, in most situations only the gradient of the bands is important, which represents the group velocity (or effective mass) in periodic media. This can be extracted directly from the first Brillouin zone.

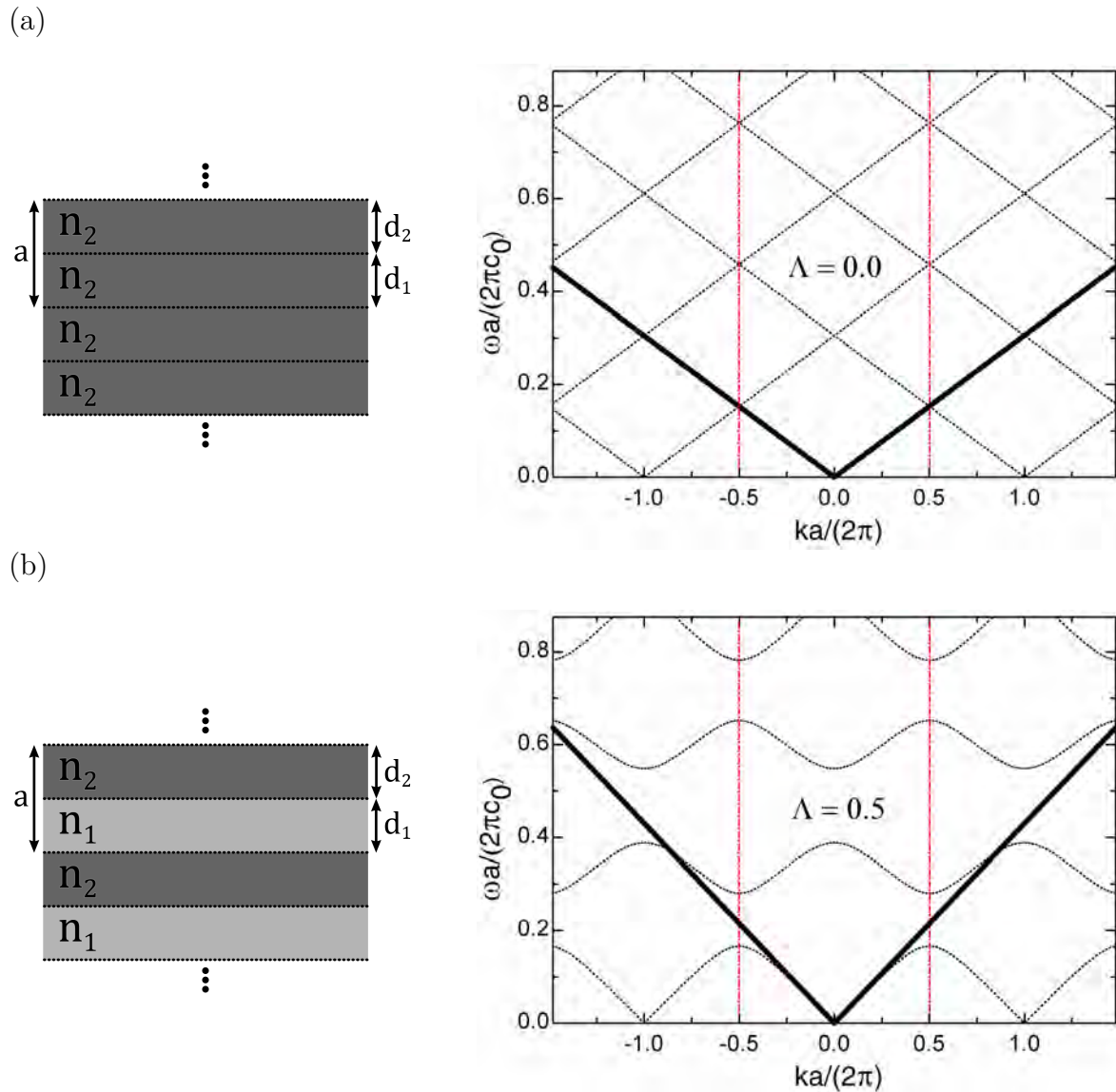
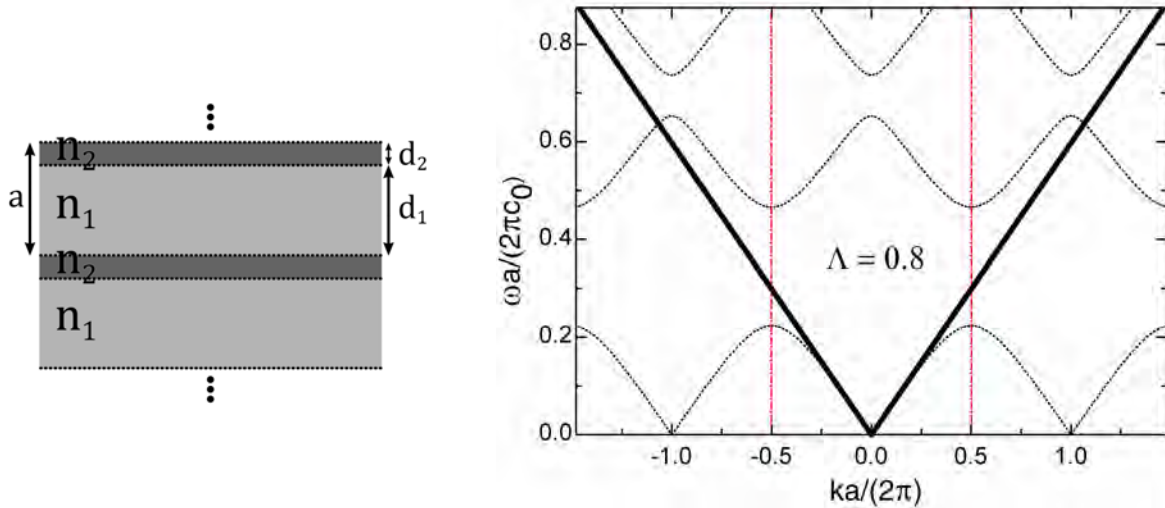


Figure 3.7: Layer structure and dispersion relation of a one-dimensional photonic crystal. (a) Propagation through homogeneous material with refractive index  $n_2$ . The artificially added periodicity causes the dispersion lines to “fold back” at the border of the first Brillouin zone. (b) Propagation through layers with alternating refractive indices  $n_1$  and  $n_2$ . At certain frequencies, no wave propagation is possible. These regions are called band gaps. The solid black lines show the dispersion relation of a homogeneous medium with the average refractive index of  $n_1$  and  $n_2$ .

The width of the photonic band gap depends on the refractive index contrast  $n_1/n_2$  and on the duty cycle  $\Lambda = d_1/a$ . The larger the contrast or the duty cycle, the wider the band gap. Figure 3.8a shows the photonic band structure for a duty cycle of  $\Lambda = 0.8$ . For many applications it is important to have photonic band gaps as wide as possible, for example to build high-quality broadband mirrors. When the duty cycle becomes

$\Lambda = 1.0$ , the structure is identical to a homogeneous medium with refractive index  $n_1$ . The band structure then again consists simply of the dispersion relation of the homogeneous medium, folded back at the border of the first Brillouin zone.

(a)



(b)

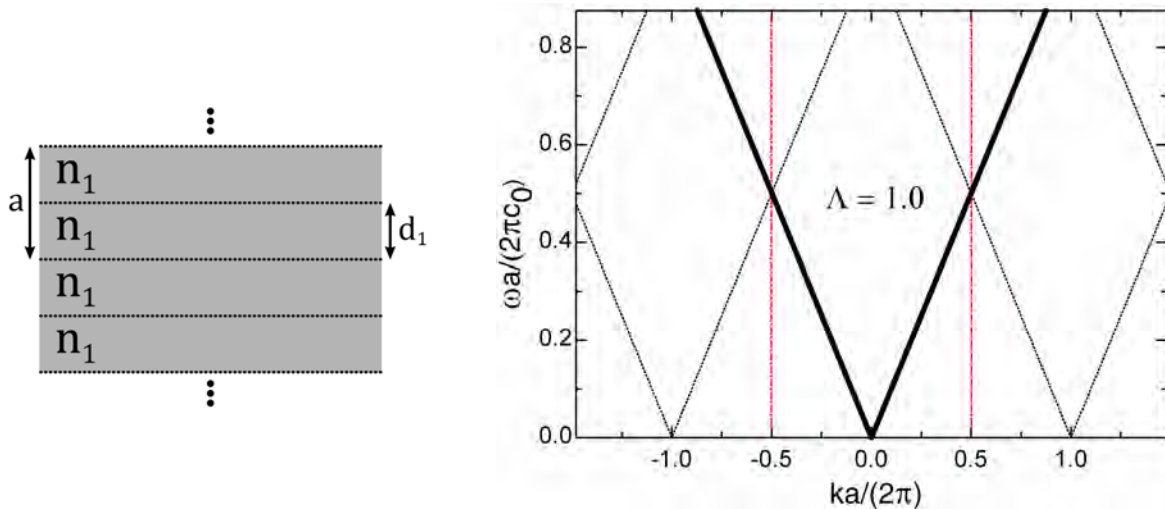


Figure 3.8: Layer structure and dispersion relation of a one-dimensional photonic crystal. (a) Photonic band structure for a duty cycle of  $\Lambda = 0.8$ . (b) For a duty cycle of  $\Lambda = 1.0$ , the layer stack is identical to a homogeneous medium with refractive index  $n_1$ . The solid black lines show the dispersion relation of a homogeneous medium with the average refractive index of  $n_1$  and  $n_2$ .

It is interesting to compare the photonic band structure to the dispersion relation of a homogeneous medium with a refractive index, that is the average refractive index of  $n_1$  and  $n_2$ . This is represented by the solid black lines in Fig. 3.7 and Fig. 3.8. For homogeneous media, this is of course identical to the photonic bands, except it is not

folded back at the borders of the first Brillouin zone (Fig. 3.7a and Fig. 3.8b). In periodic media, it corresponds to the gradient of the lowest band at low frequencies (Fig. 3.7b and Fig. 3.8a). This shows, that for low frequencies where the wavelength is much larger than the modulation period, the periodic medium behaves like a homogeneous medium with the average refractive index of  $n_1$  and  $n_2$ . Once the wavelength becomes comparable to the modulation period, this approximation fails, and the photonic band structure is necessary to correctly describe the system.

### 3.2.2 Off-axis Wave Propagation

So far we have considered wave propagation only in  $z$ -direction (perpendicular through the layers), which is equal to setting  $\vec{k}_{\parallel} = \vec{0}$ . For a complete description of the optical properties, we now consider also off-axis propagation ( $\vec{k}_{\parallel} \neq \vec{0}$ ). Figure 3.9 shows the photonic band structure for a layer stack with refractive indices  $n_1 = 1.0$  (air),  $n_2 = 3.0$  (dielectric), and a duty cycle  $\Lambda = 0.5$ . There are two main differences between on-axis and off-axis propagation: (i) There are no band gaps for off-axis propagation, since the refractive index is not modulated in in-plane direction. (ii) While the photonic bands are degenerate for on-axis propagation, they split up for off-axis propagation. This happens always when the symmetry of the crystal is broken [88].

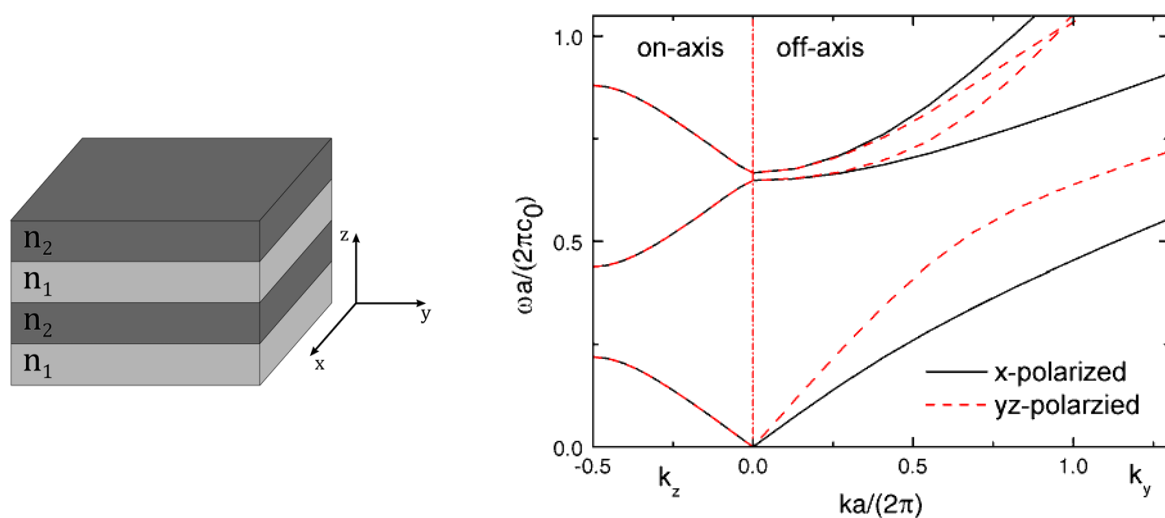


Figure 3.9: Off-axis propagation through a dielectric multi-layer stack. The photonic band structure is calculated for a duty cycle  $\Lambda = 0.5$ . For on-axis propagation, the modes are degenerate and both polarizations overlap. For off-axis wave propagation, the photonic bands split up. Band gaps exist only for on-axis propagation ( $\vec{k}_{\parallel} = \vec{0}$ ).

### 3.3 2D Photonic Crystals

Today, the majority of photonic crystal publications are based on 2D photonic crystals. The obvious reason is, that the fabrication of 3D photonic crystals poses a great challenge at infrared and visible frequencies. Fortunately, most of the interesting optical properties of 3D photonic crystals can be found also in their 2D counterparts [107]. 1D photonic crystals are intensively used as dielectric mirrors, but the overall design freedom is somewhat limited. Hence, the main interest in current research is focused on 2D photonic crystal structures.

The term *2D photonic crystal* is not uniquely defined and commonly applied to two different structures: 1) “real” 2D photonic crystals are structures that are periodic in two dimensions and constant in the third dimension (Fig. 3.10a). 2) photonic crystal slabs, where the structure is finite (e.g. a thin slab) in the third dimension (Fig. 3.10b). A distinction between the two cases can be made by looking at the electromagnetic field distribution in the crystal. If the optical mode “feels” the vertical confinement, then it is referred to as a photonic crystal slab. To any 2D structures with a considerably large extension in the third dimension, where the optical mode does not “feel” the borders, we will simply refer to as 2D photonic crystals.

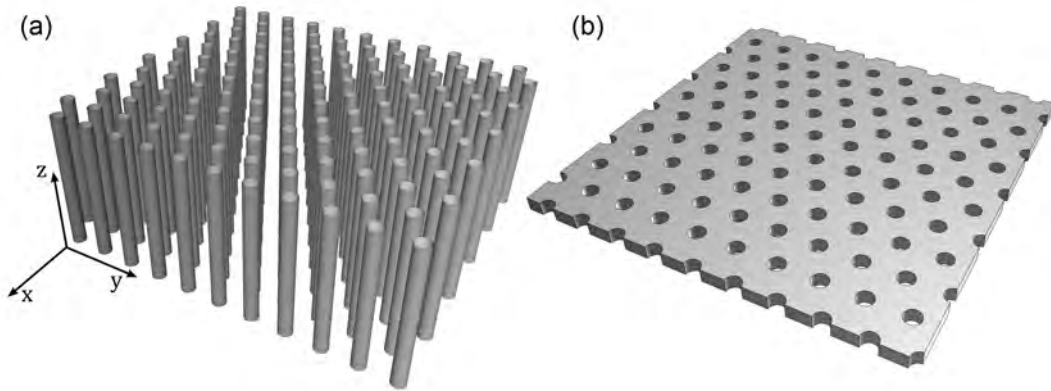


Figure 3.10: Two-dimensional photonic crystals. (a) 2D photonic crystal consisting of infinitely parallel cylinders of dielectric material. (b) A photonic crystal slab is a periodically perforated dielectric slab.

“Real” 2D photonic crystals cannot exist in reality, but they present an excellent theoretical model. In some situations they can be used as a good approximation for physically existing structures, e.g. in photonic crystal fibers [116] or when the mode is confined to the 2D photonic crystal by metallic mirrors [157]. To characterize the

optical properties of 2D photonic crystals, we are again looking at the photonic band structure. Several methods are available to calculate the band structure, but here we will focus on the plane wave expansion method.

### 3.3.1 Plane Wave Expansion Method

The PWEM implements a Fourier decomposition of the periodic permittivity  $\varepsilon_r(\vec{r})$  to find the periodic Bloch functions  $\vec{E}_k(\vec{r})$  and  $\vec{H}_k(\vec{r})$  [98, 99]. With this conversion from real space to reciprocal space an algebraic eigenvalue problem can be defined. The eigenvalue problem is then solved for all  $\vec{k}$  values along the boundary of the irreducible Brillouin zone, resulting in the photonic band structure of the photonic crystal. With a powerful eigenvalue solver, which are available as standard software today, this method yields a complete 2D band structure in a matter of seconds on a conventional desktop computer. A common freeware tool is the MIT Photonic Bands solver, which includes all software tools to compute photonic band structures of photonic crystals with the PWEM [184].

The Bloch theorem (section 3.1.2) allows us to express the electric field in the photonic crystal as the product of a plane wave and a periodic Bloch function

$$\vec{E}(\vec{k}, \vec{r}) = e^{-j\vec{k}\cdot\vec{r}}\vec{u}(\vec{k}, \vec{r}) \quad (3.17)$$

where  $\vec{u}_k(\vec{r})$  has the same periodicity as the lattice. Therefore, it can be represented as a Fourier series

$$\vec{u}(\vec{k}, \vec{r}) = \sum_{\vec{G}} A^E(\vec{k}, \vec{G}) e^{-j\vec{G}_n\cdot\vec{r}}$$

where  $\vec{k} = k_x\vec{e}_x + k_y\vec{e}_y$  is a two-dimensional vector and  $A^E(\vec{k}, \vec{G})$  are the Fourier coefficients. Inserting this result into the Bloch theorem (Eq. 3.17) leads to

$$\vec{E}(\vec{k}, \vec{r}) = \sum_{\vec{G}} A^E(\vec{k}, \vec{G}) e^{-j(\vec{k}+\vec{G}_n)\cdot\vec{r}} \quad (3.18)$$

Similarly, the magnetic field can be decomposed, which yields

$$\vec{H}(\vec{k}, \vec{r}) = \sum_{\vec{G}} A^H(\vec{k}, \vec{G}) e^{-j(\vec{k}+\vec{G}_n)\cdot\vec{r}}$$

The dielectric permittivity  $\varepsilon_r(\vec{r})$  also satisfies the condition  $\varepsilon(\vec{r}) = \varepsilon(\vec{r} + \vec{R})$  and it can be decomposed into a Fourier series

$$\varepsilon_r(\vec{r}) = \sum_G \kappa(\vec{G}) e^{-j\vec{G}_n \cdot \vec{r}}$$

where  $\kappa(\vec{G})$  are the Fourier coefficients. To solve the eigenvalue equation, the reciprocal function  $\varepsilon_r^{-1}(\vec{r})$  is necessary. Since  $\varepsilon_r(\vec{r})$  is periodic,  $\varepsilon_r^{-1}(\vec{r})$  is also periodic and can be expressed as a Fourier series

$$\varepsilon_r^{-1}(\vec{r}) = \sum_G \theta(\vec{G}) e^{-j\vec{G}_n \cdot \vec{r}} \quad (3.19)$$

The Fourier coefficients  $\theta(\vec{G})$  of the reciprocal permittivity function  $\varepsilon_r^{-1}(\vec{r})$  can be calculated very efficiently using fast Fourier transformation (FFT) or for simple geometries by using an analytical expression.

A consequence of the translational invariance in  $z$ -direction is that the electromagnetic modes can be separated into two polarization, namely TM and TE. In real 2D photonic crystals a TM mode has only non-zero  $E_z$ ,  $H_x$  and  $H_y$  component, while a TE mode has only non-zero  $H_z$ ,  $E_x$  and  $E_y$  components. This fact greatly simplifies the following analysis, but the two polarizations have to be treated separately. Here we will only show briefly the derivation for TM modes, since this polarization is relevant for QWIPs. For a more complete mathematical introduction, refer to [91, 185].

**Transverse Magnetic Polarization** In section 3.1.2 we have derived the eigenvalue equation for the electric field directly from Maxwell's equations

$$\frac{1}{\varepsilon_r(\vec{r})} \vec{\nabla} \times (\vec{\nabla} \times \vec{E}(\vec{r})) = \left(\frac{\omega}{c_0}\right)^2 \vec{E}(\vec{r}) \quad (3.20)$$

Since for TM polarization only the  $E_z$  component is non-zero, we expect to find a much simpler eigenvalue equation. For this, we apply the  $(\vec{\nabla} \times)$  operator to the Fourier decomposition of the electric field (Eq. 3.18), which leads to

$$\begin{aligned} \vec{\nabla} \times \vec{E}(\vec{k}, \vec{r}) &= \sum_G \vec{\nabla} \times [\vec{A}^E(\vec{k}, \vec{G}) e^{-j(\vec{k}+\vec{G}) \cdot \vec{r}}] = \\ \sum_G \left[ e^{-j(\vec{k}+\vec{G}) \cdot \vec{r}} \underbrace{\vec{\nabla} \times \vec{A}^E(\vec{k}, \vec{G})}_{=\vec{0}} + (\nabla e^{-j(\vec{k}+\vec{G}) \cdot \vec{r}}) \times \vec{A}^E(\vec{k}, \vec{G}) \right] &= \\ \sum_G \left[ -j e^{-j(\vec{k}+\vec{G}) \cdot \vec{r}} ((\vec{k} + \vec{G}) \times \vec{A}^E(\vec{k}, \vec{G})) \right] \end{aligned}$$

Application of another  $(\vec{\nabla} \times)$  operator will result the desired eigenvalue equation for the electric field

$$\vec{\nabla} \times \vec{\nabla} \times \vec{E}(\vec{k}, \vec{r}) = \sum_{\vec{G}} e^{-j(\vec{k}+\vec{G})\cdot\vec{r}} \left[ A^E(\vec{k}, \vec{G}) \left( (\vec{k} + \vec{G}) \cdot (\vec{k} + \vec{G}) \right) \right]$$

Inserting the decomposition of the reciprocal permittivity function (Eq. 3.19) and some rearranging of the indices finally leads to

$$\sum_{\vec{G}} \left( (\vec{k} + \vec{G}') \theta(\vec{G}' - \vec{G}) \cdot (\vec{k} + \vec{G}) \right) A^E(\vec{k}, \vec{G}) = \left( \frac{\omega}{c_0} \right)^2 A^E(\vec{k}, \vec{G}) \quad (3.21)$$

This result can be written in matrix form as

$$\mathbf{A}\mathbf{x} = \lambda\mathbf{x}$$

where  $\left( \frac{\omega}{c_0} \right)^2$  are the eigenvalues.

For a set of wave vectors  $\{\vec{k}\}$ , Eq. (3.21) will yield a set of frequencies  $\{\omega\}$ . This way the dispersion relation  $\omega(\vec{k})$  can easily be calculated. Simulation along the border of the IBZ results in the photonic band structure of the 2D photonic crystal (Fig. 3.11). If the entire Brillouin zone is simulated, the resulting photonic band structure consists of dispersion surfaces (Fig. 3.12).

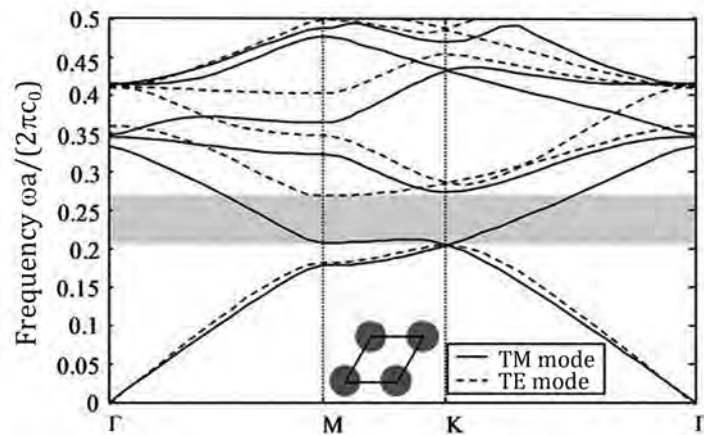


Figure 3.11: Photonic band structure for a hexagonal lattice of dielectric cylinders, calculated with the PWEM. (Published in [91])

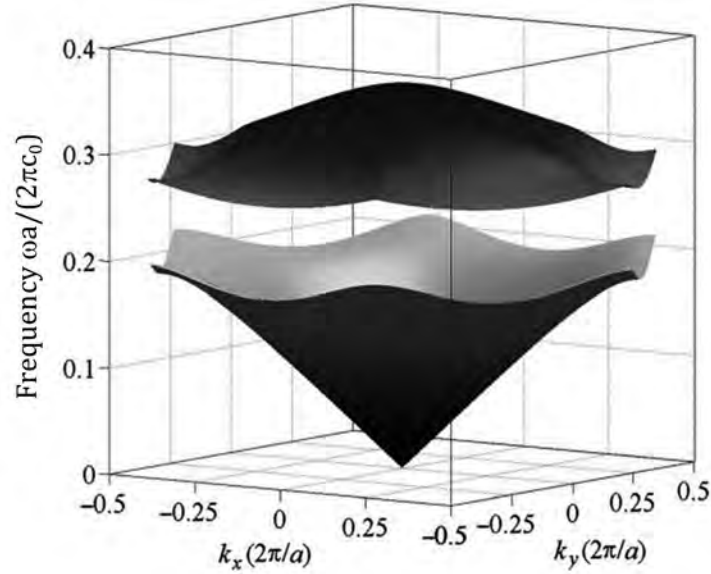


Figure 3.12: Dispersion surfaces of the first and second photonic band for a 2D photonic crystal with a hexagonal lattice of dielectric cylinders. (Published in [91])

### 3.3.2 Photonic Crystal Slabs

Photonic crystal slabs are 2D photonic crystals, where the height is finite and comparable to the wavelength. The optical modes inside the PCS can “feel” the borders of the slab. Although the refractive index modulation is only in two dimensions, a PCS has to be treated as a three-dimensional structure. The dispersion relation of a PCS is determined by both, the photonic crystal and the slab waveguide. The optical modes in a PCS cannot be separated into TE and TM polarization anymore, since the translational invariance in  $z$ -direction is lost. However, it was shown that the modes in a PCS are still similar to the pure TE and TM modes in a 2D photonic crystal [122, 123]. For this reason the modes in a PCS are referred to as TE-like and TM-like modes.

The modes in a PCS are separated into guided modes and radiative modes (Fig. 3.13). Guided modes are strongly localized within the slab and cannot couple to free-space modes. For PCS waveguides, guided modes are preferred since the losses to the surrounding medium are much lower. On the other hand, radiative modes do couple to free-space modes, hence, these modes are used for in- and out-coupling of light into PCSs. Naturally, for a photodetector only radiative modes are useful, since they allow energy transfer from the free-space wave to the optical PCS mode. The border

between guided and radiative modes is called the light line. The light line is simply the dispersion relation of free space  $\omega(\vec{k}) = \frac{c_0}{n} |\vec{k}_{air}|$ . Along the light line the free-space wave vector  $\vec{k}_{air}$  and the PCS mode in-plane wave vector  $\vec{k}_{||}$  are equal [91].

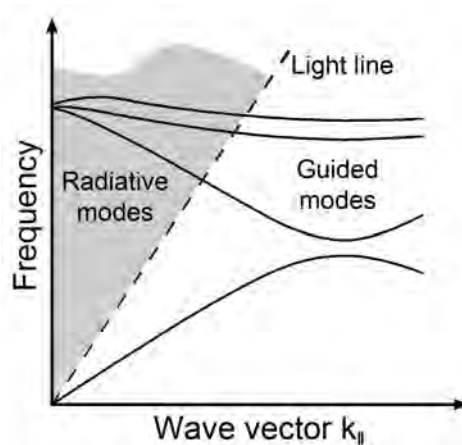


Figure 3.13: Schematic dispersion relation for a photonic crystal slab. The modes in a PCS are separated into guided modes and radiative modes. Guided modes are strongly localized within the slab while radiative modes can also couple to free-space modes [91].

### 3.3.3 Modeling of Photonic Crystal Slabs

To calculate the photonic band structure of photonic crystal slabs, the dispersion of the slab waveguide needs to be considered as well. A possibility is to simulate the wave propagation in a PCS with a full 3D simulation tool. A universal approach to simulate the wave propagation in any kind of structure is to perform a finite difference time domain (FDTD) simulation [186, 187]. The drawback of the FDTD method is that the simulation is computational very demanding and solving a problem can take several hours up to days or even weeks.

A more time-efficient approach is to treat the PCS as the combination of a slab waveguide without holes and 2D photonic crystal (Fig. 3.14). The dispersion of the slab waveguide is introduced into the 2D photonic crystal calculation as a frequency dependent permittivity  $\varepsilon_r = \varepsilon_r(\omega)$ . In a first step, the dispersion relation for a slab waveguide without holes is calculated (Fig. 3.15). From this calculation, an effective refractive index  $n_{eff}$  is derived, which is then introduced into the 2D photonic crystal calculation  $\varepsilon_r(\omega) = (n_{eff}(\omega))^2$  [188].

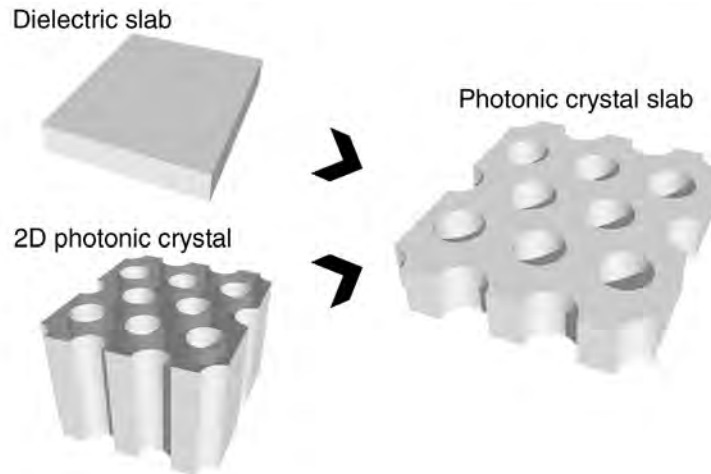


Figure 3.14: Photonic crystal slab modeling. To calculate the photonic band structure of a photonic crystal slab, the dispersion of the slab waveguide is coupled with the band structure calculation of a 2D photonic crystal. (Published in [185])

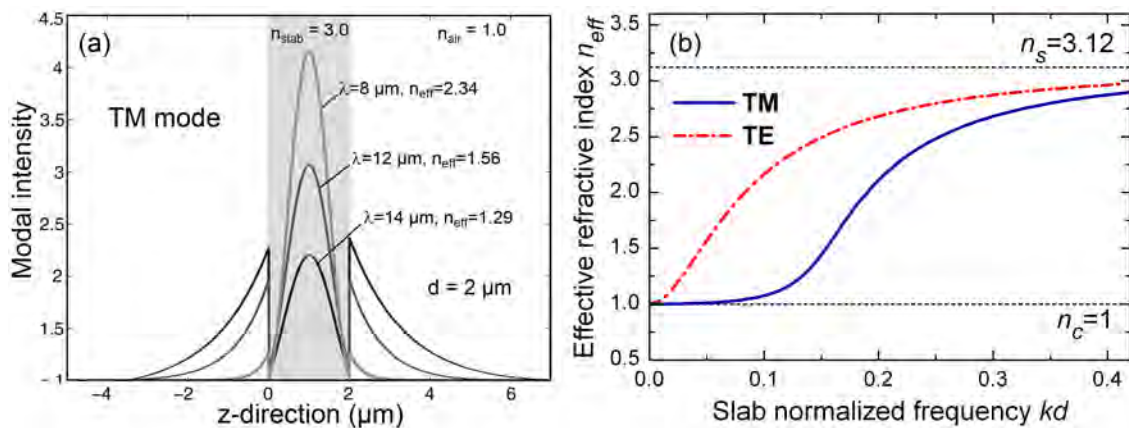


Figure 3.15: Effective refractive index of a slab waveguide. (a) The mode profile in a slab waveguide depends on the wavelength of the light. The further the mode leaks into the surrounding medium, the lower is the effective refractive index. (b) Simulation of the effective refractive index for a GaAs slab waveguide ( $n_{GaAs} = 3.12$ ). The frequency is normalized by the waveguide thickness  $d$ . (Image (b) published in [185])

Unfortunately, the very efficient PWEM, used for the simulation of 2D photonic crystals, does not support a frequency dependent permittivity  $\epsilon_r(\omega)$ . For this purpose, the revised plane wave expansion method (RPWEM) was developed [189]. The eigenvalue problem in the RPWEM is changed from solving for  $\omega$  (like in the PWEM) to solving

for  $\vec{k}$ . By making  $\omega$  an input parameter, a different permittivity can be considered for each frequency point. Since  $\vec{k}$  is a vector, that consists of the two components  $k_x$  and  $k_y$ , the eigenvalue problem is solved for one component of the  $\vec{k}$ -vector (e.g.  $k_x$ ) while the other component (e.g.  $k_y$ ) is the second input parameter (Fig. 3.16).

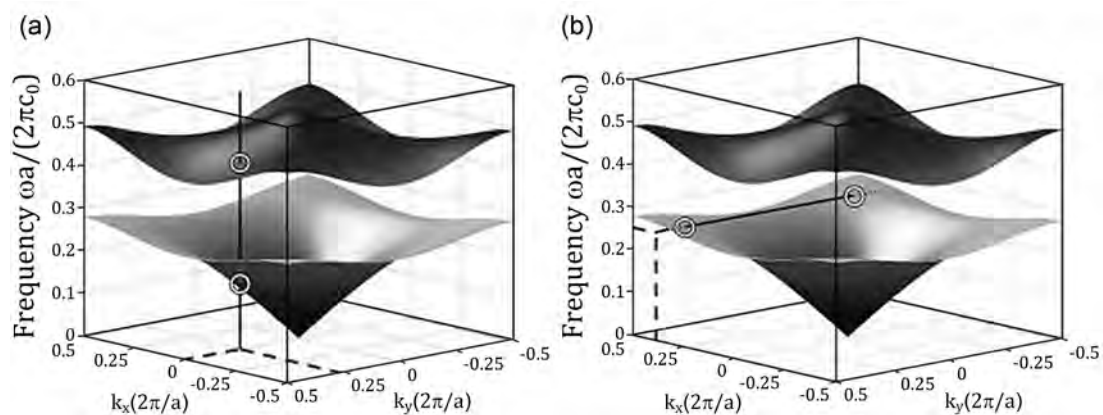


Figure 3.16: Comparison of the input parameters and results for the PWEM and RPWEM. Dashed lines indicate input parameters, the circles indicate found eigenvalues. (a) For the conventional PWEM, the input parameters are a pairs of  $k$ -values  $\{k_x, k_y\}$ . The resulting eigenvalues are the frequencies  $\omega_n$ . (b) For the revised PWEM, the input parameters are one  $k$ -value and a frequency e.g.  $\{k_x, \omega\}$ , the results are eigenvalues for the  $k$ -vector  $k_{y,n}$ . (Published in [91])

The problem with this approach is, that it is not possible to simulate along an arbitrary path in the  $k$ -space. For this purpose, an improved version of the RPWEM was developed, where  $\vec{k}$  is split into arbitrary vectors  $\vec{k}_0$  and  $\vec{k}_1$  [100]. This allows to simulate along any straight path in  $k$ -space by leaving  $\vec{k}_0$  constant and multiplying  $\vec{k}_1$  by a scalar value  $\alpha$ . The eigenvalue problem is then reformulated to solve for  $\alpha$ . This method permits to efficiently calculate the photonic band structure along the border of the IBZ for any photonic crystal slab (Fig. 3.17a).

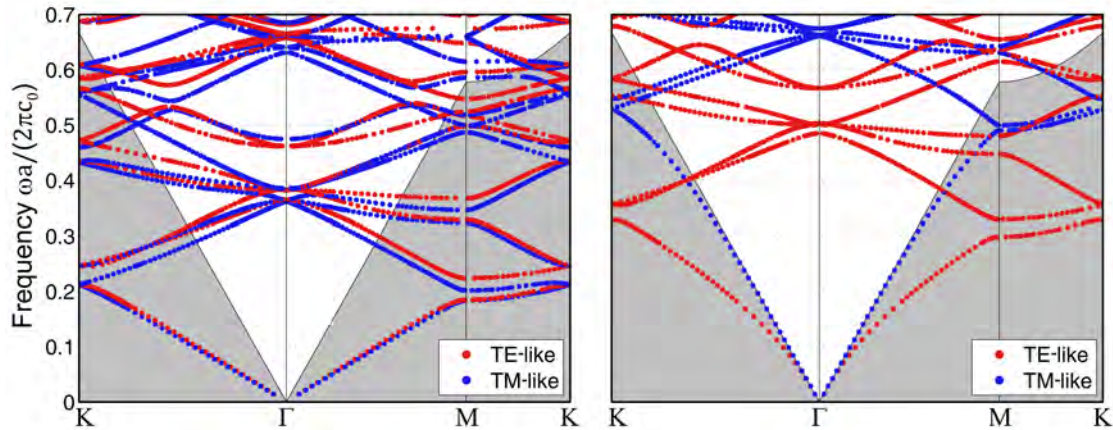


Figure 3.17: Comparison of the photonic band structure of a “real” 2D photonic crystal (left) and a triangular photonic crystal slab (right). The photonic crystal dimensions are  $a = 4.0 \mu\text{m}$ ,  $r/a = 0.2$  and for the PCS slab thickness  $d = 1 \mu\text{m}$ . The thinner the slab waveguide, the more the mode leaks into the surrounding medium and the further the photonic bands are pushed to higher frequencies. The shift is different for TE-like and TM-like modes. (Published in [185])

The thickness of the slab has a huge impact onto the photonic band structure, in particular when the thickness is close to or below the wavelength. The more the mode leaks into the surrounding medium, the further the photonic band are pushed to higher frequencies. The shift is also different for TE-like and TM-like modes (Fig. 3.17b).

## 4 Photonic Crystal QWIPs

A photonic crystal QWIP is a photonic crystal structure is fabricated from QWIP material. The motivation to create such devices is to increase the photoresponse of the detector using a resonator without increasing the detector noise. This concept is known as resonant cavity enhancement and was discussed in sections 1.1 and 2.3.3.

The advantage of photonic crystals compared to other resonator structures is fulfillment of two functions at once. Photonic crystals are excellent resonators with designable Q-factors ranging from  $10^0$  to  $10^7$ . Additionally, they support numerous optical modes, which can be designed and adjusted to the specific application. In section 2.1 it was shown that QWIPs are sensitive only to electric fields in confinement direction, hence they are not sensitive to surface-normal incident light. Photonic crystals provide the polarization conversion of the incoming light by coupling free space modes to TM-like photonic crystal modes, which have the proper electric field polarization to be absorbed by the QWIP.

The vertical mode confinement in the photonic crystal is essential for the performance of the final device. Two different waveguide designs are presented: 1) plasmon-enhanced waveguides with a thin gold layer on top of the photonic crystal and 2) purely dielectric slab waveguides with an air gap below the slab.

The photonic crystal QWIPs with a plasmon-enhanced waveguide will only be discussed briefly, since these devices were the subject of previous work and a detailed investigation can be found in [160]. The focus in this chapter is on photonic crystal slab QWIPs, in particular on performance enhancement.

### 4.1 Design and Fabrication

In this section the design and fabrication of standard mesa QWIPs and photonic crystal QWIPs is discussed. All QWIPs were grown on the in-house MBE, which greatly simplified material requests. The heterostructure design was developed in close collaboration with the MBE growth team. In the development process of the PCS-QWIPs several heterostructure designs were grown and investigated. The samples referenced in this chapter are only the optimized designs.

### 4.1.1 Standard Mesa QWIPs

The quantum design of the QWIP heterostructure is calculated using a self-written Schrödinger-Poisson solver searching for self-consistent solutions. The heterostructure is simulated for an applied electric field of  $10 \text{ kV/cm}$ , which results in a tilted conduction band. The excited electronic state is designed as a quasi-bound state close to the barrier energy, such that the electrons can easily escape the quantum well. The conduction band design of the standard QWIP sample H491, designed for a wavelength of  $\lambda \approx 8.3 \mu\text{m}$ , is shown in figure 4.1.

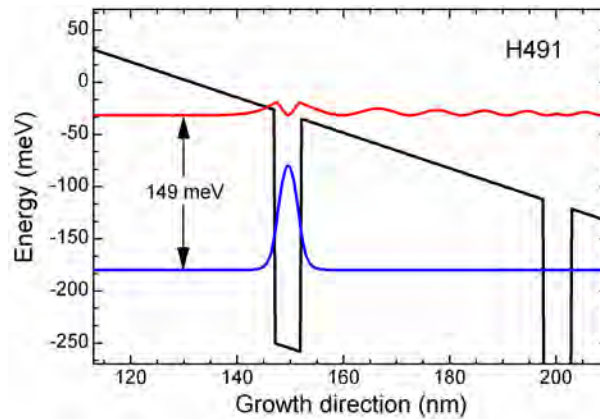


Figure 4.1: Electronic conduction band and probability density functions of the QWIP H491.

The model for this simulation considers only a single electron in perfectly parabolic quantum wells, hence the calculated intersubband transition energy deviates from experimental values. A more accurate model should consider the non-parabolicity of the subbands and include many body effects, especially in high doped quantum wells. For a detailed analysis of the necessary correction terms refer to [37].

From the electronic conduction band simulation the dimensions and material compositions for the MBE growth sheet are extracted. To allow backside illumination of the photodetector, the heterostructure is grown on a semi-insulating GaAs substrate. The bottom contact is a  $500 \text{ nm}$  doped GaAs layer, followed by the active region, and a  $100 \text{ nm}$  top contact layer (Tab. 4.1).

The active region consists of 40 quantum wells. In a standard QWIP the number of quantum wells is determined by noise considerations, the desired total absorption and the maximum heterostructure thickness. If the heterostructure functions also as a waveguide, then the number of quantum wells is additionally determined by the optical wave guide design (Fig. 4.2).

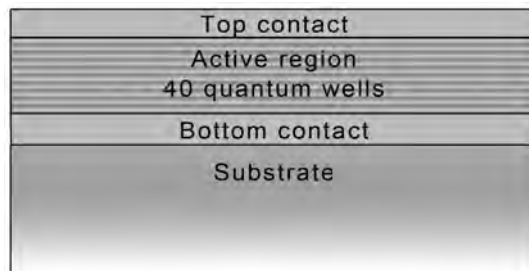


Figure 4.2: Heterostructure of the standard QWIP H491. The thickness of the active region is  $2.03 \mu m$ , the total thickness of the heterostructure is  $2.68 \mu m$ .

The doping concentration in the quantum wells influences the absorption efficiency and the dark current at the same time. Depending on the application, the QWIP can be optimized for high detectivity or for high BLIP temperature by choosing the right doping level [44]. The doping concentration in the contact layers is generally chosen as high as possible to guarantee good ohmic contacts. However, if the heterostructure is also a waveguide, then a high contact layer doping can introduce large waveguide losses due to free carrier absorption, and the contact layer doping concentration would be chosen lower. The sum of all this information finally results in the MBE growth sheet (Tab. 4.1).

Layer	Thickness	Composition	Doping	Description
	nm	% Aluminum	n-type	
Substrate	$650 \mu m$		semi-insulating	GaAs Substrate
Si:GaAs	500		$2 \times 10^{18} cm^{-3}$	Contact layer
<i>Loop 40</i>				
AlGaAs	45	30%		Barrier
GaAs	1			Well
Doping			$4 \times 10^{11} cm^{-2}$	Silicon $\delta$ -doping
GaAs	3.5			Well
<i>End Loop</i>				
AlGaAs	45	30%		Barrier
AlGaAs	55	30% $\rightarrow$ 0%		Barrier gradient
Si:GaAs	100		$1 \times 10^{18} cm^{-3}$	Contact layer

Table 4.1: Growth sheet of the QWIP structure H491.

Standard QWIPs are fabricated by etching  $100 \times 100 \mu m$  mesa from the QWIP heterostructure. The etch depth is controlled to slightly etch into the bottom contact. To collect the photocurrent,  $Ge/Au/Ni/Au$  contacts are deposited onto the top and

bottom contact layers. Finally, the metal contacts are annealed at 430°C to form ohmic contacts. A microscope image of the finished device is shown in figure 4.3.

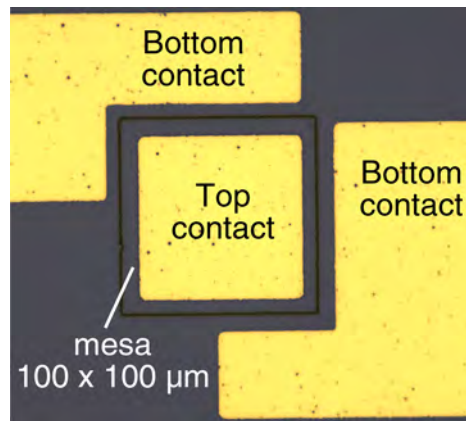


Figure 4.3: Microscope image of the finished standard QWIP H491.

### 4.1.2 Plasmon-Enhanced Photonic Crystal QWIPs

A straight forward way to process a photonic crystal from a QWIP heterostructure is to etch the photonic crystal pattern directly into the material. The problem with this approach is that the optical mode is not guided in the vertical direction. Since the average refractive index of the structured detector volume is generally lower than of the substrate, the light is not confined to the detector region and will vanish into the substrate. In this case the photonic crystal works only as a diffractive element, but not as a resonator.

A method to create a vertical waveguide is to deposit a layer of metal layer on top of the heterostructure. A metal/semiconductor interface supports a surface-plasmon mode, which propagates along the interface [190]. The metal is deposited before the photonic crystal pattern is etched into the heterostructure. The resulting layer stack supports a surface-plasmon mode, which is well confined to the detector region. (Fig. 4.4).

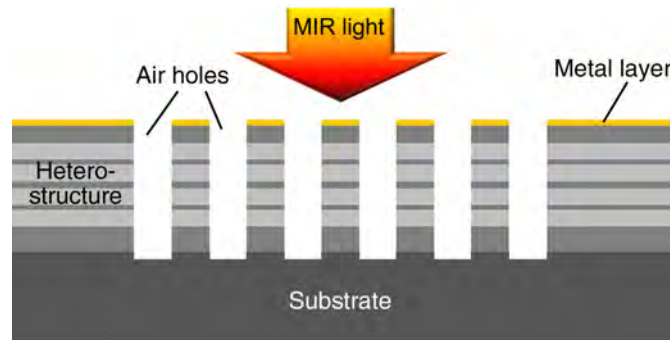


Figure 4.4: Schematic cross section of a plasmon-enhanced photonic crystal QWIP.

For a wavelength of  $\lambda = 7.8 \mu\text{m}$  of the incoming light, the simulation yields an overlap ratio of the surface-plasmon mode with the QWIP area (i.e. confinement factor) of  $\Gamma = 0.87$ . This value was calculated for the surface-plasmon waveguide without air holes. Due to the large refractive index of the metal, the maximum field intensity of the guided surface-plasmon mode is close to the metal layer (Fig. 4.5). When the photonic crystal is processed into the heterostructure, the average refractive index decreases, the mode is “pushed” into the substrate and the confinement factor decreases. A detailed analysis of the surface-plasmon waveguide properties for PC-QWIPs can be found in [160].

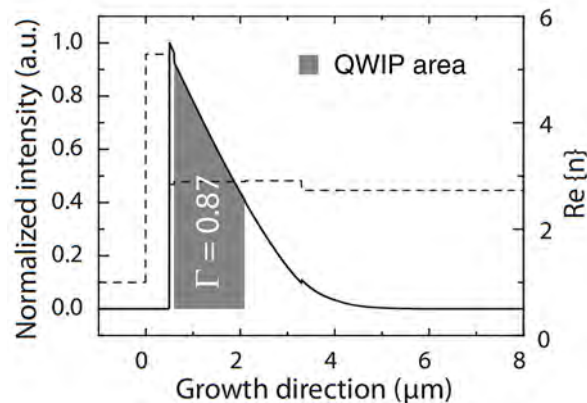


Figure 4.5: Mode profile (solid line) and refractive index profile (dashed line) of the surface-plasmon mode in a plasmon-enhanced photonic crystal QWIP. The waveguide mode profile shows a relatively high confinement factor of  $\Gamma = 0.87$ . (Published in [160])

Modeling of the optical properties of a plasmon-enhanced PC-QWIP is relatively simple. The photonic band structure is calculated using the plane wave expansion method presented in section 3.3.1. Although a PC-QWIP is really a 3D structure, it is sufficient to use this 2D simulation. The third dimension is considered by introducing an effective refractive index  $n_{eff}$ , which is extracted from the one-dimensional waveguide simulation. This approximation is valid as long as the optical mode is well confined to the photonic crystal region. The PWEM simulated photonic band structure for a plasmon-enhanced PC-QWIP is shown in figure 4.6.

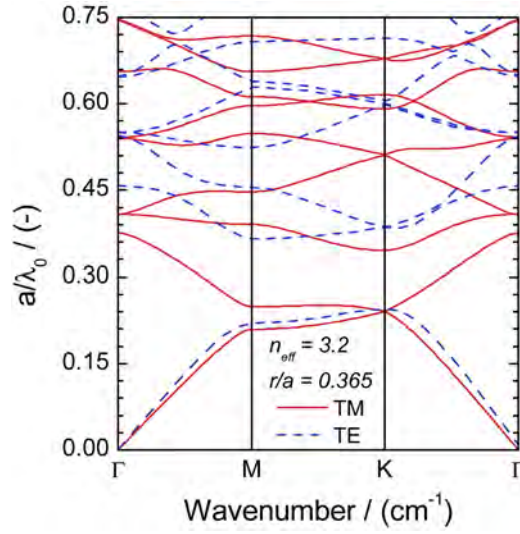


Figure 4.6: Simulated photonic band structure for a plasmon-enhanced photonic crystal QWIP with a normalized hole radius  $r/a = 0.365$ . (Published in [160])

The first step to fabricate a plasmon-enhanced PC-QWIP is to deposit a 50 nm thick  $Ge/Au/Ni/Au$  layer onto the QWIP heterostructure. This layer forms the surface-plasmon waveguide and is used as electrical top contact to collect the photocurrent. Next, the photonic crystal pattern is written into a photoresist by laser direct patterning. Then the pattern is transferred into a  $SiN_x$  hard mask by reactive ion etching. The metal layer is structured by Argon sputtering, which mechanically removes the metal. The semiconductor heterostructure is etched by a  $SiCl_4$  plasma. The heterostructure around the photonic crystal is also removed by reactive ion etching to form mesa with a defined detector area and limit the dark current flow. The sidewalls of the PC-QWIP mesa are insulated with  $SiN_x$ . Extended  $Ti/Au$  contacts are deposited for wire bonding. Finally, all metal contacts are annealed at 430°C to form ohmic contacts (Fig. 4.7a). For a detailed description of all processing steps refer to [160].

Etching of the metal layer is a challenging process step, since the metal is very resistant and introduces roughness during the etch process to the sidewalls of the photonic crystal holes (Fig. 4.7b). In this damaged region the average hole diameter is larger than at the bottom of the hole. Since the photonic band structure strongly depend on the hole diameter, this effect influences the resonant optical properties of the photonic crystal.

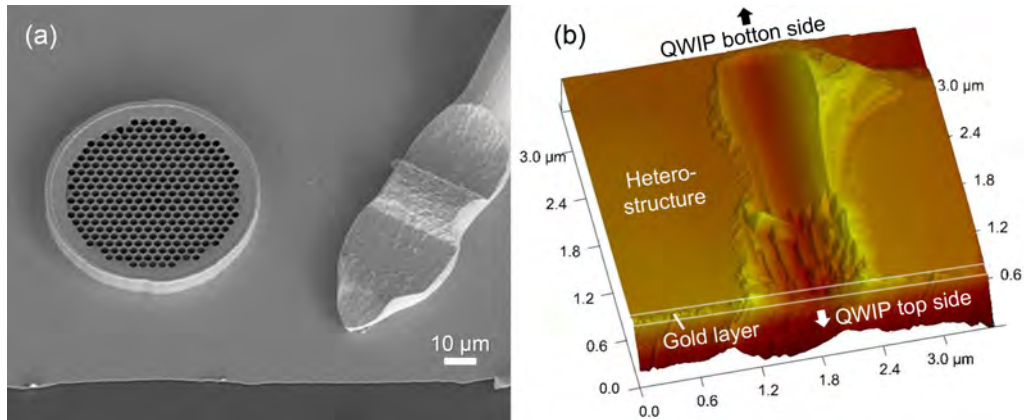


Figure 4.7: Plasmon-enhanced photonic crystal QWIPs. (a) SEM image of the finished devices. (b) Atomic force microscopy topography image of a photonic crystal hole. Close to the gold layer (QWIP top side), the surface of the sidewalls inside the holes is rough. In this region the average hole diameter is different than on the bottom of the hole, which influences the optical properties of the photonic crystal. (Image (a) published in [160])

A drawback of the plasmon-enhanced waveguide are the relatively high waveguide losses. Low waveguide losses are important in photonic crystal resonators, otherwise the quality factors of the photonic crystal resonances are low.

### 4.1.3 Photonic Crystal Slab QWIPs

A purely dielectric photonic crystal structure can show very high Q-factors, but the optical mode needs to be confined in the vertical direction. With a standard GaAs QWIP layer structure this is not possible, since the refractive index of the GaAs substrate is higher than the average refractive index of the heterostructure. To enable good waveguiding in such a device, an additional layer is grown below the QWIP heterostructure. The highest index contrast is between semiconductor material and air. Therefore this additional layer is grown as a sacrificial layer, which is removed later in the fabrication process (Fig. 4.8).

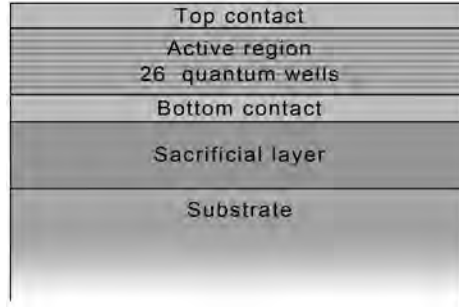


Figure 4.8: Heterostructure of the photonic crystal slab QWIP H661. The thickness of the active region is  $1.33 \mu m$ , the thickness of the sacrificial layer is  $2.00 \mu m$ , the total thickness of the heterostructure (including sacrificial layer) is  $4.00 \mu m$ .

Two PCS-QWIP materials were grown, which differ only in the quantum well doping: H661 with a doping concentration of  $4 \times 10^{11} cm^{-2}$  and H681 with a doping concentration of  $4 \times 10^9 cm^{-2}$ . From both materials standard QWIPs and PCS-QWIPs are processed. The doping concentration of H661 was chosen according to the guidelines for a detectivity optimized detector design [44]. The quantum wells in H681 were doped  $100\times$  lower than in H661. The absorption peak of both samples is around a wavelength of  $\lambda = 8 \mu m$ . The ISB transition is designed to be a bound-to-quasibound transition. A comparison of the properties of H661 and H681 is shown in table 4.2. The growth sheets for both materials are in Appendix A.

Name	<b>H661</b>	<b>H681</b>
Function	PCS-QWIP	PCS-QWIP
Doping	high ( $4 \times 10^{11} cm^{-2}$ )	low ( $4 \times 10^9 cm^{-2}$ )
Design	30% Al content in barrier 4.5 nm well width 45 nm barrier width 26 wells	30% Al content in barrier 4.5 nm well width 45 nm barrier width 26 wells
Sacrificial layer	yes, $d = 2 \mu m$	yes, $d = 2 \mu m$
Substrate	semi-insulating	n+ doped ( $1 \times 10^{18} cm^{-3}$ )

Table 4.2: Properties of the QWIP materials H661 and H681.

The photonic crystal is etched directly into the heterostructure. When the sacrificial layer below the detector region is removed, a free standing photonic crystal slab surrounded by air is left (Fig. 4.9). The doped contact layers on top and bottom of the slab are used to collect the photocurrent.

The material composition of the sacrificial layer is  $Al_{0.85}Ga_{0.15}As$ , which is challenging for the MBE growth. The crystal quality of the sacrificial layer needs to be maintained very high to ensure a low defect density in the heterostructure. At the same time the strain induced by any lattice mismatch needs to be kept low, otherwise the membrane will bend or even break after release.

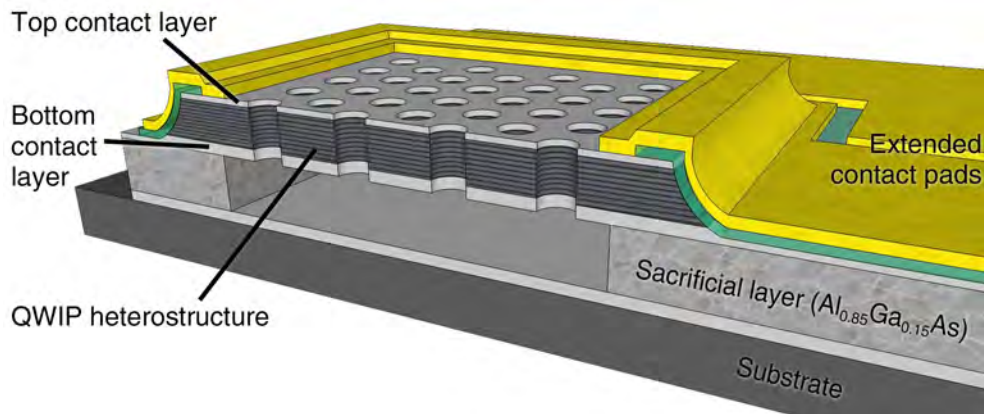


Figure 4.9: Schematic device structure of a photonic crystal slab QWIP. (Published in [117]).

**Slab Waveguide** The thicknesses of the photonic crystal slab and of the air gap below the slab can be adjusted to optimize the detector performance. The maximum intensity of the optical slab mode is located approximately in the center of the slab, which guarantees an excellent overlap with the detector region. For a slab waveguide with a slab thickness of  $2\ \mu m$  at a wavelength of  $\lambda = 8\ \mu m$  the confinement factor  $\Gamma = 0.84$  (Fig. 4.10a).

The slab thickness is chosen to support only a single guided mode at the desired operation wavelength. At shorter wavelengths the slab waveguide can also guide higher order slab modes (Fig. 4.10b). For each additional slab mode, new photonic crystal modes will appear in the detectors photoresponse [191]. While higher order modes present an interesting research topic by themselves, they are usually undesirable for detectivity optimization and need to be suppressed by the detector design.

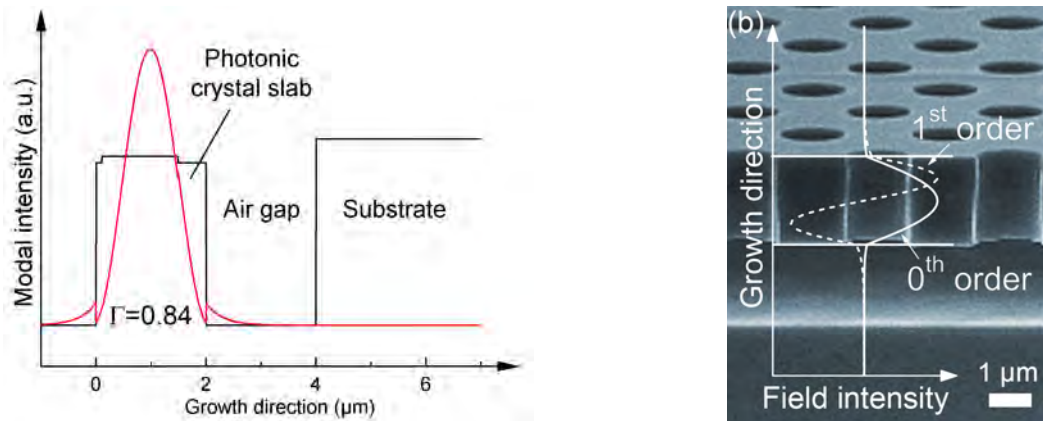


Figure 4.10: Slab waveguide design. (a) Refractive index profile (black line) and mode profile (red line) for a slab thickness of  $2 \mu\text{m}$  and a wavelength  $\lambda = 8 \mu\text{m}$ . (b) SEM image of the photonic crystal slab, overlaid with a  $0^{\text{th}}$  order and a  $1^{\text{st}}$  order slab mode. (Published in [192])

The thickness of the air gap below the photonic crystal slab can be engineered to reflect the light back to the detector region. The result is a higher total absorption than a photonic crystal slab QWIP in free space could achieve. A simulation for varying air gap thickness shows, that the optimum slab thickness is exactly a quarter of the design wavelength  $\lambda = 8 \mu\text{m}$  (Fig. 4.11).

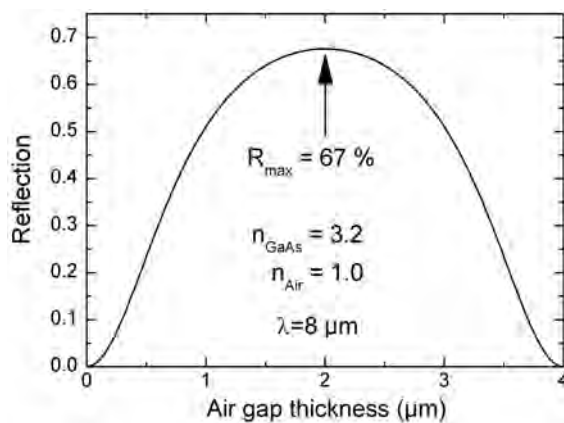


Figure 4.11: Optimum air gap thickness.

**Photonic Band Structure** The band structure of the photonic crystal slab is simulated with the revised plane wave expansion method (see section 3.3.3). Since the

effective refractive index of the slab waveguide changes significantly with the frequency, a frequency dependent permittivity is introduced into the simulation (Fig. 4.12).

Using the revised PWEM, the photonic band structure is designed to overlap with the sensitive frequency range of the QWIP. The photonic crystal mode with a dipole-like in-plane symmetry is placed at the QWIP peak absorption frequency, since these modes couple very efficiently to free space modes. From this simulation the photonic crystal dimensions (lattice constant  $a$ , hole radius  $r/a$ ) are determined.

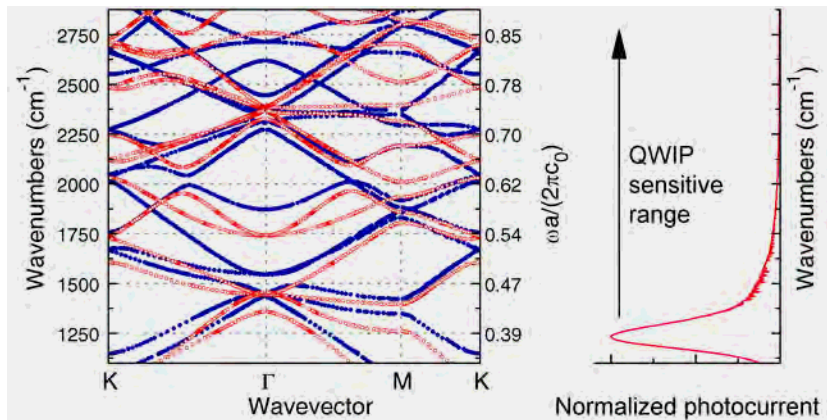


Figure 4.12: Photonic band structure of a photonic crystal slab. The band structure is simulated with the revised plane wave expansion method. The photonic crystal is designed such that the photonic bands overlap with the QWIP sensitive range. (Published in [117])

**Fabrication Process** The fabrication of a PCS-QWIP starts by deposition of a layer of photoresist onto the QWIP sample (Fig. 4.13a). The photonic crystal pattern is written into the photoresist by laser direct writing. The spatial resolution of the used laser writing system is  $\approx 500\text{ nm}$ . This resolution is sufficient since the diameter of the photonic crystal holes is typically  $> 1\ \mu\text{m}$ . To process smaller structure the use of electron beam lithography becomes necessary.

The photonic crystal pattern is transferred into the heterostructure by  $\text{SiCl}_4$  reactive ion etching (Fig. 4.13b). The selectivity of the etch process between photoresist and the  $\text{GaAs}/\text{AlGaAs}$  heterostructure is relatively high, so the holes can be etched several micrometers deep without problems. Only for small photonic crystal holes ( $< 1\ \mu\text{m}$ ) the process becomes more challenging, since the etch rate depends on the hole diameter (see Appendix B). The etched surface is relatively smooth and the hole radius is constant across the entire slab (Fig. 4.10b).

To define the device area and limit the current flow, mesas are fabricated by etching the heterostructure around the photonic crystal. The etch depth needs to be controlled very well to hit the bottom contact layer. The mesa fabrication process is done by wet chemical etching with diluted  $H_3PO_4$  acid (Fig. 4.13c). This allows to easily interrupt the etch process and measure the mesa height.

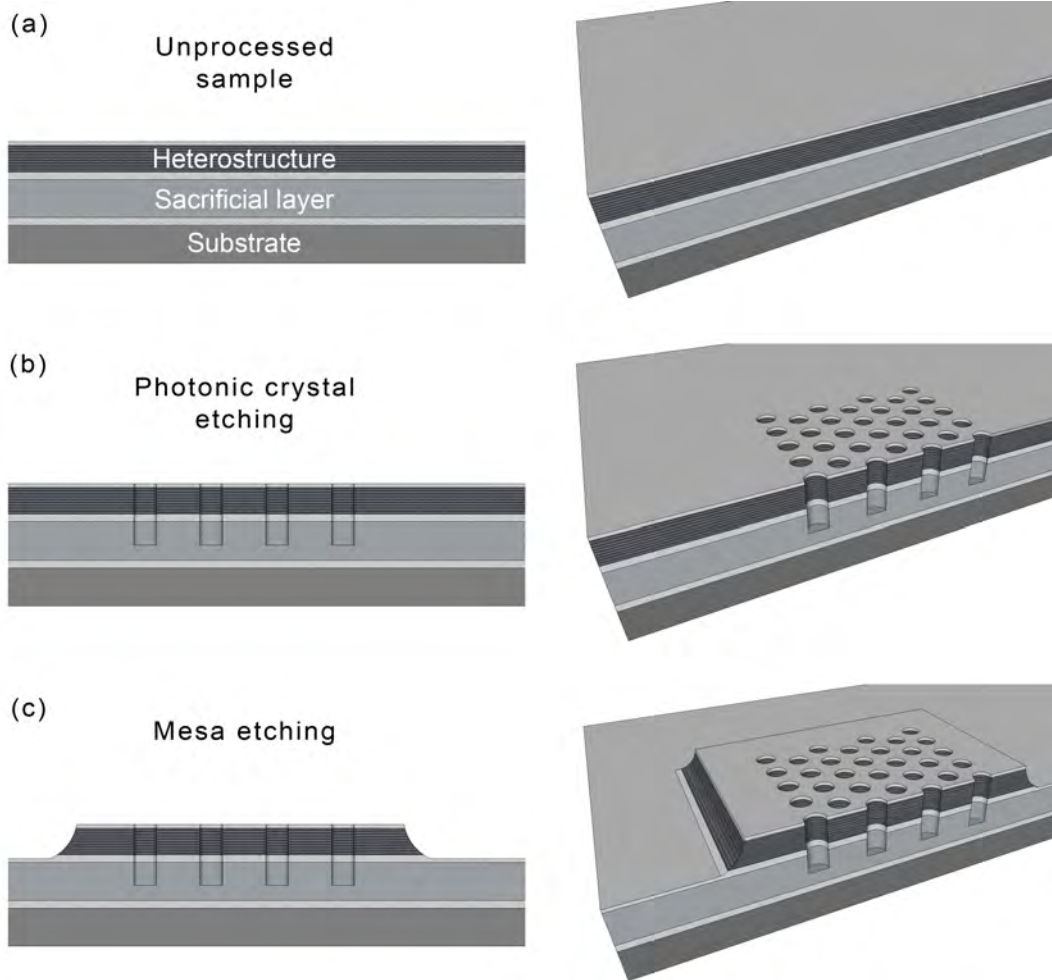


Figure 4.13: Processing steps for a photonic crystal slab QWIP I.

Consecutively, the sidewalls of the mesa are insulated by silicon nitride (Fig. 4.14a). This protects the heterostructure from short circuiting with the metal contacts. The  $SiN_x$  is deposited onto the entire sample, also inside the photonic crystal holes. This unwanted  $SiN_x$  layer needs to be removed before the processing is continued by  $SF_6$  reactive ion etching. Any remaining  $SiN_x$  layer will later disturb the sacrificial layer etching (see Appendix B).

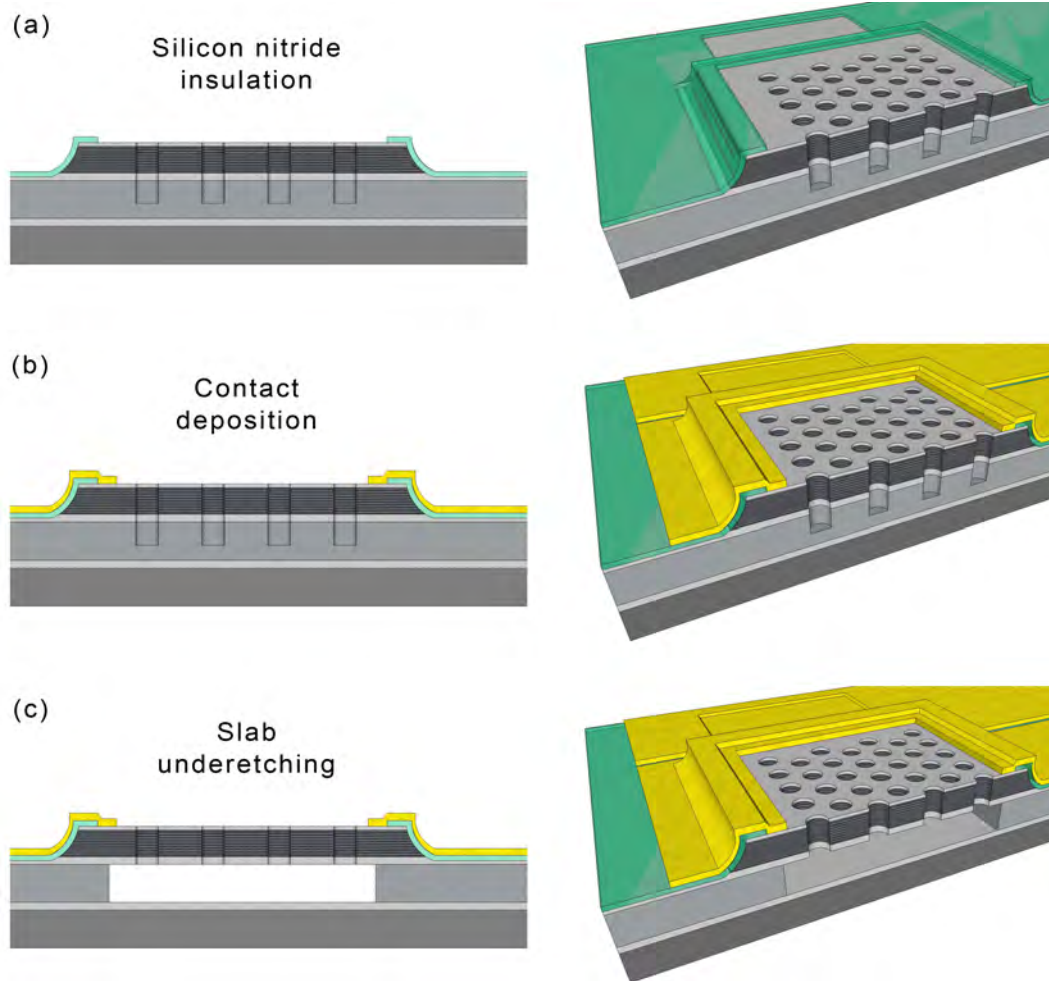


Figure 4.14: Processing steps for a photonic crystal slab QWIP II.

The metal contacts are deposited in a two-step process. A  $50\text{ nm}$  thick  $Ge/Au/Ni/Au$  layer is deposited by electron beam evaporation to form good ohmic contacts. Next a  $Ti/Au$  layer is sputtered to cover the mesa sidewalls and form extended contact pads. (Fig. 4.14b).

The final processing step is the photonic crystal slab underetching (Fig. 4.14c). The sacrificial layer is removed with diluted  $HCl$  acid, leaving a free standing membrane. To protect the metal contacts during the underetch process, they are covered with a thick film of photoresist. To reduce tensile forces, which occur during sample drying, the water is replaced by methanol ( $CH_3OH$ ). If the tensile forces are too strong, the photonic crystal slab will break. After annealing the metal contacts at  $430^\circ\text{C}$  the device is finished.

Figure 4.15 shows a SEM image of a finished PCS-QWIPs. On this sample several different photonic crystals patterns were processed, resulting in different photocurrent spectra.

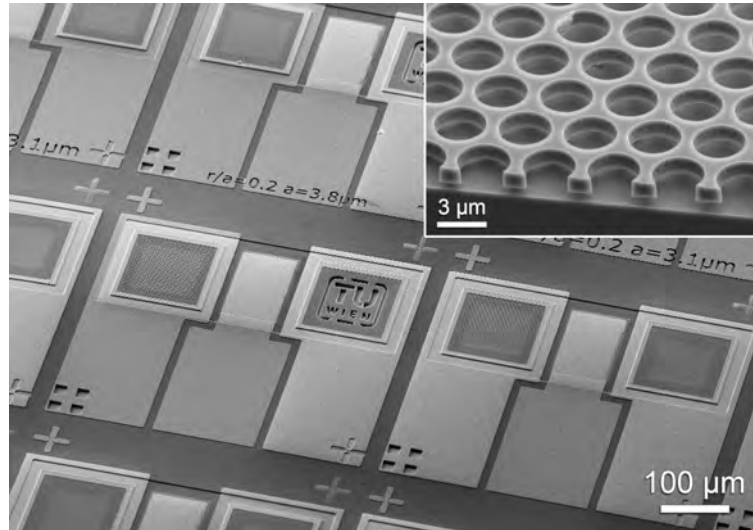


Figure 4.15: SEM image of finished PCS-QWIPs. The devices were processed with several different photonic crystals patterns, resulting in different photocurrent spectra. For public relation purposes the devices in the center were fabricated with the logo of the Vienna University of Technology. Inset: SEM image of cleaved photonic crystal slab.

## 4.2 Experimental Results

This section is a summary of the experimental results from measurements on standard and photonic crystal QWIPs. The measurement and data analysis techniques are discussed in the standard QWIP section, but they equally apply to the photonic crystal QWIP measurements.

### 4.2.1 Standard Mesa QWIPs

**Measurement Setup** Standard mesa QWIPs are illuminated through a  $45^\circ$  wedged facet from the backside of the sample (Fig. 4.16a). The reflectivity of the polished facet is  $\approx 30\%$ . The mid-IR radiation is generated by a Globar inside a Fourier transform infrared spectrometer (FTIR). The broad light beam is then focused with a ZnSe lens through the cryostat ZnSe window onto the QWIP. The photocurrent signal from the QWIP is amplified with a transimpedance amplifier and fed back into the FTIR.

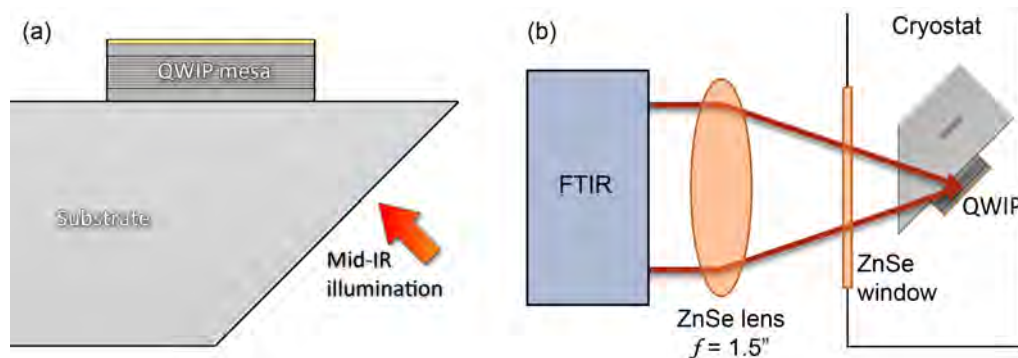


Figure 4.16: Standard QWIP measurement setup. (a) Standard QWIPs are illuminated through a  $45^\circ$  wedged facet from the backside of the sample. (b) The mid-IR light from a Fourier transform infrared spectrometer is focused with a ZnSe lens onto the QWIP.

**Spectral Photoresponse** The spectral photoresponse of the standard QWIP shows a peak at the intersubband transition energy (Fig. 4.17). The exact peak position and shape depends on the design and MBE growth conditions, and shows some variations between different growth runs.

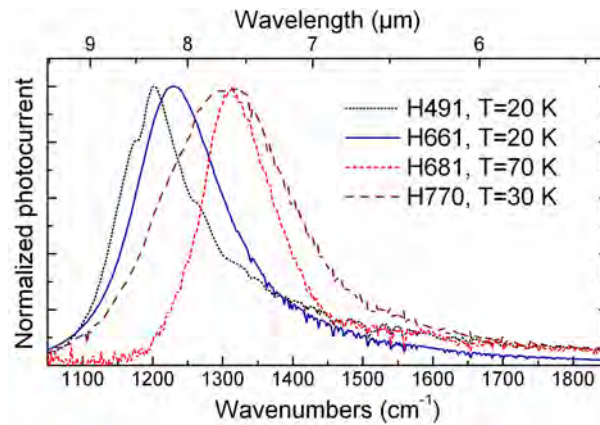


Figure 4.17: Spectral photocurrent response of standard QWIPs. All QWIPs were designed with 30% Al content, 4.5 nm well width and 45 nm barrier width. The exact peak position and shape depends on the MBE growth conditions.

The measured photocurrent spectrum is influenced by several factors, which need to be corrected to get the true photoresponse of the detector. Since the optical beam path is partly in air, the atmosphere causes numerous absorption peaks in the photocurrent spectrum. Additionally, the Globar emission intensity is not constant over the full spectral range. These two influences are corrected by normalizing the measured photocurrent response by a Globar emission spectrum measured through air (Fig. 4.18a).

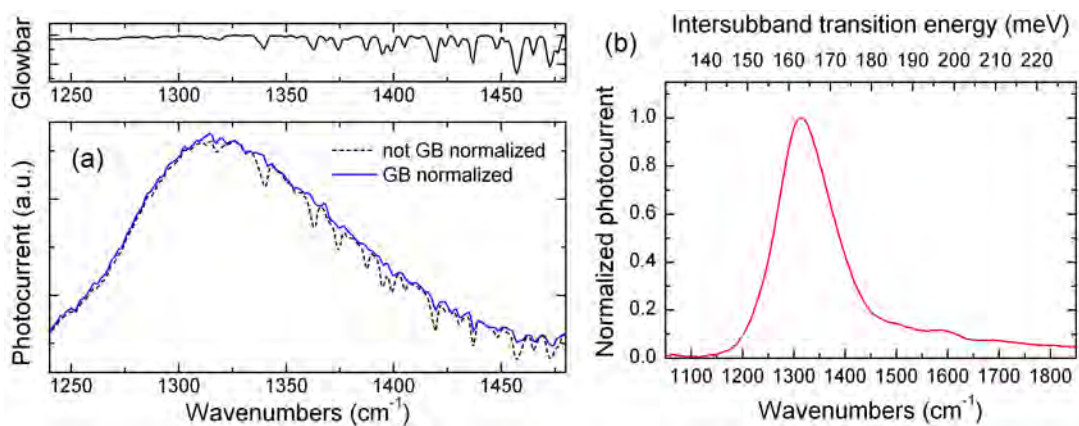


Figure 4.18: Normalization of the photocurrent response. (a) The QWIP photocurrent spectrum is normalized by a Globar emission spectrum measured through air. This way the influences of the atmospheric absorption and the Globar emission spectrum are corrected. (b) Corrected photocurrent spectrum measured from the low doped standard QWIP H681.

An additional influence on the photocurrent spectrum is presented by the substrate absorption. If the substrate is semi-insulating, this contribution is very small and can be neglected. For doped substrates free-carrier absorption becomes significant and needs to be considered. The absorption depends on the length of the light path through the substrate and the doping concentration. The high doped QWIP material H661 was grown on semi-insulating substrate, therefore no correction is necessary. The low doped QWIP material H681 was grown on n+ doped substrate with a doping density of  $1 \times 10^{18} \text{ cm}^{-3}$ , which makes a correction of the photocurrent spectrum necessary. A description of the absorption model and the applied correction is given in Appendix C.

The corrected photocurrent spectrum measured from the standard mesa QWIP H681 is shown in figure 4.18b. The peak magnitude is normalized, since it was not possible to determine the responsivity in this measurement. To assign absolute responsivity values to the measured spectra the optical power on the QWIP has to be determined precisely. The measurement setup to obtain absolute responsivity values is explained later in this section.

**Electrical Properties** The I-V characteristics of the standard QWIPs processed from the material H661 and H681 are shown in figure 4.19. The dark current of the low doped QWIP H681 is two orders of magnitude lower compared to the high doped QWIP H661, which is a result of the  $100\times$  lower doping density. The temperature dependence of the dark current density at  $-2V$  bias voltage is shown in figure 4.20. At low temperatures the dark current of the high doped QWIP H661 is constant, since it is dominated by background radiation. In the low doped QWIP H681, the dark current is also dominated by background radiation. The dark current decreases because the carriers start to freeze out at temperature below  $70 \text{ K}$ .

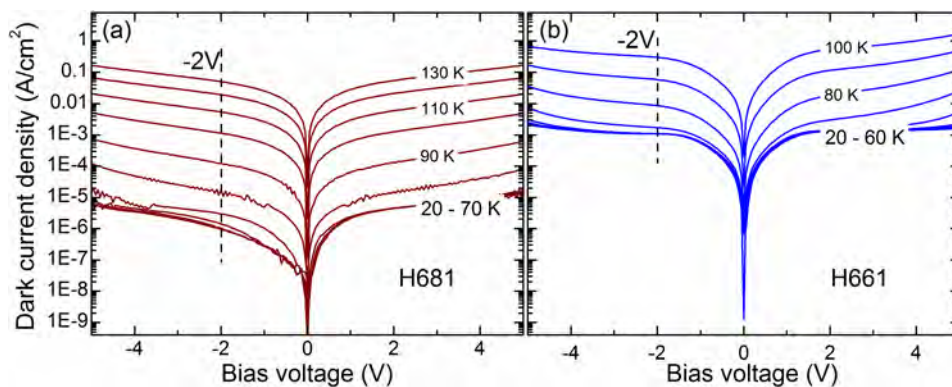


Figure 4.19: I-V characteristics of the QWIPs H661 and H681. The dashed line marks the sampling points for the curves in figure 4.20.

The BLIP temperature of the QWIPs H661 and H681 was found at 69 K and 75 K, respectively. Above  $T_{BLIP}$  the dark current is dominated by thermal carrier excitation. Since the barriers are relatively thick (45 nm), sequential tunneling plays only a minor role.

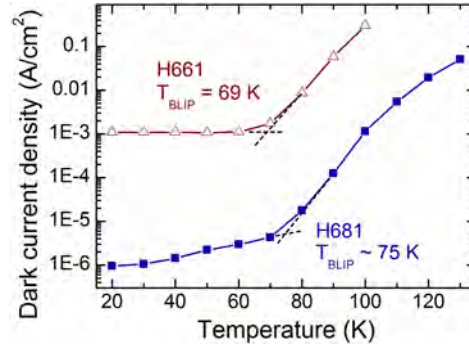


Figure 4.20: Temperature dependence of the dark current density. The dark current of the low doped QWIP H681 is two orders of magnitude lower compared to the high doped QWIP H661. At temperatures below 70 K, the carriers in the low doped QWIP H681 start to freeze out.

**Responsivity** The responsivity of a photoconductive QWIP is defined as

$$\mathcal{R} = \frac{I_{ph}}{P_{opt}}$$

To accurately measure the responsivity of a photodetector, the optical power on the detector surface and the photocurrent have to be measured precisely. While the measurement of the photocurrent is relatively easy using an electrical Ampere-meter, it is more difficult to accurately determine the optical power. The light source has to be well defined spatially and spectrally to measure correct values. A simple method for incoherent light sources is to place an optical band pass filter and a tiny aperture in front of the detector. This results in a homogeneous illumination of the detector with a well defined area and known bandwidth. However, since the optical output power of a Globar is limited, the light intensity on the detector surface is usually very low.

A more advanced, but also more complex approach is to illuminate the detector with a coherent light source, in this case with a single-mode quantum cascade laser (Fig. 4.21). The advantage of a single-mode laser is that the emission bandwidth is very well defined. Further, coherent light can be focused very well to a beam diameter in the range of

several wavelengths. The optical power on the detector is orders of magnitude higher compared to an incoherent light source, which allows measurements also at high noise levels.

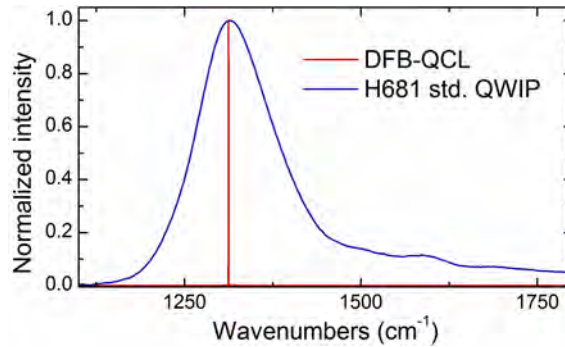


Figure 4.21: Responsivity measurement using a single-mode quantum cascade laser [193]. The bandwidth of the QCL is well defined. The emission frequency is tuned to be at the QWIP peak frequency using a distributed feedback (DFB) resonator.

The laser beam from the QCL is focused with a single ZnSe lens onto the QWIP. The divergence of the laser beam from the QCL is relatively large ( $\approx 30^\circ$ ), so a ZnSe lens with a short focal length ( $f = 1.5''$ ) and a large diameter is used to collect the light. The lens is placed at a distance of  $\approx 1.1 \times f$  away from the QCL facet. The focus is then at a distance of  $\approx 10 \times f$  behind the lens, where the cryostat with the QWIP is positioned. The cryostat is mounted on a three-axis stage to place the QWIP exactly in the focus of the laser beam (Fig. 4.22).

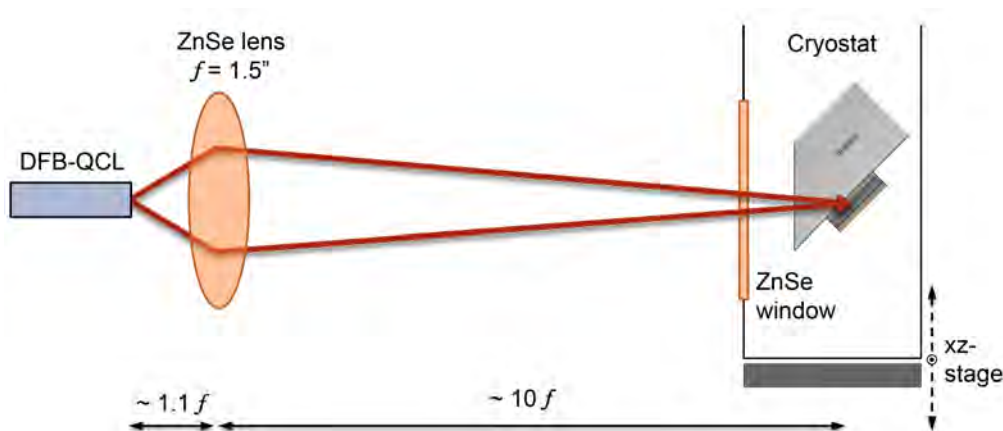


Figure 4.22: Responsivity measurement setup.

The laser was designed specifically for the responsivity measurements. To precisely hit the detector peak frequency, an array of DFB-QCLs was fabricated (Fig. 4.23a). Each DFB-QCL was processed with a different grating period, resulting in equally spaced emission frequencies. This allows selecting the QCL with the ideal emission frequency for a certain photodetector (Fig. 4.23b). This feature is less important for standard QWIPs, where the absorption spectrum is broad, but very useful for photonic crystal QWIPs with much narrower absorption peaks. All lasers allow continuous wave operation, which guarantees a stable emission spectrum and simplifies the optical power measurements.

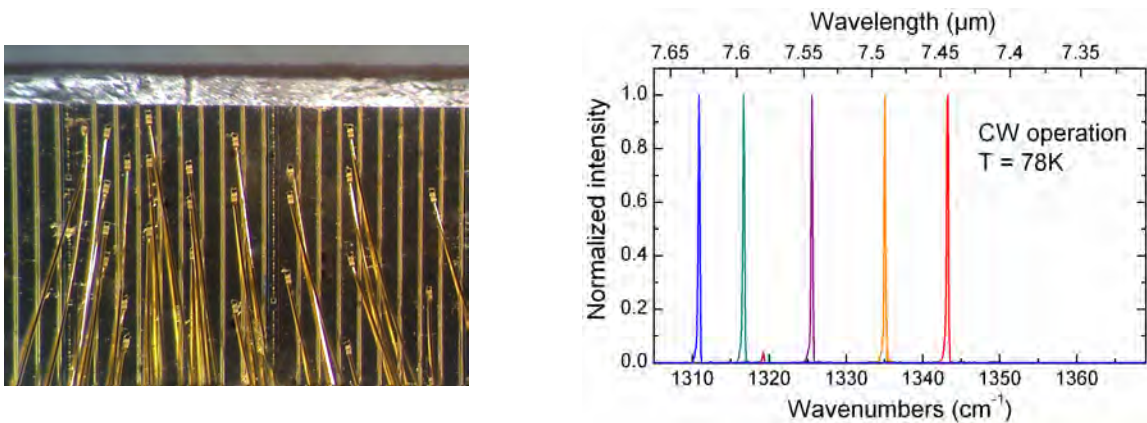


Figure 4.23: Array of DFB-QCLs for responsivity measurements. (a) Microscope image of the laser array. Each DFB-QCL is connected with several bond wires to ensure a homogeneous current distribution in the laser active region. (b) Normalized emission spectra of the DFB-QCLs. The lasers are operated in continuous wave mode at liquid nitrogen temperature.

The main disadvantage of this measurement setup is the inhomogeneous intensity distribution on the photodetector. To determine the optical power on the detector area, the beam profile needs to be measured. This is performed by using the QWIP itself. The stage is shifted stepwise in the vertical and in the horizontal direction, measuring a cross section of the beam. From this data the intensity distribution is extrapolated (Fig. 4.24). A description of the beam profiling method is given in Appendix D.

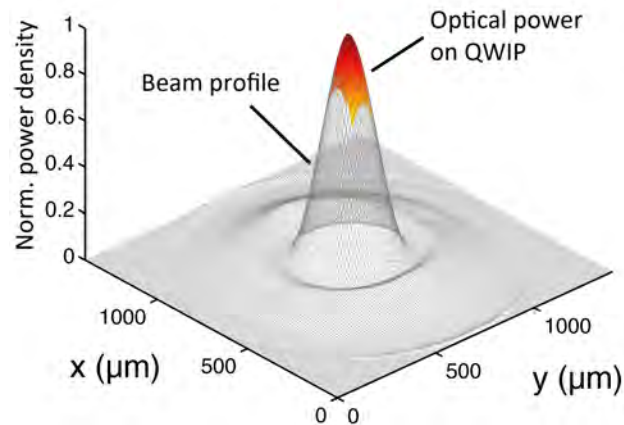


Figure 4.24: Beam profile at the focal point of the laser beam, used to determine the optical power on the detector.

The total optical power of the laser beam is measured with a laser power meter. From the beam profile the ratio of optical power on the QWIP to total optical power is determined.

The responsivity is calculated as the ratio of measured photocurrent and optical power on the QWIP area (Fig. 4.25). With increasing temperature the responsivity also increases. At temperatures below  $\approx 70\text{ K}$  the increase is caused by activation of dopants. This effect is visible primarily in the low doped QWIP samples. At high temperatures the responsivity increase can be attributed to the thermally assisted carrier extraction from the quantum wells.

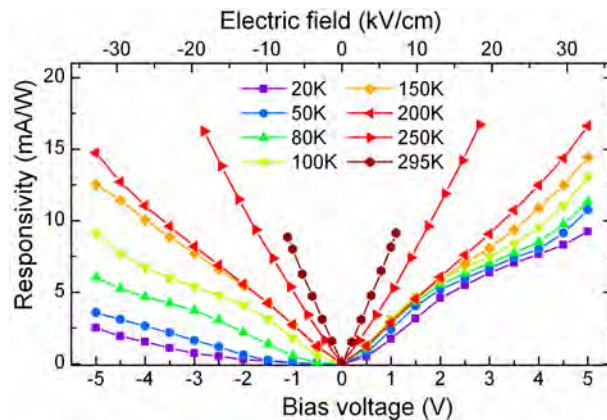


Figure 4.25: Responsivity of the low doped standard QWIP H681. The responsivity is calculated as the ratio of measured photocurrent and optical power on the QWIP area. (Published in [192])

The continuous increase of responsivity with bias voltage is an indication for a bound-to-bound ISB transition. The higher the electric field, the higher is the extraction probability from the quantum wells and the higher is also the responsivity. If the excited state would be quasi-bound, a small bias voltage would already create a large photocurrent and further increasing the electric field would not significantly change the responsivity (see section 2.2.3).

**Noise Spectral Density** To quantify the detector performance, the measurement of the detector noise is as important as the detector responsivity. The noise current  $i_n$  of the QWIP is amplified with a transimpedance amplifier, which also converts the noise current  $i_n$  into a noise voltage. The noise voltage is then sampled with a FFT spectrum analyzer (Fig. 4.26). Since the noise currents are generally very low, a single measurement can take several minutes or even hours. To avoid interferences from the power grid, these measurements are best performed at night.

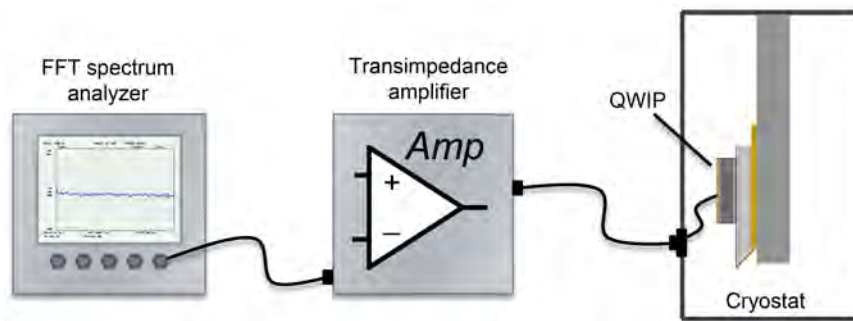


Figure 4.26: Noise measurement setup.

From the measured noise spectra, the noise current spectral density  $\mathcal{S}_n$  is calculated (Fig. 4.27). At low temperatures  $\mathcal{S}_n$  is dominated by the noise from the transimpedance amplifier. With increasing temperature the dark current noise increases and becomes the dominating noise source. The shape of the noise curves is similar to the dark current curves (Fig. 4.19), since the two quantities are directly related by Eq. 2.13.

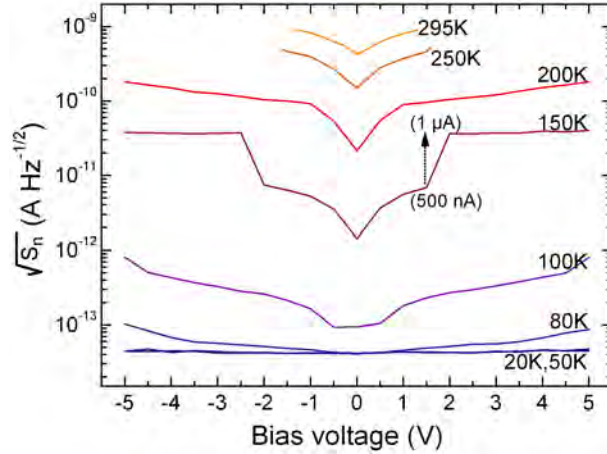


Figure 4.27: Noise current spectral density  $\mathcal{S}_n$  of the low doped standard QWIP H681. The jump in the 150 K curve is caused by a supply range switch of the built in current source from 500 nA to 1  $\mu$ A, which instantly makes it the dominating noise source.

The dark current can be separated into a DC component  $I_d$  and an AC noise component  $i_n$ . The DC component is compensated with a current source built into the transimpedance amplifier. However, the DC current source in the amplifier is a noise source itself. The jump in the 150 K curve in figure 4.27 is caused by a supply range switch of the built in current source from 500 nA to 1  $\mu$ A, which instantly makes it the dominating noise source. The curves at 250 K and 295 K could be measured only up to  $\pm 2$  V, since then the dark current became too large and saturated the amplifier.

**Detectivity** The specific detectivity  $D^*$  of the QWIP is calculated by

$$D^* = \frac{\mathcal{R}}{\sqrt{\mathcal{S}_n}} \sqrt{A}$$

where the detector area  $A$  is the electrically active area. In a standard QWIP the effective optical area is smaller than the electrically active area, since the QWIP mesa is illuminated at a  $45^\circ$  angle of incidence. The electrically active area (i.e. mesa size) of the low doped standard QWIP H681 is  $150 \times 150 \mu\text{m}$ .

The detectivity of the low doped standard QWIP H681 is shown in figure 4.28. The peak detectivity of  $2 \times 10^9 \text{ cm Hz}^{1/2}/\text{W}$  is relatively low compared to state of the art QWIPs with detectivities of  $10^{10} - 10^{11} \text{ cm Hz}^{1/2}/\text{W}$ . However, the device was not optimized for peak detectivity at low temperatures, but for low noise operation at high temperatures. The simple fact that the QWIP can be operated at room temperature with reasonable high bias voltages shows that this device has potential for high

temperature operation. The photonic crystal will help to improve the relatively low detectivity of the QWIP.

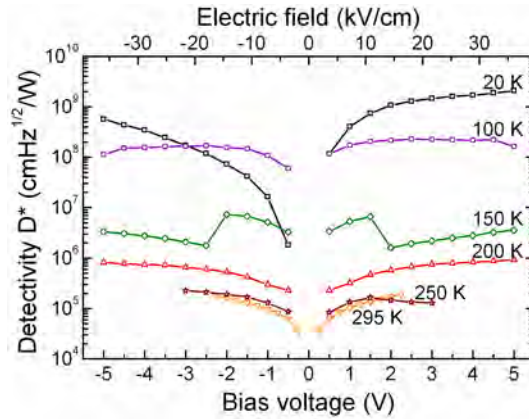


Figure 4.28: Detectivity of the low doped standard QWIP H681.

#### 4.2.2 Plasmon-Enhanced Photonic Crystal QWIPs

The spectral photoresponse of a plasmon-enhanced photonic crystal QWIP is shown in figure 4.29a. The sample was illuminated with surface-normal incidence light. The photocurrent spectrum shows one pronounced photocurrent peak and several smaller peaks. Each peak corresponds to a photonic crystal resonance (Fig. 4.29b).

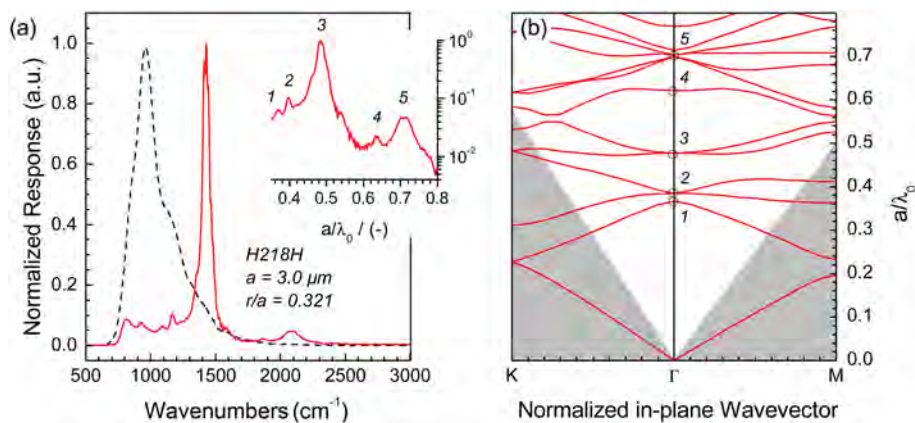


Figure 4.29: Photocurrent response of a plasmon-enhanced photonic crystal QWIP. (a) Photocurrent spectrum of a standard QWIP (dashed line) and a plasmon-enhanced PC-QWIP (solid line). (b) Each photocurrent peak of the PC-QWIP spectrum corresponds to a photonic band in the photonic crystal band structure. (Published in [160])

The strongest photocurrent peak (peak 3) corresponds to a dipole-like photonic crystal mode, which couples most efficiently to free space modes. All other photocurrent peaks are significantly smaller, since the in-plane symmetry of the free space mode and the photonic crystal modes are very different. A detailed discussion of photonic crystal symmetries and mode coupling can be found in [160].

The peak width of the photonic crystal resonances is relatively broad. The Q-factor of the strongest resonance in figure 4.29a is around  $Q \approx 50$ , while simulations would suggest much higher Q-factors between  $10^2 - 10^3$  [107, 123]. The reason is the high waveguide loss caused by the top metal layer. To get to higher Q-factors, a different type of waveguide with low absorption losses, such as purely dielectric slab waveguides, is necessary.

### 4.2.3 Photonic Crystal Slab QWIPs

**Measurement Setup** The photonic crystal slab QWIP is illuminated with surface-normal incident light (Fig. 4.30a). The mid-IR light is emitted from a Globar source inside the Fourier transform infrared spectrometer, and focused onto the QWIP with a ZnSe lens (Fig. 4.30b).

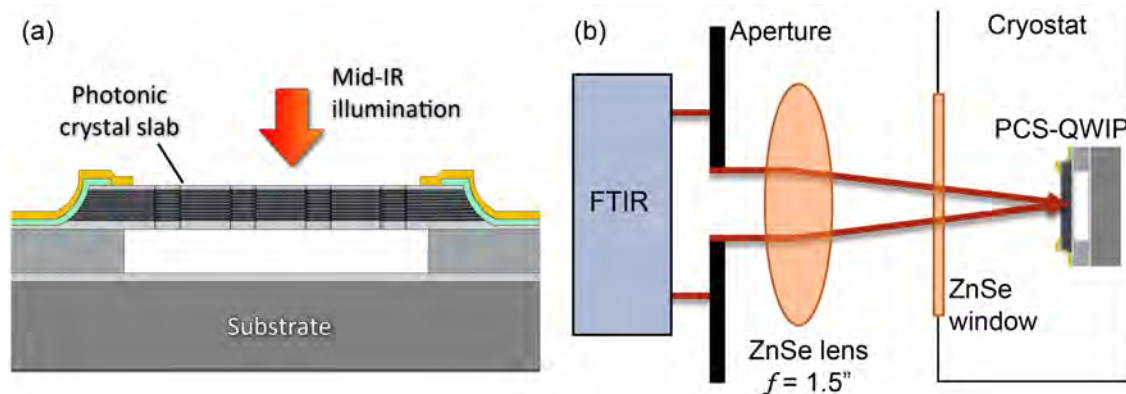


Figure 4.30: Optical setup for the spectral characterization of photonic crystal slab QWIPs. (a) The PCS-QWIPs are illuminated with surface-normal incident light. (b) The mid-IR light from the Fourier transform infrared spectrometer is focused onto the QWIP with a ZnSe lens. The opening angle of the focused beam is reduced by a 10 mm aperture, since the spectral response of the PCS-QWIP depends on the incident angle.

To be able to measure narrow resonances, the opening angle of the focused beam is reduced by an aperture. The in-plane wave vector of the photonic crystal modes depends on the in-plane wave vector of the incident light. If the opening angle is large, a broad range of photonic crystal modes will be excited with different in-plane wave vectors, which leads to significantly broader resonance peaks. The photocurrent from the QWIP is then amplified with a transimpedance amplifier and fed back into the FTIR.

**Spectral Photoresponse** The spectral response of the low doped PCS-QWIP H681 shows a broad peak at  $1250\text{ cm}^{-1}$ , which corresponds to the ISB transition energy of the QWIP (Fig. 4.31). Additionally, there are several pronounced resonance peaks, where each peak corresponds to a PCS resonance.

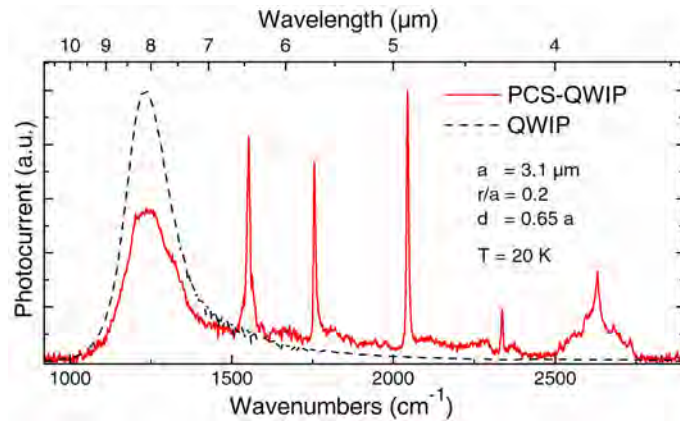


Figure 4.31: Photocurrent spectrum of the low doped PCS-QWIP H681 and the low doped standard QWIP H681 (dashed line). The PCS-QWIP spectrum shows pronounced resonance peaks, which correspond to the photonic crystal resonances. (Published in [117])

The photocurrent spectrum can be understood with the photonic crystal band structure (Fig. 4.32). The sample is illuminated at surface-normal incidence, so the in-plane wave vector of the PCS modes is zero ( $\Gamma$ -point). The energy transfer from free space to the photonic crystal modes is most efficient, if the in-plane symmetry matches. The first and second resonance peaks correspond to a TM-like and TE-like dipole mode, respectively. The reason, that the QWIP is sensitive also to TE-like modes, is that these modes are not pure TE modes. They have a significant electric field component also in the out-of-plane direction.

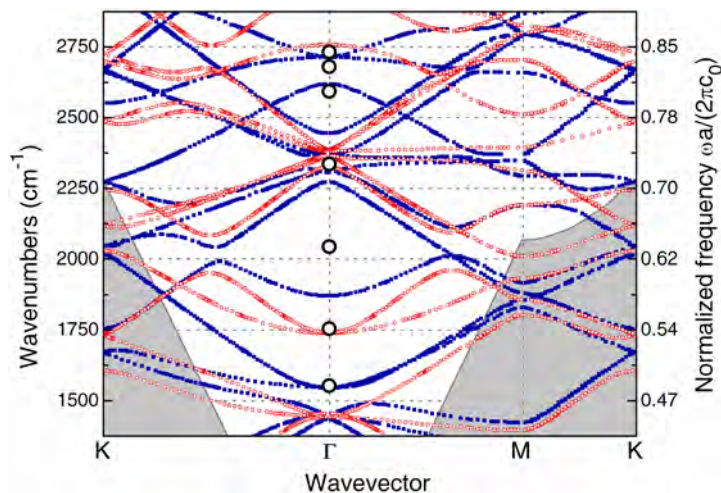


Figure 4.32: Photonic band structure for the  $0^{\text{th}}$  order slab waveguide mode, overlaid with the PCS-QWIP H681 resonances (large black circles). The band structure is separated into TM-like (blue squares) and TE-like (red circles) photonic bands. (Published in [117])

The third resonance in figure 4.32 (black circles at the  $\Gamma$ -point) appears to have no corresponding photonic band. This was explained by Gansch *et al.* who showed that also higher order slab modes exist in a PCS-QWIP. The photonic band structure of the higher order slab modes is shifted towards higher frequencies with respect to the band structure of the  $0^{\text{th}}$  order slab mode. [191]. The in-plane symmetry of the excited higher order slab modes is again dipole-like.

The peak widths of the PCS-QWIP resonances are significantly smaller as compared to the plasmon-enhanced PC-QWIPs. Since the slab waveguide is purely dielectric, the waveguide losses are relatively low. Q-factors up to  $Q \approx 300$  were measured for PCS-QWIPs. This number is in the range of the theoretically predicted values for guided resonances in purely dielectric photonic crystal slabs [123]. Since the PCS modes couple to free space modes, the photons in the PCS have a finite lifetime before they are radiated back into free space again.

**Responsivity** The responsivity of the PCS-QWIPs is measured with the same optical setup described for the standard QWIPs. The PCS-QWIP is illuminated with a focused single mode QCL. The beam profile of the focused beam is measured to determine the optical power on the detector. With this information the responsivity of the detector is calculated.

An important difference to the standard QWIP measurement is, that the absorption peaks of PCS-QWIPs are very narrow. If the laser frequency is not exactly at the

resonance peak center, the measured responsivity is not the peak responsivity, but some lower value. Additionally the PCS-QWIP resonance frequencies are temperature dependent, since the refractive index of the PCS depends on temperature (Fig. 4.33a). Unfortunately, in these experiments the laser frequency was fixed and could not be tuned to the exact wavelength of the PCS resonance. The frequency spacing between different DFB-QCLs is too large to precisely hit the PCS-QWIP resonances. To get the correct peak responsivity, a correction factor is calculated from the measured PCS-QWIP spectra for each laser and for each temperature (Fig. 4.33b).

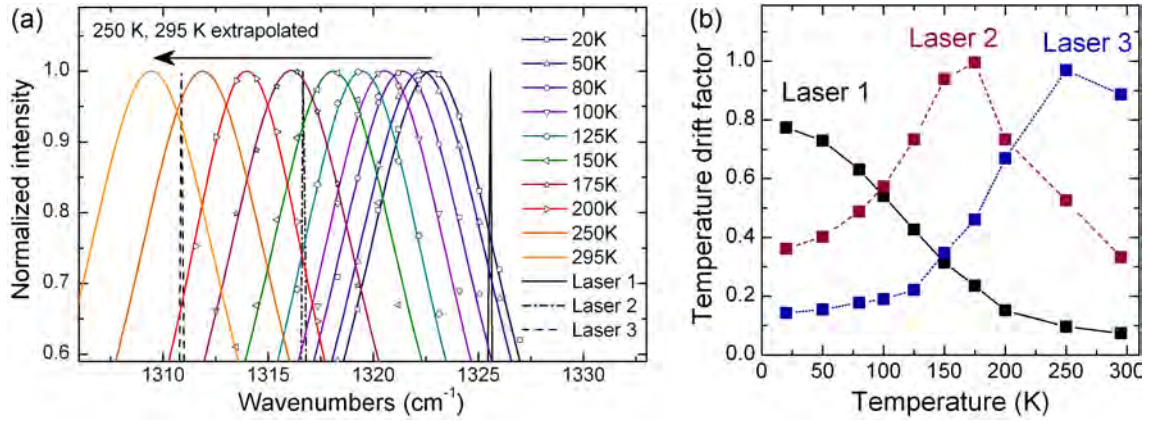


Figure 4.33: Temperature dependent PCS resonance shift. (a) The PCS resonances shift to lower frequencies with increasing temperature. The resonance peaks are Lorentz fitted to extract correction factors. (b) Correction factors for three DFB-QCLs. (Published in [192])

The peak responsivity of the low doped PCS-QWIP H681 with lattice constant  $a = 4.0 \mu\text{m}$  and hole radius  $r/a = 0.22$  is shown in figure 4.34. The responsivity increases with raising temperature, since the extraction probability of the electrons from the quantum wells increases. Only when approaching room temperature, the responsivity decreases again. The reason is probably the low ohmic resistance of the QWIP compared to the input resistance of the transimpedance amplifier, which results in an inefficient photocurrent extraction.

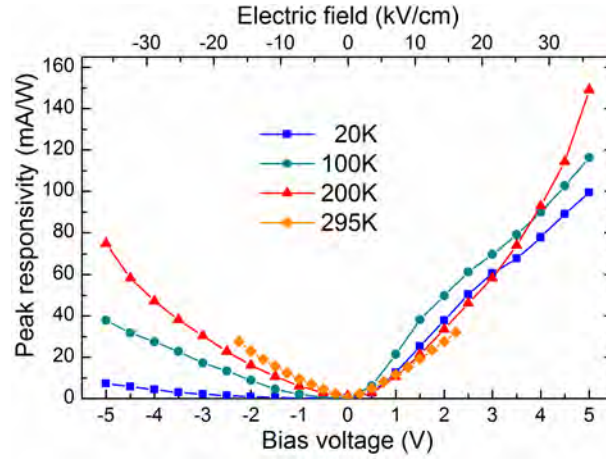


Figure 4.34: Peak responsivity of the low doped PCS-QWIP H681 with lattice constant  $a = 4.0 \mu\text{m}$  and hole radius  $r/a = 0.26$ . (Published in [192])

The peak responsivity of  $150 \text{ mA/W}$  is about five to ten times smaller compared to state-of-the-art QWIPs. However, this design is not optimized yet. With an improved photonic crystal design and MBE growth optimization, a significantly higher responsivity should be achievable.

**Detectivity** To calculate the detectivity of the PCS-QWIPs, the noise spectral density  $\mathcal{S}_n$  is determined. The measurement setup is identical to the standard QWIP setup. At temperatures below  $80 \text{ K}$  the dominant noise source is again the transimpedance amplifier. The noise spectral density of the low doped PCS-QWIP H681 is shown in figure 4.35.

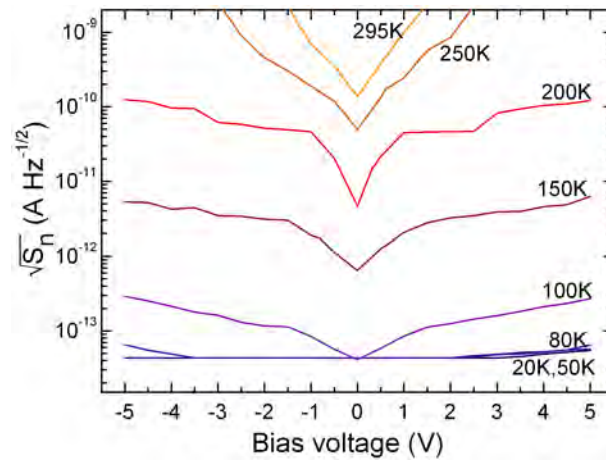


Figure 4.35: Noise spectral density of the low doped PCS-QWIP H681.

To get the specific detectivity  $D^*$ , the noise is normalized by the electrically active area. In a PCS-QWIP the electrically active area should be the mesa area minus the area of the photonic crystal holes. However, we found that the carrier density in the photonic crystal slab is reduced by Fermi level pinning close to the semiconductor surface, which effectively reduces the electrically active detector area. To calculate the detectivity, we estimate an electrically active area of  $100 \times 100 \mu\text{m}$ , which gives a lower boundary for the PCS-QWIP detectivity (Fig. 4.36)<sup>1</sup>. The real PCS-QWIP detectivity is probably higher.

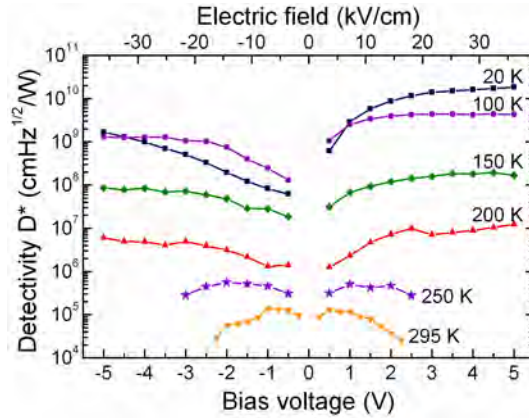


Figure 4.36: Detectivity of the low doped PCS-QWIP H681. The detectivity values were calculated using a conservative estimate for the electrically active area of  $100 \times 100 \mu\text{m}$ . The real electrically active area is probably larger, which would result in even higher detectivity values. (Published in [192])

<sup>1</sup>The size of the mesa is  $148 \times 148 \mu\text{m}$ . The normalized hole radius is  $r/a = 0.26$ , which gives a material filling factor of  $f_{mat} \approx 75\%$  for a hexagonal lattice of air holes. For fabrication reasons it is not possible to etch holes into the entire device area, hence only the center area of the mesa ( $110 \times 110 \mu\text{m}$ ) is structured. The remaining material without holes is equivalent to an area of  $137 \times 137 \mu\text{m}$ . Fermi level pinning reduces the carrier density in the photonic crystal slab, hence the electrically active detector area is significantly smaller. As a conservative estimate for the electrically active area we use  $100 \times 100 \mu\text{m}$ .

## 4.3 Detectivity Enhancement

The detectivity of a photodetector can be enhanced by either increasing the responsivity  $\mathcal{R}$  or by reducing the detector noise spectral density  $\mathcal{S}_n$ . In a PCS-QWIP both effects happen at the same time. To understand and optimize the total enhancement, the two effects are quantified separately.

### 4.3.1 Responsivity Enhancement

The responsivity  $\mathcal{R}$  of the detector is increased by designing the PCS such, that the frequency of the strongest resonance coincides with the QWIP absorption peak frequency (Fig. 4.37). At the PCS resonance frequency the responsivity is increased  $\approx 10$  times compared to the low doped standard QWIP H681. The higher the Q-factor of the resonance peak, the higher is the enhancement. However, with a higher Q-factor also the absorption bandwidth is reduced.

The strongest resonance usually corresponds to the  $0^{\text{th}}$  order TM-like photonic crystal mode. The other photonic crystal resonances are still present, but the peaks are much smaller since they are far away from the QWIP absorption peak. Hence, in a linear scale only one pronounced photocurrent peak is visible.

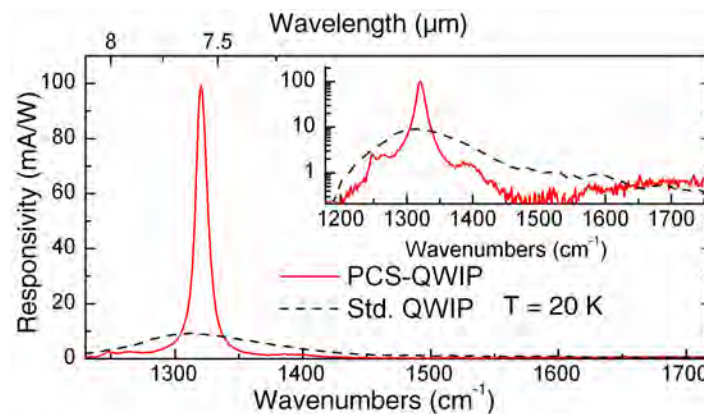


Figure 4.37: Comparison of the low doped PCS-QWIP H681 (solid line) and low doped standard QWIP H681 (dashed line) responsivity. The photonic crystal slab is designed such, that the frequency of the strongest resonance coincides with the QWIP absorption peak frequency. Inset: At a logarithmic scale other photonic crystal resonances are visible. (Published in [117])

**Doping Influence** The responsivity enhancement depends on the Q-factor of the resonance peak, and the Q-factor is limited by the absorption in the PCS (Fig. 4.38a). At high quantum well doping levels, the dominant absorption mechanism is the ISB absorption. A PCS-QWIP fabricated from the high doped QWIP material H661 ( $N_D = 4 \times 10^{11} \text{ cm}^{-2}$ ) shows a moderate responsivity enhancement. The Q-factor of the resonance is  $Q \approx 25$  (Fig. 4.38b). A PCS-QWIP fabricated from the low doped QWIP material H681 ( $N_D = 4 \times 10^9 \text{ cm}^{-2}$ ) shows a significantly larger responsivity enhancement and a Q-factor of  $Q \approx 120$ . The dominating absorption mechanism in the low doped QWIP most likely is not the ISB absorption anymore, but free carrier absorption in the contact layers.

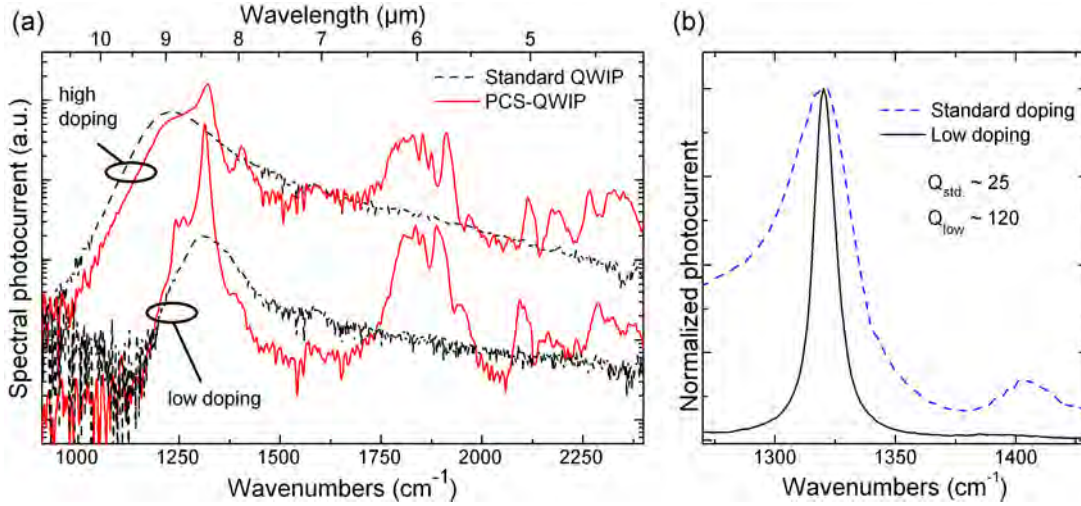


Figure 4.38: Influence of the quantum well doping levels on the responsivity enhancement. At high doping levels ( $N_D = 4 \times 10^{11} \text{ cm}^{-2}$ ), the Q-factor of the photonic crystal resonance is limited by ISB absorption. In a low doped PCS-QWIP ( $N_D = 4 \times 10^9 \text{ cm}^{-2}$ ) the absorption is most likely dominated by free carrier absorption in the contact layers. (Published in [117])

### 4.3.2 Detector Noise Reduction

The dark current of a PCS-QWIP is lower compared to a standard QWIP, because the detector volume is reduced by the photonic crystal etching process by  $\approx 25\%$  (Fig. 4.39a). Additionally, the carrier density in the photonic crystal slab is reduced by Fermi level pinning at the etched surface of the photonic crystal holes [194]. The exposed surface of a PCS-QWIP causes bending of the electronic band structure and depletes the GaAs surface. With a lower number of electrons in the active region the noise

current is also lower. Therefore the noise spectral density  $\mathcal{S}_n$  of the PCS-QWIP is less than half of  $\mathcal{S}_n$  of the standard QWIP (Fig. 4.39b). At 200 K and 4 V bias voltage the dark current suddenly jumps by more than one order of magnitude. This is probably caused by trap ionization, which can occur in heterostructures at high electric fields.

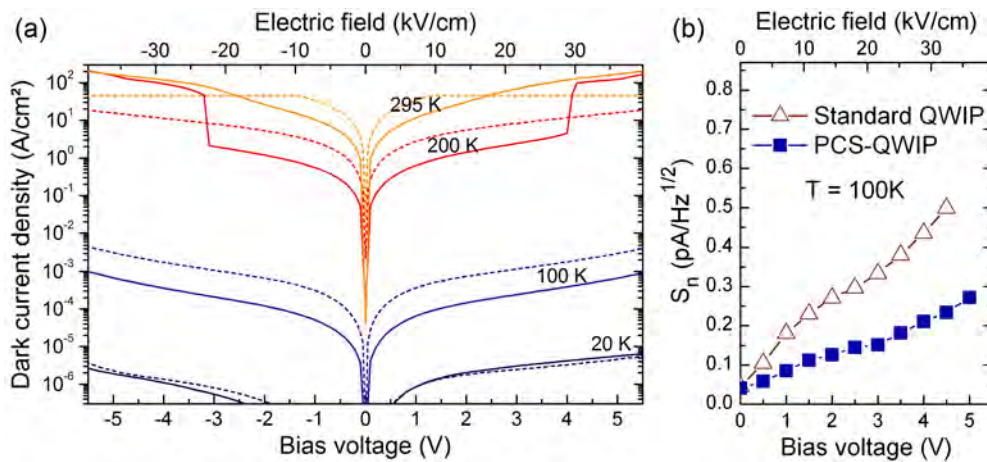


Figure 4.39: Comparison of dark current density and noise spectral density  $\mathcal{S}_n$  of the low doped PCS-QWIP H681 (solid lines) and the low doped standard QWIP H681 (dashed lines).

### 4.3.3 Detectivity Enhancement

The detectivity enhancement is the combined effect of responsivity enhancement and detector noise reduction. To visualize the detectivity enhancement, the PCS-QWIP detectivity is normalized by the standard QWIP detectivity (Fig. 4.40a). The maximum enhancement achieved by the PCS-QWIP design is a 20 times larger specific detectivity  $D^*$ .

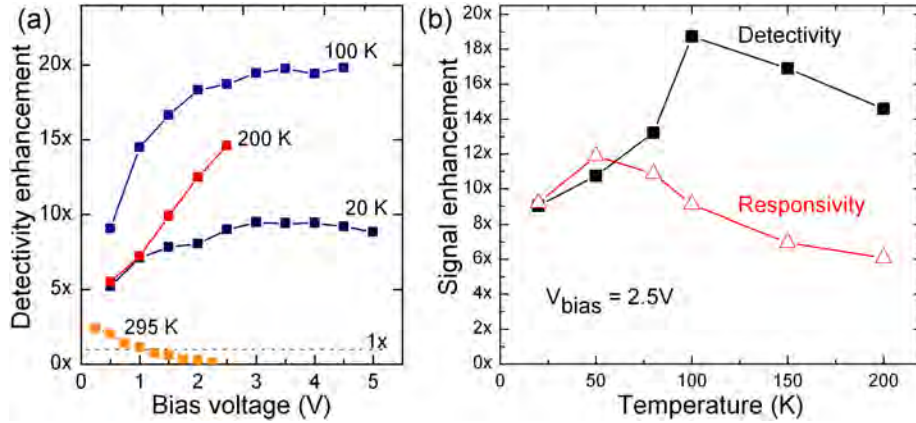


Figure 4.40: Detectivity enhancement. (a) The combined effect of responsivity enhancement and detector noise reduction yields a detectivity enhancement of up to 20 times. (b) Temperature dependence of the responsivity and detectivity enhancement. (Published in [192])

The detectivity enhancement is temperature dependent. For the measured samples (low doped PCS-QWIP H681 and the low doped standard QWIP H681) the maximum is around 100 K (Fig. 4.40b). At temperatures below 70 K the detector noise is dominated by background black body radiation, which is absorbed like signal illumination. Therefore, the detectivity enhancement is equal to the responsivity enhancement. Above 70 K the dark current is dominated by thermal carrier excitation, which is lower in a PCS-QWIP than in a standard QWIP. For this reason the detectivity enhancement becomes larger than the responsivity enhancement.

**Room Temperature Operation** The operation of a photodetector at room temperature is highly desirable, since it reduces complexity and cost. PCS-QWIPs with low quantum well doping allow room temperature operation, since the dark current is reasonable small to prevent a thermal breakdown of the detector. The detectivity is relatively low, but when illuminated with a laser a photocurrent signal can easily be measured. The laser power on the optically active QWIP area of  $110 \times 110 \mu\text{m}^2$  was  $\approx 400 \mu\text{W}$  continuous wave. In figure 4.41 the oscilloscope signal measured from the low doped PCS-QWIP H681 at room temperature is shown. A laser beam is modulated with a chopper at a frequency of  $\approx 80 \text{Hz}$  and focused onto the PCS-QWIP. The modulated signal is clearly visible, which is a direct proof that PCS-QWIPs can be operated at room temperature.

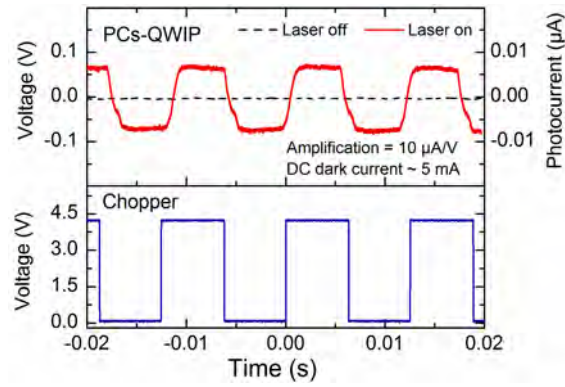


Figure 4.41: Oscilloscope signal of the low doped PCS-QWIP H681 measured at room temperature. The detector was illuminated with a modulated laser beam ( $P_{laser,cw} \approx 400 \mu\text{W}$ ).

## 4.4 Resonance Tuning

Tuning of the absorption peak frequency is a desirable feature for many applications and increases the functionality of a photodetector. Thanks to the unique design of the PCS-QWIP, several ways to tune the photonic crystal resonance are possible.

### 4.4.1 Temperature Tuning

The refractive index of a dielectric material depends on the temperature. This fact can be easily exploited to tune the PCS resonances (Fig. 4.42a). Within a temperature range of  $180\text{ K}$  the resonance peak is shifted over a range of  $9\text{ cm}^{-1}$ . The temperature dependence of the PCS resonances is modeled by using the revised plane wave expansion method (see section 3.3.3). The refractive index change is approximated by  $\Delta n = 4.5 \times 10^{-5} * T[K]$  for GaAs [195]. A tuning coefficient of  $-0.055\text{ cm}^{-1}/K$  was extracted from the simulation, which fits well with the measured resonance peak shifts (Fig. 4.42b). Only at low temperatures, where the approximation for the refractive index change is not valid, the simulation deviates from the measured spectral shift.

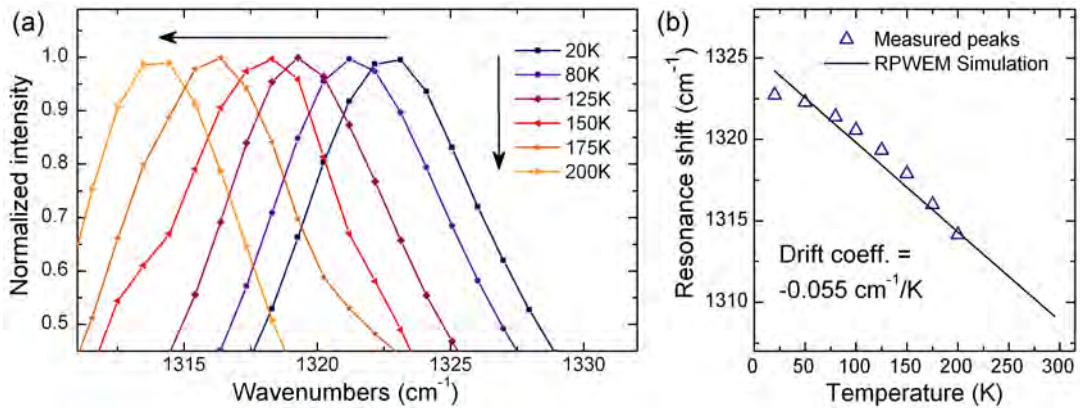


Figure 4.42: Temperature tuning of a PCS-QWIP resonance. (a) With increasing temperature the PCS resonance is tuned towards lower frequencies. (b) The temperature dependence of the PCS resonances is modeled by using the revised plane wave expansion method. (Published in [192])

### 4.4.2 Silicon Nitride Tuning

A straight forward method to tune the photonic crystal resonances is by changing the hole radius. This can be achieved post-fabrication by deposition of silicon nitride

onto the entire photonic crystal QWIP. The photonic crystal resonance was shifted over a bandwidth of  $43\text{ cm}^{-1}$  by deposition of  $690\text{ nm}$   $\text{SiN}_x$  on top of the sample (Fig. 4.43). The  $\text{SiN}_x$  layer thickness inside the photonic crystal holes is thinner, since the deposition rate depends on the orientation of the surface. The tuning coefficient extracted from photocurrent measurements is  $-0.06\text{ cm}^{-1}/\text{nm}$ .

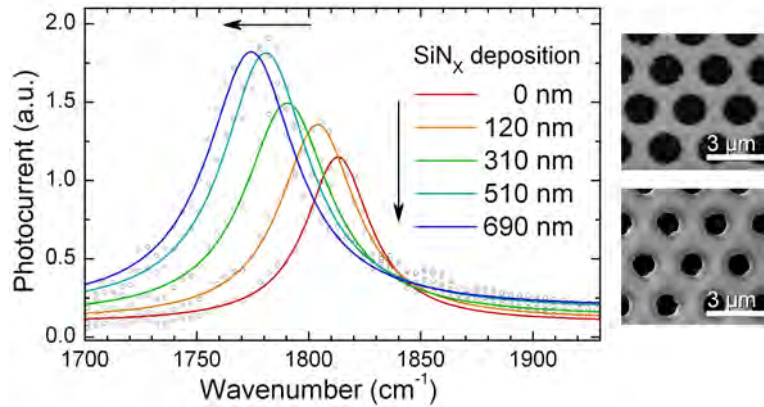


Figure 4.43: Silicon nitride tuning of photonic crystal resonances. (Published in [196])



# 5 Summary and Outlook

## Summary

The focus of this thesis is to improve the performance of quantum well infrared photodetectors using photonic crystal slab resonators. Standard QWIPs provide high detectivities up to  $10^{11} \text{ cm Hz}^{1/2}/\text{W}$  at cryogenic temperatures, are well understood and commercially available. However, the performance decreases rapidly with increasing temperature. Further, standard QWIPs are not sensitive to surface-normal incident light. The strong resonant properties of photonic crystals allow increasing the peak detectivity of QWIPs by resonant absorption enhancement. Further, photonic crystals couple surface-normal incident light to photonic crystal modes, which can be absorbed by the QWIP. Additionally, the photonic crystal resonances can be tuned by several ways, which increases the functionality of QWIP.

We designed and fabricated QWIPs with photonic crystal slab resonators to improve the detectivity and temperature performance. The QWIPs were designed for a peak absorption wavelength  $\lambda = 8 \mu\text{m}$ . Two QWIP designs were grown, which differ only in doping density: H661 with a doping concentration of  $4 \times 10^{11} \text{ cm}^{-2}$  and H681 with a doping concentration of  $4 \times 10^9 \text{ cm}^{-2}$ . To allow fabrication of free standing photonic crystal slabs, a sacrificial layer was introduced below the detector active region. All QWIPs were grown on the in-house MBE.

The PCS design was performed using the revised plane wave expansion method to calculate the photonic band structure. The PCS is approximated as a 2D photonic crystal combined with a simple slab waveguide. The RPWEM simulation tool allows calculation of the photonic band structure of the PCS within a matter of seconds.

PCS-QWIPs, plasmon-enhanced PC-QWIPs and standard mesa QWIPs were fabricated using standard cleanroom technology. The photonic crystal pattern was written by laser direct writing, which allows great flexibility.

The spectral photoresponse of the plasmon-enhanced PC-QWIP shows resonance peaks, which correspond to the photonic crystal modes. However, the peak widths of the photonic crystal resonances are relatively broad and the Q-factors are limited to  $Q \sim 50$ .

The photocurrent spectrum of the PCS-QWIP shows pronounced resonance peaks, which corresponds to dipole-like PCS modes. The simulated photonic band structure

predicts very well the measured photocurrent spectra. PCS-QWIPs were illuminated at surface-normal incidence. As reference the photocurrent response from standard mesa QWIPs was measured.

To increase the peak detectivity of the photodetectors the PCS was designed such, that the frequency of the strongest resonance coincides with the QWIP absorption peak frequency. The absorption peak of the high doped PCS-QWIP H661 shows relatively low Q-factor of  $Q \sim 25$ , since the ISB absorption is too strong. The low-doped PCS-QWIP H681 exhibits much narrower resonances with Q-factors up to  $Q \sim 120$ , resulting in significantly larger absorption enhancement at the resonance frequency.

To accurately measure the detector responsivity, the samples were illuminated with a single-mode mid-IR laser. Specifically for this measurement an array of DFB-QCLs with equally spaced emission frequencies was fabricated, allowing to choose the ideal emission wavelength. The optical laser power was large enough to measure a clear photocurrent signal over a temperature range from 20 K to 300 K. The detector noise spectral density was measured with a Fourier transform spectrum analyzer.

The measurement results show a detectivity enhancement of up to 20 times compared to a standard QWIP. The detectivity enhancement is a combined effect of a responsivity increase and noise current reduction. The device was operated up to room temperature, still showing reasonable detectivities and manageable dark currents.

Two different approaches to tune the photonic crystal resonance were presented: Temperature tuning with a tuning coefficient of  $-0.055 \text{ cm}^{-1}/\text{K}$  and silicon nitride tuning with a tuning coefficient of  $-0.06 \text{ cm}^{-1}/\text{nm}$ .

## Outlook

Photonic crystal QWIPs present a flexible and versatile tool for numerous future research activities.

**Frame-less Photonic Crystal QWIPs** The current PCS-QWIP design includes a large frame to support the free standing photonic crystal membrane. Calculations show, that a large part of the dark current is actually generated in this support frame. An advanced design with small supporting pillars in the corners of the PCS instead of a closed frame should significantly reduce the dark current.

**High Order Mode Suppression** The mode profile of  $0^{\text{th}}$  order and  $1^{\text{st}}$  order slab modes in a PCS is different. While the  $0^{\text{th}}$  order slab mode has a maximum at the center of the slab, the  $1^{\text{st}}$  order modes shows there a minimum. Using a QWIP with

a single quantum well at the center of the slab, it should be possible to distinguish between these modes.

**Photonic Crystal THz QWIPs** QWIPs are not only fabricated for mid-IR frequencies, but also for the THz wavelength range. THz QWIPs are still at an early stage and further research is necessary to achieve reasonable temperature performance. Photonic crystals can help to improve the temperature performance of THz photodetectors.

**Strong Light-Matter Interaction in the Reststrahlenband** If the photonic crystal resonance is designed to be in the Reststrahlenband ( $\lambda \sim 35 \mu\text{m}$ ), light-matter interaction should be enhanced. In such a device the QWIP would only serve as sensing device. The acquired data will help to gain a deeper understanding of the photon-phonon interaction in the Reststrahlenband.

**Electrostatic Tuning** The PCS is usually designed such, that the mode is guided inside the slab. If the slab thickness is reduced, the modes will leak into the surrounding medium and also into the substrate. The distance between PCS and substrate will then influence the propagation properties of the modes, changing also the resonance frequency. An elegant way to change the length of the air gap below the PCS is by applying a bias voltage [185]. The electrostatic force will push the PCS towards the substrate and tune the resonance frequency (Fig. 5.1).

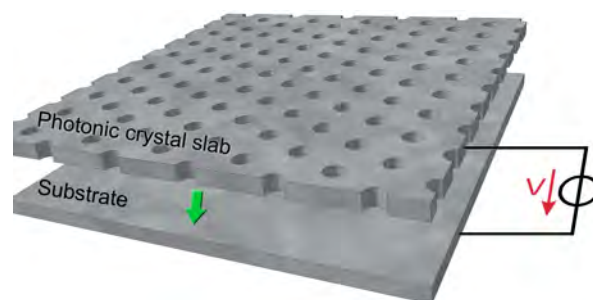


Figure 5.1: Electrostatic tuning of photonic crystal resonances. The applied bias voltage creates an electrostatic force, which will push the PCS towards the substrate and tune the resonance frequency.

The fabrication of a PCS-QWIP, that allows electrostatic tuning is challenging. The PCS membrane needs to be suspended with flexible beams of GaAs. The beams are designed to allow bending with reasonable forces, but need to be stable enough to

support the membrane (Fig. 5.2). The greatest challenge is to grow a heterostructure with low strain, otherwise the PCS membrane will buckle and electrostatic tuning becomes impossible. This project is still subject of ongoing research.

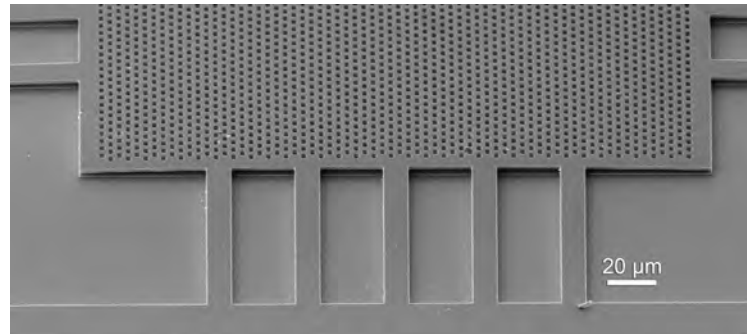


Figure 5.2: SEM image of a PCS-QWIP designed for electrostatic resonance tuning. (Published in [185])

**Plasmonic Lens QWIP** The improvement of responsivity and the reduction of detector noise is probably the main goal in infrared photodetector development. An elegant way to reduce the detector noise is by reduction of the detector volume. The light is collected from a large area and focused onto a tiny detector, which then generates high photocurrents but low noise. Plasmonics offers a fascinating way to focus light on planar semiconductor structures. A tiny QWIP placed at the center of a plasmonic lens should show a significantly improved performance and allow high temperature operation (Fig. 5.3).

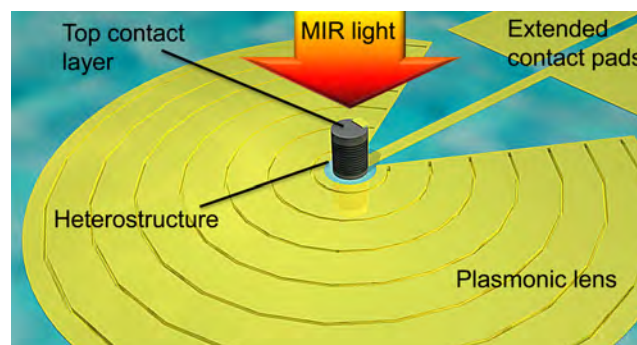


Figure 5.3: Plasmonic lens QWIP. The light is collected from a large area and focused onto a tiny detector.

The absorption peak frequency can be adjusted by the plasmonic grating period  $\Lambda$  (Fig. 5.4). A great challenge for this approach is the huge impedance mismatch between free space and the plasmon waveguide. However, a plasmonic lens QWIP was already fabricated and first promising results were reported [197].

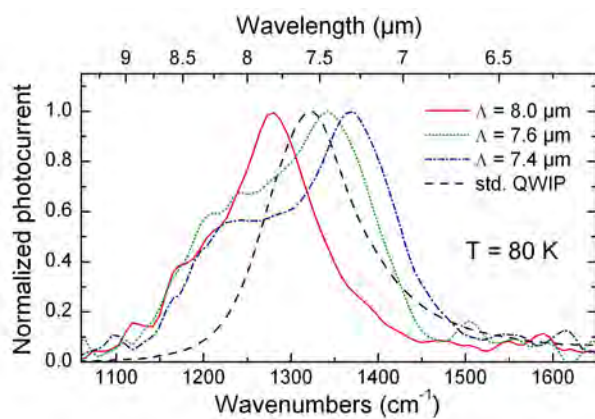


Figure 5.4: The absorption peak frequency depends on the plasmonic grating period  $\Lambda$ .



# Appendix

## Appendix A: QWIP Growth Sheets

Layer	Thickness	Composition	Doping	Description
	nm	% aluminum	n-type	
Substrate	650 $\mu m$		semi-insulating	GaAs Substrate
Si:GaAs	500		$2 \times 10^{18} cm^{-3}$	Contact layer
<i>Loop 40</i>				
AlGaAs	45	30%		Barrier
GaAs	1			Well
Doping			$4 \times 10^{11} cm^{-2}$	Silicon $\delta$ -doping
GaAs	3.5			Well
<i>End Loop</i>				
AlGaAs	45	30%		Barrier
AlGaAs	55	30% $\rightarrow$ 0%		Barrier gradient
Si:GaAs	100		$1 \times 10^{18} cm^{-3}$	Contact layer

Table 5.1: Growth sheet of the QWIP structure H491.

**H540**

Layer	Thickness	Composition	Doping	Description
	nm	% aluminum	n-type	
Substrate	650 $\mu m$		semi-insulating	GaAs Substrate
Si:GaAs	500		$2 \times 10^{18} cm^{-3}$	Contact layer
<i>Loop 40</i>				
AlGaAs	45	30%		Barrier
GaAs	1			Well
Doping			$4 \times 10^{10} cm^{-2}$	Silicon $\delta$ -doping
GaAs	3.5			Well
<i>End Loop</i>				
AlGaAs	45	30%		Barrier
AlGaAs	55	30% $\rightarrow$ 0%		Barrier gradient
Si:GaAs	100		$1 \times 10^{18} cm^{-3}$	Contact layer

Table 5.2: H540: PC-QWIP with low doping.

Pros:

- PC-QWIP with reasonable photocurrent response
- Semi-insulating substrate suitable for backside illumination

Cons:

- Poor vertical mode confinement without plasmon waveguiding

**H661**

Layer	Thickness	Composition	Doping	Description
	nm	% aluminum	n-type	
Substrate	625 $\mu\text{m}$		semi-insulating	GaAs Substrate
GaAs	300		$2 \times 10^{18} \text{ cm}^{-3}$	
AlGaAs	2000	85%		Sacrificial layer
Smoothing	160		$2 \times 10^{18} \text{ cm}^{-3}$	Smoothing superlattice
Si:GaAs	350		$2 \times 10^{18} \text{ cm}^{-3}$	Contact layer
<i>Loop 26</i>				
AlGaAs	45	30%		Barrier
GaAs	1			Well
Doping			$4 \times 10^{11} \text{ cm}^{-3}$	Silicon $\delta$ -doping
GaAs	3.5			Well
<i>End Loop</i>				
AlGaAs	45	30%		Barrier
AlGaAs	11	24%		Barrier gradient
AlGaAs	11	18%		
AlGaAs	11	12%		
AlGaAs	11	6%		
AlGaAs	11	0%		
Si:GaAs	100		$2 \times 10^{18} \text{ cm}^{-3}$	Contact layer
Si:InGaAs	5	50% indium	$2 \times 10^{19} \text{ cm}^{-3}$	Contact layer

Table 5.3: H661: PCS-QWIP with standard doping.

Pros:

- First functioning PCS-QWIP, working horse for several publications
- Strong photoresponse at 8  $\mu\text{m}$  wavelength
- Good vertical mode confinement when fabricated as free standing slab
- Semi-insulating substrate suitable for backside illumination

Cons:

- “Smoothing “ superlattice unstable
- Well doping is too high to allow strong photonic crystal resonances

**H681**

Layer	Thickness	Composition	Doping	Description
	nm	%	n-type	
Substrate	625 $\mu\text{m}$		n+ doping	GaAs Substrate
GaAs	300		$2 \times 10^{18} \text{ cm}^{-3}$	
AlGaAs	2000	85%		Sacrificial layer
Smoothing	160		$2 \times 10^{18} \text{ cm}^{-3}$	Smoothing superlattice
Si:GaAs	350		$2 \times 10^{18} \text{ cm}^{-3}$	Contact layer
<i>Loop 26</i>				
AlGaAs	45	30%		Barrier
GaAs	1			Well
Doping			$4 \times 10^9 \text{ cm}^{-3}$	Silicon $\delta$ -doping
GaAs	3.5			Well
<i>End Loop</i>				
AlGaAs	45	30%		Barrier
AlGaAs	11	24%		Barrier gradient
AlGaAs	11	18%		
AlGaAs	11	12%		
AlGaAs	11	6%		
AlGaAs	11	0%		
Si:GaAs	100		$2 \times 10^{18} \text{ cm}^{-3}$	
Si:InGaAs	5	50% indium	$2 \times 10^{19} \text{ cm}^{-3}$	Contact layer

Table 5.4: H681: PCS-QWIP with low doping.

Pros:

- Low QW doping allows strong photonic crystal resonances. Q-factors up to 300, detectivity enhancement up to 20 times
- Low dark current even at high temperature. Device was operated up to room temperature without saturation of the transimpedance amplifier
- Good vertical mode confinement when fabricated as free standing slab

Cons:

- n+ substrate problematic for backside illumination. Large absorption in the mid-IR
- “Smoothing “ superlattice unstable
- Contact layer doping is probably too high to allow strong photonic crystal resonances

## Appendix B: Processing Challenges

The following images will illustrate some of the processing challenges during PCS-QWIP fabrication.

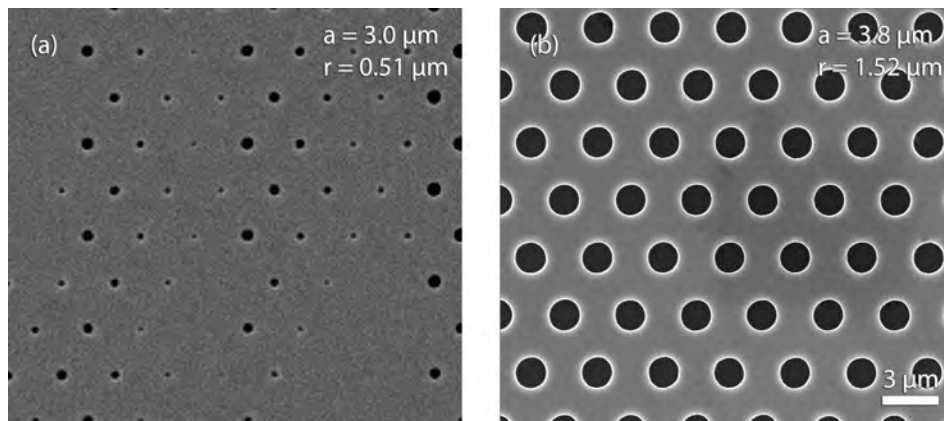


Figure 5.5: The exposure of the laser writer system is not perfectly homogeneous. (a) The inhomogeneous exposure causes partially unexposed photonic crystal holes, which results in an inhomogeneous hole distribution. (b) For large structure ( $> 1 \mu\text{m}$ ) this effect was not visible.

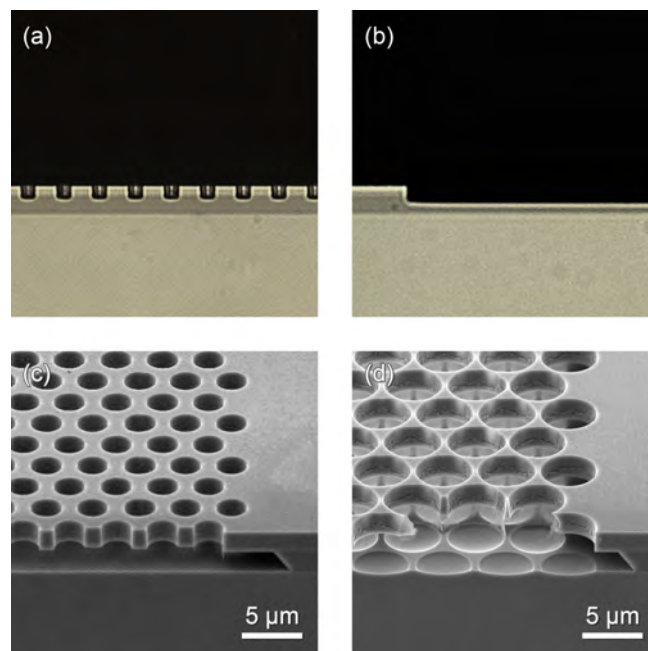


Figure 5.6: Hole size dependent etch depth. The reactive ion etch process depends on the size of the structures. For very different hole sizes on the same sample this causes problems.

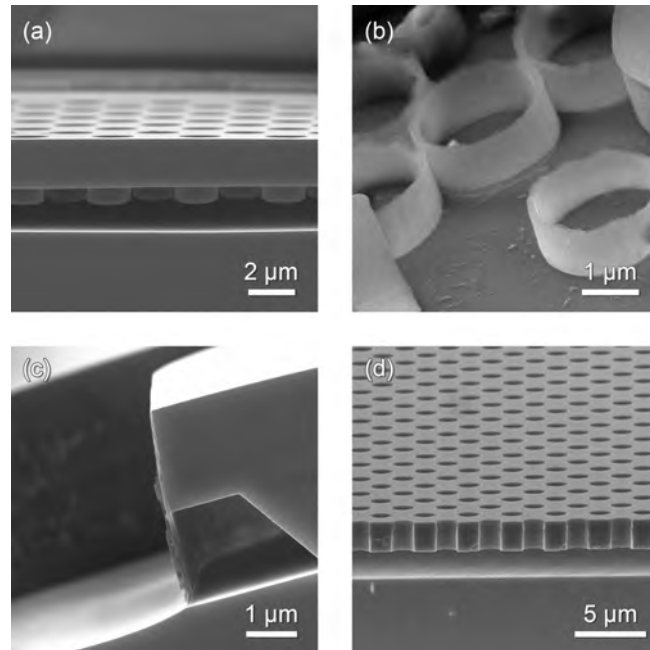


Figure 5.7: Silicon nitride on the sidewalls of the photonic crystal holes. (a) After the insulation process step, the sidewalls of the photonic crystal holes are covered with silicon nitride. (b) The  $SiN_x$  forms small rings on the bottom side of the slab. (c) When the  $SiN_x$  rings reach down to the substrate, the sacrificial layer underetching is inhibited. (d) A high pressure RIE etch step with  $SF_6$  will remove the silicon nitride.

## Appendix C: Substrate Absorption

Standard mesa QWIPs are illuminated at a  $45^\circ$  angle through the substrate. If the substrate is doped, the light will be absorbed by free carrier absorption (Fig. 5.8). This absorption can be calculated using a Drude model.

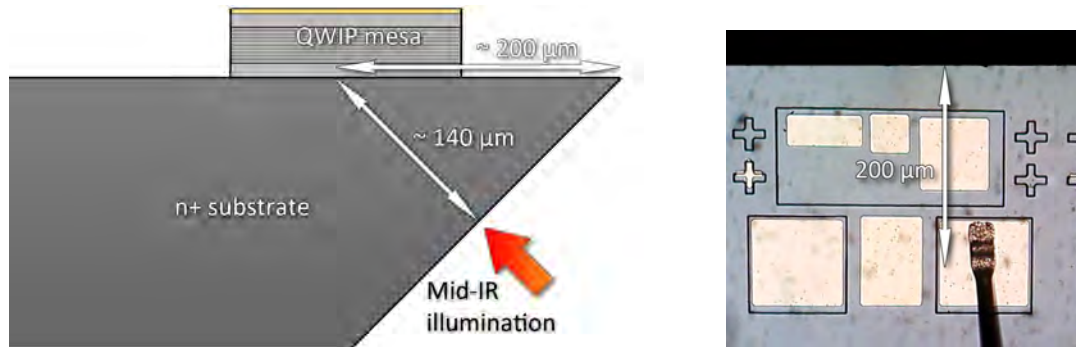


Figure 5.8: Standard mesa QWIPs are illuminated at a  $45^\circ$  angle through the substrate. The absorption length depends on the mesa position on the sample. On the standard QWIP H681, the mesa is placed  $\sim 200 \mu m$  away from the edge.

The doping concentration of the GaAs substrate is  $\sim 1 \times 10^{18} \text{ cm}^{-3}$ . The free carrier absorption in GaAs can be calculated from the imaginary part of the refractive index of the material. With the Drude formula, the refractive index is

$$n = \sqrt{\varepsilon_\infty \left( 1 - \frac{\omega_p^2}{\omega^2 \left( 1 + \frac{i}{\omega\tau} \right)} \right)}$$

where  $\omega = 2\pi c/\lambda$ ,  $\varepsilon_\infty$  is the high frequency dielectric constant,  $\tau = m^*\mu/e_0$  is the scattering time, and  $\omega_p = \sqrt{\frac{n_0 e^2}{\varepsilon_0 \varepsilon_\infty m^*}}$  is the plasma frequency. The absorption coefficient is then given by

$$\alpha = 4\pi\Im(n)/\lambda$$

The mobility is  $\sim 2100 \text{ cm}^2/\text{Vs}$  and the effective electron mass in GaAs is  $m^* = 0.067 m_0$ .

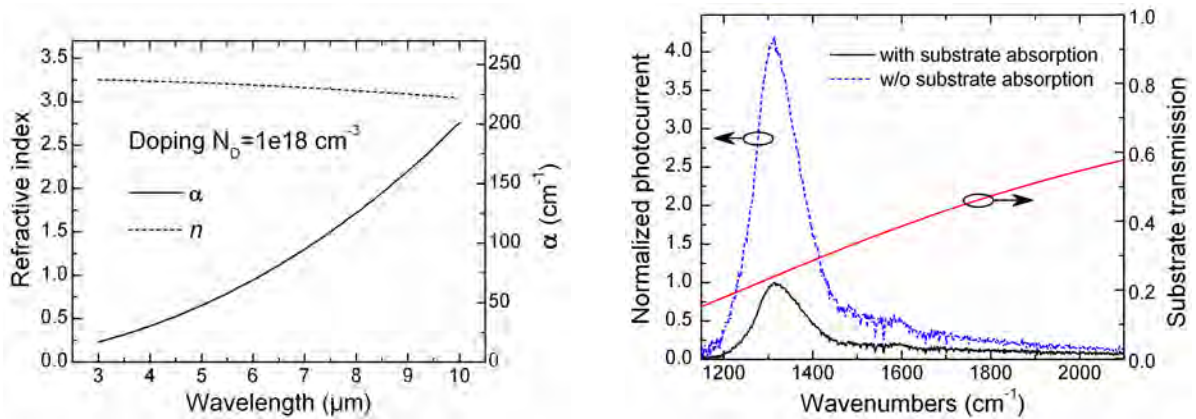


Figure 5.9: Free carrier absorption in doped substrates. (a) Wavelength dependence of the refractive index and the absorption coefficient of doped GaAs. (b) Corrected QWIP photocurrent spectrum. The measured photocurrent spectrum (solid line) is divided by the substrate transmission (red line) to receive the photocurrent spectrum, that would have been measured through a transparent substrate (blue dashed line).

## Appendix D: Laser Beam Profiling

If the QWIP is illuminated with a focused laser beam, the intensity distribution on the detector is inhomogeneous. To calculate the correct optical power on the QWIP, the beam profile needs to be determined.

The stage is moved stepwise to measure a cross section of the beam profile in vertical and horizontal direction (Fig. 5.10).

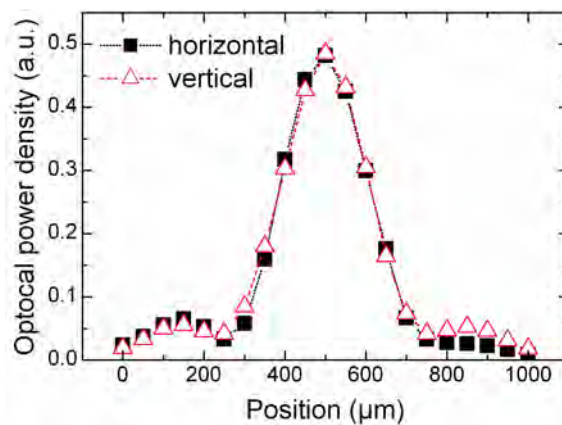


Figure 5.10: Measured cross sections of the beam profile.

Since the QWIP has a finite size, the measured beam profile is broader than the real intensity profile. Using a deconvolution algorithm the real intensity profile is revealed (Fig. 5.11).

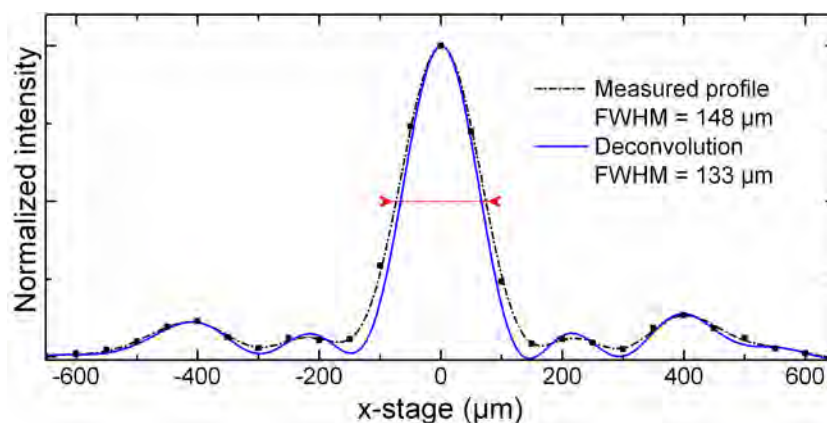


Figure 5.11: Deconvolution of the measured beam profile to reveal the real beam profile.

The two-dimensional intensity profile is interpolated from the two cross sections. Integration over the QWIP area then yields the optical power on the QWIP (Fig. 5.12).

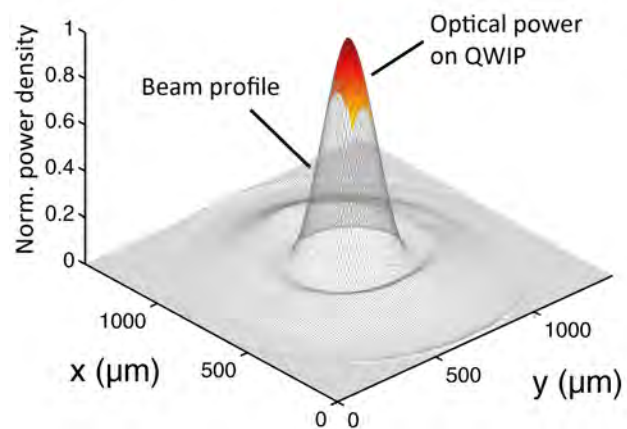


Figure 5.12: Interpolated beam profile of the focused laser beam.

# Bibliography

- [1] W. Herschel, “Experiments on the refrangibility of the invisible rays of the Sun,” *Philosophical Transactions of the Royal Society*, vol. 90, pp. 284–292, 1800.
- [2] P. H. A. Barth, *Biological and biomedical infrared spectroscopy*. Amsterdam Washington, DC: IOS Press, 2009.
- [3] A. Krier, *Mid-Infrared Semiconductor Optoelectronics*. London: Springer, 1 ed., 2006.
- [4] Wikipedia-Community, “Infrared spectroscopy.” [http://en.wikipedia.org/wiki/Infrared\\_spectroscopy](http://en.wikipedia.org/wiki/Infrared_spectroscopy), 2012.
- [5] F. Capasso, R. Paiella, R. Martini, R. Colombelli, C. Gmachl, T. Myers, M. Taubman, R. Williams, C. Bethea, K. Unterrainer, H. Hwang, D. Sivco, A. Cho, A. Sergent, H. Liu, and E. Whittaker, “Quantum cascade lasers: ultrahigh-speed operation, optical wireless communication, narrow linewidth, and far-infrared emission,” *IEEE Journal of Quantum Electronics*, vol. 38, pp. 511–532, 2002.
- [6] R. Martini, R. Paiella, C. Gmachl, F. Capasso, E. Whittaker, H. Liu, H. Hwang, D. Sivco, J. Baillargeon, and A. Cho, “High-speed digital data transmission using mid-infrared quantum cascade lasers,” *Electronics Letters*, vol. 37, no. 21, pp. 1290–1292, 2001.
- [7] R. Martini, C. Bethea, F. Capasso, C. Gmachl, R. Paiella, E. Whittaker, H. Hwang, D. Sivco, J. Baillargeon, and A. Cho, “Free-space optical transmission of multimedia satellite data streams using mid-infrared quantum cascade lasers,” *Electronics Letters*, vol. 38, no. 4, pp. 181–183, 2002.
- [8] S. E. Botts, “Design and performance of a SWIR HgCdTe hybrid module for multispectral linear array/Landsat applications,” *IEEE Transactions on Electron Devices*, vol. ED-32, pp. 1584–1591, 1985.
- [9] A. Rogalski, “Infrared detectors: an overview,” *Infrared Physics & Technology*, vol. 43, pp. 187–210, 2002.
- [10] A. Rogalski, “Infrared detectors: status and trends,” *Progress in Quantum Electronics*, vol. 27, pp. 59–210, 2003.
- [11] A. Rogalski, “Recent progress in infrared detector technologies,” *Infrared Physics & Technology*, vol. 54, no. 3, pp. 136–154, 2011. Proceedings of the International Conference on Quantum Structure Infrared Photodetector (QSIP) 2010.

- [12] R. Dornhaus, G. Nimtz, B. Schlicht, G. Nimtz, and B. Schlicht, "Narrow-gap lead salts," in *Narrow-Gap Semiconductors*, vol. 98 of *Springer Tracts in Modern Physics*, pp. 1–117, Springer Berlin / Heidelberg, 1983.
- [13] M. Tacke, "New developments and applications of tunable IR lead salt lasers," *Infrared Physics & Technology*, vol. 36, no. 1, pp. 447 – 463, 1995. Proceedings of the Sixth International Conference on Infrared Physics.
- [14] H. Günzler and H.-U. Gremlich, *IR spectroscopy : an introduction*. Weinheim: Wiley-VCH, 2002.
- [15] P. Norton, "HgCdTe infrared detectors," *Optoelectronics review*, vol. 10, pp. 159–174, 2002.
- [16] A. Rogalski, "HgCdTe infrared detector material: history, status and outlook," *Reports on Progress in Physics*, vol. 68, p. 2267, 2005.
- [17] W. W. Chow and S. W. Koch, *Semiconductor-laser fundamentals: physics of the gain materials*. Berlin New York: Springer Berlin Heidelberg, 1999.
- [18] A. Cho and J. Arthur, "Molecular beam epitaxy," *Progress in Solid State Chemistry*, vol. 10, Part 3, no. 0, pp. 157 – 191, 1975.
- [19] G. Sun, *Advances in Lasers and Electro Optics*. InTech, 2010.
- [20] R. F. Kazarinov and R. A. Suris, "Possibility of amplification of electromagnetic waves in a semiconductor with a superlattice," *Soviet physics: Semiconductors*, vol. 5, pp. 797–800, 1971.
- [21] R. F. Kazarinov and R. A. Suris, "Electric and electromagnetic properties of semiconductors with a superlattice," *Soviet physics: Semiconductors*, vol. 6, pp. 120–131, 1972.
- [22] L. L. Chang, L. Esaki, and R. Tsu, "Resonant tunneling in semiconductor double barriers," *Applied Physics Letters*, vol. 24, no. 12, pp. 593–595, 1974.
- [23] L. L. Chang, L. Esaki, and G. A. Sai-Halasz, "Infrared Optical Devices of Layered Structures," *IBM Technical Disclosure Bulletin*, vol. 20, no. 5, p. 2019, 1977.
- [24] L. C. West and S. J. Eglash, "First observation of an extremely large-dipole infrared transition within the conduction band of a GaAs quantum well," *Applied Physics Letters*, vol. 46, no. 12, pp. 1156–1158, 1985.
- [25] B. F. Levine, K. K. Choi, C. G. Bethea, J. Walker, and R. J. Malik, "New 10  $\mu\text{m}$  infrared detector using intersubband absorption in resonant tunneling GaAlAs superlattices," *Applied Physics Letters*, vol. 50, no. 16, pp. 1092–1094, 1987.
- [26] M. Helm, P. England, E. Colas, F. DeRosa, and S. J. A. Jr., "Intersubband emission from semiconductor superlattices excited by sequential resonant tunneling," *Physical Review Letters*, vol. 63, p. 74, 1989.

- [27] J. Faist, F. Capasso, D. L. Sivco, C. Sirtori, A. L. Hutchinson, and A. Y. Cho, "Quantum cascade laser," *Science*, vol. 264, pp. 553–556, 1994.
- [28] B. Gokden, Y. Bai, N. Bandyopadhyay, S. Slivken, and M. Razeghi, "Broad area photonic crystal distributed feedback quantum cascade lasers emitting 34W at  $\lambda \sim 4.36\mu\text{m}$ ," *Applied Physics Letters*, vol. 97, no. 13, p. 131112, 2010.
- [29] E. Mujagić, M. Nobile, H. Detz, W. Schrenk, J. Chen, C. Gmachl, and G. Strasser, "Ring cavity induced threshold reduction in single-mode surface emitting quantum cascade lasers," *Applied Physics Letters*, vol. 96, no. 3, p. 031111, 2010.
- [30] J. Zhang, L. Wang, J. Chen, L. Zhao, F. Liu, J. Liu, L. Li, and Z. Wang, "Continuous-wave operation of distributed-feedback quantum cascade laser with ultra-low threshold current density," *Electronics Letters*, vol. 47, no. 24, pp. 1338–1339, 2011.
- [31] A. Wittmann, A. Hugi, E. Gini, N. Hoyler, and J. Faist, "Heterogeneous High-Performance Quantum-Cascade Laser Sources for Broad-Band Tuning," *IEEE Journal of Quantum Electronics*, vol. 44, no. 11, pp. 1083–1088, 2008.
- [32] E. Mujagić, C. Schwarzer, Y. Yao, J. Chen, C. Gmachl, and G. Strasser, "Two-dimensional broadband distributed-feedback quantum cascade laser arrays," *Applied Physics Letters*, vol. 98, no. 14, p. 141101, 2011.
- [33] E. Mujagić, L. K. Hoffmann, S. Schartner, M. Nobile, W. Schrenk, M. P. Semtsiv, M. Wienold, W. T. Masselink, and G. Strasser, "Low divergence single-mode surface emitting quantum cascade ring lasers," *Applied Physics Letters*, vol. 93, no. 16, p. 161101, 2008.
- [34] E. Mujagić, S. Schartner, L. K. Hoffmann, W. Schrenk, M. P. Semtsiv, M. Wienold, W. T. Masselink, and G. Strasser, "Grating-coupled surface emitting quantum cascade ring lasers," *Applied Physics Letters*, vol. 93, no. 1, p. 011108, 2008.
- [35] S. I. Ahn, E. Mujagić, M. Nobile, H. Detz, S. Kalchmair, A. M. Andrews, P. Klang, W. Schrenk, and G. Strasser, "Electrical beam steering of Y-coupled quantum cascade lasers," *Applied Physics Letters*, vol. 96, no. 14, p. 141113, 2010.
- [36] W. Bewley, J. Lindle, C. S. Kim, I. Vurgaftman, J. Meyer, A. Evans, J. S. Yu, S. Slivken, and M. Razeghi, "Beam steering in high-power CW quantum-cascade lasers," *IEEE Journal of Quantum Electronics*, vol. 41, pp. 833–841, 2005.
- [37] H. C. Liu and F. Capasso, *Intersubband transitions in quantum wells: Physics and device applications I*. San Diego, CA: Academic Press, 2000.
- [38] C. Hamaguchi, *Basic semiconductor physics*. Berlin: Springer-Verlag, 2010.
- [39] D. Hofstetter, J. Faist, M. Beck, and U. Oesterle, "Surface-emitting  $10.1\mu\text{m}$

- quantum-cascade distributed feedback lasers,” *Applied Physics Letters*, vol. 75, no. 24, pp. 3769–3771, 1999.
- [40] J. Y. Andersson and L. Lundqvist, “Grating-coupled quantum-well infrared detectors: theory and performance,” *Journal of Applied Physics*, vol. 71, pp. 3600–3610, 1992.
- [41] J. Y. Andersson, L. Lundqvist, and Z. F. Paska, “Quantum efficiency enhancement of AlGaAs/GaAs quantum well infrared detectors using a waveguide with a grating coupler,” *Applied Physics Letters*, vol. 58, no. 20, pp. 2264–2266, 1991.
- [42] Y. Fu, M. Willander, W. Lu, and W. Xu, “Optical coupling in quantum well infrared photodetector by diffraction grating,” *Journal of Applied Physics*, vol. 84, no. 10, pp. 5750–5755, 1998.
- [43] G. Sarusi, B. F. Levine, S. J. Pearton, K. M. S. Bandara, and R. E. Leibenguth, “Improved performance of quantum well infrared photodetectors using random scattering optical coupling,” *Applied Physics Letters*, vol. 64, no. 8, pp. 960–962, 1994.
- [44] H. Schneider and H. C. Liu, *Quantum well infrared photodetectors : physics and applications*. Berlin New York: Springer, 2007.
- [45] A. Rogalski, “Comparison of the performance of quantum well and conventional bulk infrared photodetectors,” *Infrared Physics & Technology*, vol. 38, pp. 295–310, 1997.
- [46] S. Gunapala, S. Bandara, J. Liu, E. Luong, S. Rafol, J. Mumolo, D. Ting, J. Bock, M. Ressler, M. Werner, P. LeVan, R. Chehayeb, C. Kukkonen, M. Levy, P. LeVan, and M. Fauci, “Quantum well infrared photodetector research and development at Jet Propulsion Laboratory,” *Infrared Physics & Technology*, vol. 42, pp. 267–282, 2001.
- [47] D. Pan, E. Towe, and S. Kennerly, “Normal-incidence intersubband (In, Ga)As/GaAs quantum dot infrared photodetectors,” *Applied Physics Letters*, vol. 73, no. 14, pp. 1937–1939, 1998.
- [48] J. Jiang, S. Tsao, T. O’Sullivan, W. Zhang, H. Lim, T. Sills, K. Mi, M. Razeghi, G. J. Brown, and M. Z. Tidrow, “High detectivity InGaAs/InGaP quantum-dot infrared photodetectors grown by low pressure metalorganic chemical vapor deposition,” *Applied Physics Letters*, vol. 84, no. 12, pp. 2166–2168, 2004.
- [49] H. C. Liu, M. Gao, J. McCaffrey, Z. R. Wasilewski, and S. Fafard, “Quantum dot infrared photodetectors,” *Applied Physics Letters*, vol. 78, no. 1, pp. 79–81, 2001.
- [50] S. Krishna, “Quantum dots-in-a-well infrared photodetectors,” *Infrared Physics & Technology*, vol. 47, pp. 153–163, 2005. Proceedings of the International Workshop on Quantum Well Infrared Photodetectors.

- [51] R. V. Shenoi, R. S. Attaluri, A. Siroya, J. Shao, Y. D. Sharma, A. Stintz, T. E. Vandervelde, and S. Krishna, “Low-strain InAs/InGaAs/GaAs quantum dots-in-a-well infrared photodetector,” in *Journal of Vacuum Science & Technology B*, vol. 26, pp. 1136–1139, AVS, 2008. Papers from the 25th north american conference on molecular beam epitaxy.
- [52] H. Lim, S. Tsao, W. Zhang, and M. Razeghi, “High-performance InAs quantum-dot infrared photodetectors grown on InP substrate operating at room temperature,” *Applied Physics Letters*, vol. 90, no. 13, p. 131112, 2007.
- [53] P. Vines, C. Tan, J. David, R. Attaluri, T. Vandervelde, and S. Krishna, “Noise, Gain, and Responsivity in Low-Strain Quantum Dot Infrared Photodetectors With up to 80 Dot-in-a-Well Periods,” *IEEE Journal of Quantum Electronics*, vol. 47, no. 5, pp. 607–613, 2011.
- [54] S. J. Lee, Z. Ku, A. Barve, J. Montoya, W.-Y. Jang, S. R. J. Brueck, M. Sundaram, A. Reisinger, S. Krishna, and S. K. Noh, “A monolithically integrated plasmonic infrared quantum dot camera,” *Nature communications*, vol. 2, p. 286, 2011.
- [55] A. V. Barve, J. Montaya, Y. Sharma, T. Rotter, J. Shao, W.-Y. Jang, S. Meesala, S. J. Lee, and S. Krishna, “High temperature operation of quantum dots-in-a-well infrared photodetectors,” *Infrared Physics & Technology*, vol. 54, no. 3, pp. 215 – 219, 2011. Proceedings of the International Conference on Quantum Structure Infrared Photodetector (QSIP) 2010.
- [56] H. Schneider, “Optimized performance of quantum well intersubband infrared detectors: Photovoltaic versus photoconductive operation,” *Journal of Applied Physics*, vol. 74, no. 7, pp. 4789–4791, 1993.
- [57] H. Schneider, C. Schönbein, M. Walther, K. Schwarz, J. Fleissner, and P. Koidl, “Photovoltaic quantum well infrared photodetectors: The four-zone scheme,” *Applied Physics Letters*, vol. 71, no. 2, pp. 246–248, 1997.
- [58] L. Gendron, M. Carras, A. Huynh, V. Ortiz, C. Koeniguer, and V. Berger, “Quantum cascade photodetector,” *Applied Physics Letters*, vol. 85, no. 14, pp. 2824–2826, 2004.
- [59] S. Hinds, M. Buchanan, R. Dudek, S. Haffouz, S. Laframboise, Z. Wasilewski, and H. C. Liu, “Near-Room-Temperature Mid-Infrared Quantum Well Photodetector,” *Advanced Materials*, vol. 23, no. 46, pp. 5536–5539, 2011.
- [60] B. F. Levine, “Quantum-well infrared photodetectors,” *Journal of Applied Physics*, vol. 74, no. 8, pp. R1–R81, 1993.
- [61] S. Gunapala and S. Bandara, “Chapter 4 Quantum Well Infrared Photodetector (QWIP) Focal Plane Arrays,” in *Semiconductors and Semimetals* (H. Liu and

- F. Capasso, eds.), vol. 62 of *Semiconductors and Semimetals*, pp. 197 – 282, Elsevier, 1999.
- [62] S. Krishna, S. Gunapala, S. Bandara, C. Hill, and D. Ting, “Quantum Dot Based Infrared Focal Plane Arrays,” *Proceedings of the IEEE*, vol. 95, no. 9, pp. 1838–1852, 2007.
- [63] S. Krishna, D. Forman, S. Annamalai, P. Dowd, P. Varangis, T. Tumolillo, Jr, A. Gray, J. Zilko, K. Sun, M. Liu, J. Campbell, and D. Carothers, “Demonstration of a 320 x 256 two-color focal plane array using InAs/InGaAs quantum dots in well detectors,” *Applied Physics Letters*, vol. 86, no. 19, p. 193501, 2005.
- [64] S. Gunapala, S. Bandara, J. Liu, J. Mumolo, C. Hill, S. Rafol, D. Salazar, J. Woolaway, P. LeVan, and M. Tidrow, “Towards dualband megapixel QWIP focal plane arrays,” *Infrared Physics & Technology*, vol. 50, pp. 217–226, 2007. Fourth International Workshop on Quantum Well Infrared Photodetectors.
- [65] A. Rogalski, J. Antoszewski, and L. Faraone, “Third-generation infrared photodetector arrays,” *Journal of Applied Physics*, vol. 105, no. 9, pp. 091101–1 – 091101–44, 2009.
- [66] S. U. Eker, Y. Arslan, A. E. Onuk, and C. Besikci, “High Conversion Efficiency InP/InGaAs Strained Quantum Well Infrared Photodetector Focal Plane Array With 9.7  $\mu\text{m}$  Cut-Off for High-Speed Thermal Imaging,” *IEEE Journal of Quantum Electronics*, vol. 46, pp. 164–168, 2010.
- [67] S. Krishna, “The infrared retina,” *Journal of Physics D: Applied Physics*, vol. 42, no. 23, p. 234005, 2009.
- [68] H. Schneider, H. C. Liu, S. Winnerl, O. Drachenko, M. Helm, and J. Faist, “Room-temperature midinfrared two-photon photodetector,” *Applied Physics Letters*, vol. 93, no. 10, p. 101114, 2008.
- [69] F. Castellano, R. C. Iotti, and F. Rossi, “Feasibility of sequential multiphoton absorption for terahertz radiation detection,” *physica status solidi (c)*, vol. 5, no. 1, pp. 273–276, 2008.
- [70] H. C. Liu, C. Y. Song, A. J. SpringThorpe, and J. C. Cao, “Terahertz quantum-well photodetector,” *Applied Physics Letters*, vol. 84, no. 20, pp. 4068–4070, 2004.
- [71] H. Liu, H. Luo, C. ying Song, Z. Wasilewski, A. SpringThorpe, and J. Cao, “Terahertz Quantum Well Photodetectors,” *IEEE Journal of Selected Topics in Quantum Electronics*, vol. 14, no. 2, pp. 374–377, 2008.
- [72] H. Schneider, H. C. Liu, S. Winnerl, C. Y. Song, M. Walther, and M. Helm, “Terahertz two-photon quantum well infrared photodetector,” *Optics Express*, vol. 17, no. 15, pp. 12279–12284, 2009.
- [73] R. H. Ritchie, “Plasma Losses by Fast Electrons in Thin Films,” *Physical Review*, vol. 106, pp. 874–881, 1957.

- [74] J. B. Pendry, L. Martín-Moreno, and F. J. Garcia-Vidal, “Mimicking surface plasmons with structured surfaces,” *Science*, vol. 305, no. 5685, pp. 847–848, 2004.
- [75] R. V. Shenoi, D. A. Ramirez, Y. Sharma, R. S. Attaluri, J. Rosenberg, O. J. Painter, and S. Krishna, “Plasmon assisted photonic crystal quantum dot sensors,” in *Nanophotonics and Macrophotonics for Space Environments* (E. W. Taylor and D. A. Cardimona, eds.), vol. 6713, p. 67130P, SPIE, 2007.
- [76] J. Rosenberg, R. V. Shenoi, T. E. Vandervelde, S. Krishna, and O. Painter, “A multispectral and polarization-selective surface-plasmon resonant midinfrared detector,” *Applied Physics Letters*, vol. 95, no. 16, p. 161101, 2009.
- [77] X. Hu, M. Li, Z. Ye, W. Y. Leung, K.-M. Ho, and S.-Y. Lin, “Design of midinfrared photodetectors enhanced by resonant cavities with subwavelength metallic gratings,” *Applied Physics Letters*, vol. 93, no. 24, p. 241108, 2008.
- [78] W. Wu, A. Bonakdar, and H. Mohseni, “Plasmonic enhanced quantum well infrared photodetector with high detectivity,” *Applied Physics Letters*, vol. 96, no. 16, p. 161107, 2010.
- [79] C.-C. Chang, Y. D. Sharma, Y.-S. Kim, J. A. Bur, R. V. Shenoi, S. Krishna, D. Huang, and S.-Y. Lin, “A Surface Plasmon Enhanced Infrared Photodetector Based on InAs Quantum Dots,” *Nano Letters*, vol. 10, no. 5, pp. 1704–1709, 2010.
- [80] K. Kishino, M. Unlu, J.-I. Chyi, J. Reed, L. Arsenault, and H. Morkoc, “Resonant cavity-enhanced (RCE) photodetectors,” *IEEE Journal of Quantum Electronics*, vol. 27, no. 8, pp. 2025–2034, 1991.
- [81] M. S. Unlu and S. Strite, “Resonant cavity enhanced photonic devices,” *Journal of Applied Physics*, vol. 78, no. 2, pp. 607–639, 1995.
- [82] H. S. Nalwa, *Photodetectors and fiber optics*. San Diego, CA London: Academic Press, 2001.
- [83] H.-H. Tung and C.-P. Lee, “Design of a resonant-cavity-enhanced photodetector for high-speed applications,” *IEEE Journal of Quantum Electronics*, vol. 33, no. 5, pp. 753–760, 1997.
- [84] H. Huang, Y. Huang, X. Wang, Q. Wang, and X. Ren, “Long wavelength resonant cavity photodetector based on InP/air-gap Bragg reflectors,” *IEEE Photonics Technology Letters*, vol. 16, no. 1, pp. 245–247, 2004.
- [85] S. Gryshchenko, A. Dyomin, and V. Lysak, “Theoretical study of the quantum efficiency of InGaAs/GaAs resonant cavity enhanced photodetectors,” in *International Workshop on Optoelectronic Physics and Technology*, pp. 20–22, 2007.
- [86] T. Asano, C. Hu, Y. Zhang, M. Liu, J. C. Campbell, and A. Madhukar, “Design Consideration and Demonstration of Resonant-Cavity-Enhanced Quantum Dot

- Infrared Photodetectors in Mid-Infrared Wavelength Regime ( $3 - 5 \mu m$ ),” *IEEE Journal of Quantum Electronics*, vol. 46, pp. 1484–1491, 2010.
- [87] S. M. Sze, *Physics of Semiconductor Devices*. New York: Wiley, 1981.
- [88] J. D. Joannopoulos, S. G. Johnson, and J. Winn, *Photonic Crystals, Molding the Flow of Light*. Princeton University Press, 1st ed., 1995.
- [89] J. Joannopoulos, P. R. Villeneuve, and S. Fan, “Photonic crystals,” *Solid State Communications*, vol. 102, pp. 165–173, 1997. Highlights in Condensed Matter Physics and Materials Science.
- [90] J.-M. Lourtioz, H. Benisty, V. Berger, J.-M. Gerard, D. Maystre, A. Tchelnokov, and D. Pagnoux, *Photonic Crystals : Towards Nanoscale Photonic Devices*. Berlin New York: Springer, 2005.
- [91] D. W. Prather, S. Shi, A. Sharkawy, J. Murakowski, and G. J. Schneider, *Photonic Crystals: Theory, Applications, and Fabrication*. Wiley, 2009.
- [92] V. Bykov, “Spontaneous Emission in a Periodic Structure,” *Soviet Journal of Experimental and Theoretical Physics*, vol. 35, no. 7, p. 269, 1972.
- [93] V. Bykov, “Spontaneous Emission from a Medium with a Band Spectrum,” *Soviet Journal of Quantum Electronics*, vol. 4, no. 7, p. 861, 1975.
- [94] E. Yablonovitch, “Inhibited Spontaneous Emission in Solid-State Physics and Electronics,” *Physical Review Letters*, vol. 58, pp. 2059–2062, 1987.
- [95] S. John, “Strong localization of photons in certain disordered dielectric superlattices,” *Physical Review Letters*, vol. 58, pp. 2486–2489, 1987.
- [96] E. N. Economou and A. Zdzetsis, “Classical wave propagation in periodic structures,” *Physical Review B*, vol. 40, pp. 1334–1337, 1989.
- [97] Z. Zhang and S. Satpathy, “Electromagnetic wave propagation in periodic structures: Bloch wave solution of Maxwell’s equations,” *Physical Review Letters*, vol. 65, pp. 2650–2653, 1990.
- [98] K. M. Leung and Y. F. Liu, “Photon band structures: The plane-wave method,” *Physical Review B*, vol. 41, pp. 10188–10190, 1990.
- [99] M. Plihal and A. A. Maradudin, “Photonic band structure of two-dimensional systems: The triangular lattice,” *Physical Review B*, vol. 44, pp. 8565–8571, 1991.
- [100] V. Zabelin, *Numerical Investigations of Two-Dimensional Photonic Crystal Optical Properties, Design and Analysis of Photonic Crystal Based Structures*. PhD thesis, École Polytechnique Fédérale de Lausanne, 2009.
- [101] E. Yablonovitch and T. J. Gmitter, “Photonic band structure: The face-centered-cubic case,” *Physical Review Letters*, vol. 63, pp. 1950–1953, 1989.
- [102] E. Yablonovitch, T. J. Gmitter, and K. M. Leung, “Photonic band structure:

- The face-centered-cubic case employing nonspherical atoms,” *Physical Review Letters*, vol. 67, pp. 2295–2298, 1991.
- [103] E. Özbay, E. Michel, G. Tuttle, R. Biswas, K. M. Ho, J. Bostak, and D. M. Bloom, “Terahertz spectroscopy of three-dimensional photonic band-gap crystals,” *Optics Letters*, vol. 19, no. 15, pp. 1155–1157, 1994.
- [104] S.-Y. Lin and J. Fleming, “A three-dimensional optical photonic crystal,” *Journal of Lightwave Technology*, vol. 17, no. 11, pp. 1944–1947, 1999.
- [105] I. I. Tarhan and G. H. Watson, “Photonic Band Structure of fcc Colloidal Crystals,” *Physical Review Letters*, vol. 76, pp. 315–318, 1996.
- [106] R. D. Pradhan, J. A. Bloodgood, and G. H. Watson, “Photonic band structure of bcc colloidal crystals,” *Physical Review B*, vol. 55, pp. 9503–9507, 1997.
- [107] J. D. Joannopoulos, P. R. Villeneuve, and S. Fan, “Photonic Crystals: Putting a new Twist on Light,” *Nature*, vol. 386, pp. 143–149, 1997.
- [108] J. N. Winn, R. D. Meade, and J. Joannopoulos, “Two-dimensional Photonic Band-gap Materials,” *Journal of Modern Optics*, vol. 41, no. 2, pp. 257–273, 1994.
- [109] R. D. Meade, A. Devenyi, J. D. Joannopoulos, O. L. Alerhand, D. A. Smith, and K. Kash, “Novel applications of photonic band gap materials: Low-loss bends and high Q cavities,” *Journal of Applied Physics*, vol. 75, no. 9, pp. 4753–4755, 1994.
- [110] S. Fan, J. D. Joannopoulos, J. N. Winn, A. Devenyi, J. C. Chen, and R. D. Meade, “Guided and defect modes in periodic dielectric waveguides,” *Journal of the Optical Society of America B: Optical Physics*, vol. 12, no. 7, pp. 1267–1272, 1995.
- [111] A. Mekis, J. C. Chen, I. Kurland, S. Fan, P. R. Villeneuve, and J. D. Joannopoulos, “High Transmission through Sharp Bends in Photonic Crystal Waveguides,” *Physical Review Letters*, vol. 77, pp. 3787–3790, 1996.
- [112] S.-Y. Lin, E. Chow, V. Hietala, P. R. Villeneuve, and J. D. Joannopoulos, “Experimental Demonstration of Guiding and Bending of Electromagnetic Waves in a Photonic Crystal,” *Science*, vol. 282, p. 274, 1998.
- [113] F. Cuesta-Soto, A. Martínez, J. García, F. Ramos, P. Sanchis, J. Blasco, and J. Martí, “All-optical switching structure based on a photonic crystal directional coupler,” *Optics Express*, vol. 12, no. 1, pp. 161–167, 2004.
- [114] M. F. Yanik, S. Fan, and M. Soljačić, “High-contrast all-optical bistable switching in photonic crystal microcavities,” *Applied Physics Letters*, vol. 83, no. 14, pp. 2739–2741, 2003.
- [115] P. Russell, “Photonic Crystal Fibers,” *Science*, vol. 299, pp. 358–362, 2003.

- [116] F. Benabid and P. Roberts, “Linear and nonlinear optical properties of hollow core photonic crystal fiber,” *Journal of Modern Optics*, vol. 58, no. 2, pp. 87–124, 2011.
- [117] S. Kalchmair, H. Detz, G. D. Cole, A. M. Andrews, P. Klang, M. Nobile, R. Gansch, C. Ostermaier, W. Schrenk, and G. Strasser, “Photonic crystal slab quantum well infrared photodetector,” *Applied Physics Letters*, vol. 98, no. 1, p. 011105, 2011.
- [118] W. M. Robertson, G. Arjavalingam, R. D. Meade, K. D. Brommer, A. M. Rappe, and J. D. Joannopoulos, “Measurement of photonic band structure in a two-dimensional periodic dielectric array,” *Physical Review Letters*, vol. 68, pp. 2023–2026, 1992.
- [119] M. Kanskar, P. Paddon, V. Pacradouni, R. Morin, A. Busch, J. F. Young, S. R. Johnson, J. MacKenzie, and T. Tiedje, “Observation of leaky slab modes in an air-bridged semiconductor waveguide with a two-dimensional photonic lattice,” *Applied Physics Letters*, vol. 70, no. 11, pp. 1438–1440, 1997.
- [120] E. Chow, S. Y. Lin, S. G. Johnson, P. R. Villeneuve, J. D. Joannopoulos, J. R. Wendt, G. A. Vawter, W. Zubrzycki, H. Hou, and A. Alleman, “Three-dimensional control of light in a two-dimensional photonic crystal slab,” *Nature*, vol. 407, pp. 983–986, 2000.
- [121] T. F. Krauss, R. M. D. L. Rue, and S. Brand, “Two-dimensional photonic-bandgap structures operating at near-infrared wavelengths,” *Nature*, vol. 383, pp. 699–702, 1996.
- [122] S. G. Johnson, S. Fan, P. R. Villeneuve, J. D. Joannopoulos, and L. A. Kolodziejski, “Guided modes in photonic crystal slabs,” *Physical Review B*, vol. 60, pp. 5751–5758, 1999.
- [123] S. Fan and J. D. Joannopoulos, “Analysis of guided resonances in photonic crystal slabs,” *Physical Review B*, vol. 65, no. 23, p. 235112, 2002.
- [124] T. Yoshie, J. Vučković, A. Scherer, H. Chen, and D. Deppe, “High quality two-dimensional photonic crystal slab cavities,” *Applied Physics Letters*, vol. 79, no. 26, pp. 4289–4291, 2001.
- [125] B.-S. Song, S. Noda, T. Asano, and Y. Akahane, “Ultra-high-Q photonic double-heterostructure nanocavity,” *Nature Materials*, vol. 4, pp. 207–210, 2005.
- [126] T. Asano, B.-S. Song, and S. Noda, “Analysis of the experimental Q factors ( $> 1$  million) of photonic crystal nanocavities,” *Optics Express*, vol. 14, no. 5, pp. 1996–2002, 2006.
- [127] M. Notomi, K. Yamada, A. Shinya, J. Takahashi, C. Takahashi, and I. Yokohama, “Extremely Large Group-Velocity Dispersion of Line-Defect Waveguides in Photonic Crystal Slabs,” *Physical Review Letters*, vol. 87, p. 253902, 2001.

- [128] K. Inoue, H. Oda, N. Ikeda, and K. Asakawa, “Enhanced third-order nonlinear effects in slow-light photonic-crystal slab waveguides of line-defect,” *Optics Express*, vol. 17, no. 9, pp. 7206–7216, 2009.
- [129] C. Monat, B. Corcoran, D. Pudo, M. Ebnali-Heidari, C. Grillet, M. Pelusi, D. Moss, B. Eggleton, T. White, L. O’Faolain, and T. Krauss, “Slow Light Enhanced Nonlinear Optics in Silicon Photonic Crystal Waveguides,” *IEEE Journal of Selected Topics in Quantum Electronics*, vol. 16, no. 1, pp. 344–356, 2010.
- [130] J. B. Pendry, D. Schurig, and D. R. Smith, “Controlling Electromagnetic Fields,” *Science*, vol. 312, no. 5781, pp. 1780–1782, 2006.
- [131] J. Valentine, J. Li, T. Zentgraf, G. Bartal, and X. Zhang, “An optical cloak made of dielectrics,” *Nature Materials*, vol. 8, no. 7, pp. 568–571, 2009.
- [132] T. Ergin, N. Stenger, P. Brenner, J. B. Pendry, and M. Wegener, “Three-Dimensional Invisibility Cloak at Optical Wavelengths,” *Science*, vol. 328, pp. 337–339, 2010.
- [133] T. Fujii, Y. Gao, R. Sharma, E. L. Hu, S. P. DenBaars, and S. Nakamura, “Increase in the extraction efficiency of GaN-based light-emitting diodes via surface roughening,” *Applied Physics Letters*, vol. 84, no. 6, pp. 855–857, 2004.
- [134] S. Fan, P. R. Villeneuve, J. D. Joannopoulos, and E. F. Schubert, “High Extraction Efficiency of Spontaneous Emission from Slabs of Photonic Crystals,” *Physical Review Letters*, vol. 78, pp. 3294–3297, 1997.
- [135] S. H. Kim, K.-D. Lee, J.-Y. Kim, M.-K. Kwon, and S.-J. Park, “Fabrication of photonic crystal structures on light emitting diodes by nanoimprint lithography,” *Nanotechnology*, vol. 18, no. 5, p. 055306, 2007.
- [136] K. Bergenek, C. Wiesmann, H. Zull, R. Wirth, P. Sundgren, N. Linder, K. Streubel, and T. F. Krauss, “Directional light extraction from thin-film resonant cavity light-emitting diodes with a photonic crystal,” *Applied Physics Letters*, vol. 93, no. 23, p. 231109, 2008.
- [137] C. Wiesmann, K. Bergenek, N. Linder, and U. Schwarz, “Photonic crystal LEDs - designing light extraction,” *Laser & Photonics Reviews*, vol. 3, no. 3, pp. 262–286, 2009.
- [138] J. J. Wierer, A. David, and M. M. Megens, “III-nitride photonic-crystal light-emitting diodes with high extraction efficiency,” *Nature Photonics*, vol. 3, pp. 163–169, 2009.
- [139] R. Windisch, C. Rooman, S. Meinschmidt, P. Kiesel, D. Zipperer, G. H. Döhler, B. Dutta, M. Kuijk, G. Borghs, and P. Heremans, “Impact of texture-enhanced transmission on high-efficiency surface-textured light-emitting diodes,” *Applied Physics Letters*, vol. 79, no. 15, pp. 2315–2317, 2001.

- [140] R. Windisch, C. Rooman, B. Dutta, A. Knobloch, G. Borghs, G. Dohler, and P. Heremans, "Light-extraction mechanisms in high-efficiency surface-textured light-emitting diodes," *IEEE Journal of Selected Topics in Quantum Electronics*, vol. 8, no. 2, pp. 248–255, 2002.
- [141] M. R. Krames, M. Ochiai-Holcomb, G. E. Höfler, C. Carter-Coman, E. I. Chen, I.-H. Tan, P. Grillot, N. F. Gardner, H. C. Chui, J.-W. Huang, S. A. Stockman, F. A. Kish, M. G. Craford, T. S. Tan, C. P. Kocot, M. Hueschen, J. Poselt, B. Loh, G. Sasser, and D. Collins, "High-power truncated-inverted-pyramid  $(Al_xGa_{1-x})_{0.5}In_{0.5}P/GaP$  light-emitting diodes exhibiting  $> 50\%$  external quantum efficiency," *Applied Physics Letters*, vol. 75, no. 16, pp. 2365–2367, 1999.
- [142] H.-G. Park, S.-H. Kim, S.-H. Kwon, Y.-G. Ju, J.-K. Yang, J.-H. Baek, S.-B. Kim, and Y.-H. Lee, "Electrically Driven Single-Cell Photonic Crystal Laser," *Science*, vol. 305, pp. 1444–1447, 2004.
- [143] O. Painter, R. K. Lee, A. Scherer, A. Yariv, J. D. O'Brien, P. D. Dapkus, and I. Kim, "Two-Dimensional Photonic Band-Gap Defect Mode Laser," *Science*, vol. 284, no. 5421, pp. 1819–1821, 1999.
- [144] R. Lee, O. Painter, B. Kitzke, A. Scherer, and A. Yariv, "Photonic bandgap disk laser," *Electronics Letters*, vol. 35, no. 7, pp. 569–570, 1999.
- [145] V. I. Kopp, B. Fan, H. K. M. Vithana, and A. Z. Genack, "Low-threshold lasing at the edge of a photonic stop band in cholesteric liquid crystals," *Optics Letters*, vol. 23, no. 21, pp. 1707–1709, 1998.
- [146] M. Imada, S. Noda, A. Chutinan, T. Tokuda, M. Murata, and G. Sasaki, "Coherent two-dimensional lasing action in surface-emitting laser with triangular-lattice photonic crystal structure," *Applied Physics Letters*, vol. 75, no. 3, pp. 316–318, 1999.
- [147] K. Inoue, M. Sasada, J. Kawamata, K. Sakoda, and J. W. Haus, "A Two-Dimensional Photonic Crystal Laser," *Japanese Journal of Applied Physics*, vol. 38, no. Part 2, No. 2B, pp. L157–L159, 1999.
- [148] D. Ohnishi, T. Okano, M. Imada, and S. Noda, "Room temperature continuous wave operation of a surface-emitting two-dimensional photonic crystal diode laser," *Optics Express*, vol. 12, no. 8, pp. 1562–1568, 2004.
- [149] M. Lončar, A. Scherer, and Y. Qiu, "Photonic crystal laser sources for chemical detection," *Applied Physics Letters*, vol. 82, no. 26, pp. 4648–4650, 2003.
- [150] E. Chow, A. Grot, L. W. Mirkarimi, M. Sigalas, and G. Girolami, "Ultracompact biochemical sensor built with two-dimensional photonic crystal microcavity," *Optics Letters*, vol. 29, no. 10, pp. 1093–1095, 2004.
- [151] M. Lončar, B. G. Lee, L. Diehl, M. A. Belkin, F. Capasso, M. Giovannini, J. Faist,

- and E. Gini, “Design and fabrication of photonic crystal quantum cascade lasers for optofluidics,” *Optics Express*, vol. 15, no. 8, pp. 4499–4514, 2007.
- [152] Y. Kurosaka, S. Iwahashi, Y. Liang, K. Sakai, E. Miyai, W. Kunishi, D. Ohnishi, and S. Noda, “On-chip beam-steering photonic-crystal lasers,” *Nature Photonics*, vol. 4, pp. 447–450, 2010.
- [153] R. Colombelli, K. Srinivasan, M. Troccoli, O. Painter, C. F. Gmachl, D. M. Tennant, A. M. Sergent, D. L. Sivco, A. Y. Cho, and F. Capasso, “Quantum Cascade Surface-Emitting Photonic Crystal Laser,” *Science*, vol. 302, pp. 1374–1377, 2003.
- [154] G. Xu, V. Moreau, Y. Chassagneux, A. Bousseksou, R. Colombelli, G. Patriarche, G. Beaudoin, and I. Sagnes, “Surface-emitting quantum cascade lasers with metallic photonic-crystal resonators,” *Applied Physics Letters*, vol. 94, no. 22, p. 221101, 2009.
- [155] M. Tonouchi, “Cutting-edge terahertz technology,” *Nature Photonics*, vol. 1, pp. 97–105, 2007.
- [156] H. Zhang, L. A. Dunbar, G. Scalari, R. Houdré, and J. Faist, “Terahertz photonic crystal quantum cascade lasers,” *Optics Express*, vol. 15, no. 25, pp. 16818–16827, 2007.
- [157] A. Benz, C. Deutsch, G. Fasching, K. Unterrainer, A. M. Andrews, P. Klang, W. Schrenk, and G. Strasser, “Active photonic crystal terahertz laser,” *Optics Express*, vol. 17, no. 2, pp. 941–946, 2009.
- [158] K. T. Posani, V. Tripathi, S. Annamalai, N. R. Weisse-Bernstein, S. Krishna, R. Perahia, O. Crisafulli, and O. J. Painter, “Nanoscale quantum dot infrared sensors with photonic crystal cavity,” *Applied Physics Letters*, vol. 88, no. 15, p. 151104, 2006.
- [159] J.-K. Yang, M.-K. Seo, I.-K. Hwang, S.-B. Kim, and Y.-H. Lee, “Polarization-selective resonant photonic crystal photodetector,” *Applied Physics Letters*, vol. 93, no. 21, p. 211103, 2008.
- [160] S. Schartner, *Optical Cavities for Mid-Infrared Devices*. PhD thesis, Vienna University of Technology, 2009.
- [161] S. Schartner, W. Schrenk, S. Golka, M. Austerer, P. Klang, A. M. Andrews, and G. Strasser, “Photonic Crystal Infrared Photodetectors,” in *Conference on Lasers and Electro-Optics/Quantum Electronics and Laser Science Conference and Photonic Applications Systems Technologies*, p. CTuZ2, Optical Society of America, 2007.
- [162] S. C. Lee, S. Krishna, and S. R. J. Brueck, “Quantum dot infrared photodetector enhanced by surface plasma wave excitation,” *Optics Express*, vol. 17, no. 25, pp. 23160–23168, 2009.

- [163] C.-Y. Chang, H.-Y. Chang, C.-Y. Chen, M.-W. Tsai, Y.-T. Chang, S.-C. Lee, and S.-F. Tang, "Wavelength selective quantum dot infrared photodetector with periodic metal hole arrays," *Applied Physics Letters*, vol. 91, no. 16, p. 163107, 2007.
- [164] I. R. McKerracher, H. T. Hattori, L. Fu, H. H. Tan, and C. Jagadish, "Photonic crystal-enhanced quantum dot infrared photodetectors," in *Society of Photo-Optical Instrumentation Engineers (SPIE) Conference Series*, vol. 7039 of *Society of Photo-Optical Instrumentation Engineers (SPIE) Conference Series*, 2008.
- [165] S. Schartner, S. Golka, C. Pflügl, W. Schrenk, A. M. Andrews, T. Roch, and G. Strasser, "Band structure mapping of photonic crystal intersubband detectors," *Applied Physics Letters*, vol. 89, no. 15, p. 151107, 2006.
- [166] S. Schartner, S. Golka, M. Austerer, A. M. Andrews, W. Schrenk, E. Gornik, and G. Strasser, "Characterization of planar photonic crystals using a quantum well infrared photodetector," *Physica Status Solidi (b)*, vol. 244, no. 8, pp. 2916–2925, 2007.
- [167] S. Schartner, L. Hoffmann, S. Golka, M. Austerer, P. Klang, A. M. Andrews, W. Schrenk, and G. Strasser, "Polarization Dependent Band Structure Mapping of Photonic Crystal Mid Infrared Photodetectors," in *CLEO/Europe and IQEC 2007 Conference Digest*, p. CK95, Optical Society of America, 2007.
- [168] S. Schartner, M. Nobile, W. Schrenk, A. M. Andrews, P. Klang, and G. Strasser, "Photocurrent response from photonic crystal defect modes," *Optics Express*, vol. 16, no. 7, pp. 4797–4803, 2008.
- [169] S. Schartner, M. Nobile, M. Austerer, E. Mujagić, L. K. Hoffmann, D. Andrijasević, H. Detz, W. Schrenk, P. Klang, A. M. Andrews, and G. Strasser, "Photonic crystal band edge and defect states in the spectral response of intersubband detectors," *AIP Conference Proceedings*, vol. 1199, no. 1, pp. 149–150, 2010.
- [170] H. Yang, L. Chen, Z. Qiang, and W. Zhou, "Characteristics of Photonic Crystal Cavity Based Infrared Photodetectors," in *Lasers and Electro-Optics Society, 2007. LEOS 2007. The 20th Annual Meeting of the IEEE*, pp. 36–37, 2007.
- [171] W. Zhou, L. Chen, Z. Qiang, and G. J. Brown, "Spectrally selective infrared absorption in defect-mode photonic-crystal-slab cavity," *Journal of Nanophotonics*, vol. 1, p. 013515, 2007.
- [172] H. Chen, N. Xi, J. Lou, K. Lai, L. Chen, and B. Song, "Photonic crystal with a HfO<sub>2</sub> defect to improve performance of carbon nanotube based photodetectors," in *11th IEEE Conference on Nanotechnology (IEEE-NANO)*, pp. 978–981, 2011.
- [173] H. Haug and S. W. Koch, *Quantum theory of the optical and electronic properties of semiconductors*. Singapore: World Scientific, 1994.

- [174] G. Bastard, *Wave mechanics applied to semiconductor heterostructures*. Les Ulis Cedex, France New York, N.Y.: Les Editions de Physique Halsted Press, 1988.
- [175] D. D. Coon and R. P. G. Karunasiri, “New mode of IR detection using quantum wells,” *Applied Physics Letters*, vol. 45, no. 6, pp. 649–651, 1984.
- [176] H. C. Liu, “Dependence of absorption spectrum and responsivity on the upper state position in quantum well intersubband photodetectors,” *Journal of Applied Physics*, vol. 73, no. 6, pp. 3062–3067, 1993.
- [177] H. C. Liu, “Photoconductive gain mechanism of quantum-well intersubband infrared detectors,” *Applied Physics Letters*, vol. 60, no. 12, pp. 1507–1509, 1992.
- [178] G. Reider, *Photonik : eine Einführung in die Grundlagen*. Wien: Springer, 2005.
- [179] A. V. Barve, T. Rotter, Y. Sharma, S. J. Lee, S. K. Noh, and S. Krishna, “Systematic study of different transitions in high operating temperature quantum dots in a well photodetectors,” *Applied Physics Letters*, vol. 97, no. 6, p. 061105, 2010.
- [180] R. J. D. Tilley, *Crystals and Crystal Structures*. Hoboken, NJ: Wiley, 2006.
- [181] J. Maxwell and T. Torrance, *A Dynamical Theory of the Electromagnetic Field*. Scottish Academic Press, 1982.
- [182] J. Jackson, *Classical Electrodynamics*. Wiley, 1999.
- [183] H. A. Macleod, *Thin-film Optical Filters*. Bristol Philadelphia: Institute of Physics Pub, 2001.
- [184] S. G. Johnson and J. D. Joannopoulos, “MPB (MIT Photonic Bands).” [http://ab-initio.mit.edu/wiki/index.php/MIT\\_Photonic\\_Bands](http://ab-initio.mit.edu/wiki/index.php/MIT_Photonic_Bands), 2012.
- [185] R. Gansch, “Tuning of Resonances in Photonic Crystal Slabs,” Master’s thesis, Technische Universität Wien, 2010.
- [186] K. Yee, “Numerical solution of initial boundary value problems involving maxwell’s equations in isotropic media,” *IEEE Transactions on Antennas and Propagation*, vol. 14, no. 3, pp. 302–307, 1966.
- [187] A. Taflove, “Application of the Finite-Difference Time-Domain Method to Sinusoidal Steady-State Electromagnetic-Penetration Problems,” *IEEE Transactions on Electromagnetic Compatibility*, vol. EMC-22, no. 3, pp. 191–202, 1980.
- [188] H. Benisty, D. Labilloy, C. Weisbuch, C. J. M. Smith, T. F. Krauss, D. Casagne, A. Béraud, and C. Jouanin, “Radiation losses of waveguide-based two-dimensional photonic crystals: Positive role of the substrate,” *Applied Physics Letters*, vol. 76, no. 5, pp. 532–534, 2000.
- [189] S. Shi, C. Chen, and D. W. Prather, “Revised plane wave method for dispersive material and its application to band structure calculations of photonic crystal slabs,” *Applied Physics Letters*, vol. 86, no. 4, p. 043104, 2005.

- [190] C. Sirtori, C. Gmachl, F. Capasso, J. Faist, D. L. Sivco, A. L. Hutchinson, and A. Y. Cho, “Long-wavelength ( $\lambda \approx 8\text{--}11.5\ \mu\text{m}$ ) semiconductor lasers with waveguides based on surface plasmons,” *Optics Letters*, vol. 23, no. 17, pp. 1366–1368, 1998.
- [191] R. Gansch, S. Kalchmair, H. Detz, A. M. Andrews, P. Klang, W. Schrenk, and G. Strasser, “Higher order modes in photonic crystal slabs,” *Optics Express*, vol. 19, no. 17, pp. 15990–15995, 2011.
- [192] S. Kalchmair, R. Gansch, S. I. Ahn, A. M. Andrews, H. Detz, T. Zederbauer, E. Mujagić, P. Reininger, G. Lasser, W. Schrenk, and G. Strasser, “Detectivity enhancement in quantum well infrared photodetectors utilizing a photonic crystal slab resonator,” *Optics Express*, vol. 20, no. 5, pp. 5622–5628, 2012.
- [193] C. Gmachl, F. Capasso, D. L. Sivco, and A. Y. Cho, “Recent progress in quantum cascade lasers and applications,” *Reports on Progress in Physics*, vol. 64, no. 11, p. 1533, 2001.
- [194] H. Lipsanen, M. Sopanen, M. Taskinen, J. Tulkki, and J. Ahopelto, “Enhanced optical properties of in situ passivated near-surface  $Al_xGa_{1-x}As/GaAs$  quantum wells,” *Applied Physics Letters*, vol. 68, no. 16, pp. 2216–2218, 1996.
- [195] J. S. Blakemore, “Semiconducting and other major properties of gallium arsenide,” *Journal of Applied Physics*, vol. 53, no. 10, pp. R123–R181, 1982.
- [196] S. Schartner, S. Kalchmair, A. M. Andrews, P. Klang, W. Schrenk, and G. Strasser, “Post-fabrication fine-tuning of photonic crystal quantum well infrared photodetectors,” *Applied Physics Letters*, vol. 94, no. 23, p. 231117, 2009.
- [197] S. Kalchmair, R. Gansch, T. Z. A. M. Andrews, H. Detz, W. Schrenk, and G. Strasser, “Focusing of Light with a Plasmonic Lens onto a Mid-Infrared Quantum Well Photodetector,” in *Proceedings of the 10th International Symposium on Photonic and Electromagnetic Crystal Structures*, 2012.

# Abbreviations

$SiN_x$  Silicon Nitride

1D One-dimensional

2D Two-dimensional

3D Three-dimensional

AlGaAs Aluminium Gallium Arsenide

BLIP Background Limited Performance

CB Conduction band

DBR Distributed Bragg Reflector

DFB Distributed Feedback

DLIP Detector Limited Performance

DTGS Deuterium Triglycine Sulfate

DWELL Dots-In-a-WELL

FBZ First Brillouin Zone

FDTD Finite Difference Time Domain

FFT Fast Fourier Transformation

FOV Field of View

FPA Focal Plane Array

FTIR Fourier Transform Infrared Spectrometer

g-r noise generation-recombination noise

GaAs Gallium Arsenide

GaN Gallium Nitride

HgCdTe Mercury Cadmium Telluride

IBZ	Irreducible Brillouin Zone
InGaAs	Indium Gallium Arsenide
InP	Indium Phosphide
InSb	Indium Antimonide
IR	infrared
ISB	Intersubband
ISBT	Intersubband transition
LED	Light Emitting Diode
MBE	Molecular Beam Epitaxy
MCT	Mercury Cadmium Telluride
NW	Nanowires
PBG	Photonic Band Gap
PC	Photonic Crystal
PCS	Photonic Crystal Slab
PWEM	Plane Wave Expansion Method
QCD	Quantum Cascade Detector
QCL	Quantum Cascade Laser
QD	Quantum Dots
QDIP	Quantum Dot Infrared Photodetector
QW	Quantum Well
QWIP	Quantum Well Infrared Photodetector
RCE	Resonant Cavity Enhancement
RPWEM	Revised Plane Wave Method
Si	Silicon
TE	Transverse-Electric
TEM	Transverse-Electro-Magnetic
TM	Transverse-Magnetic

# List of Publications

## Journals publications

- J1** S. Kalchmair, R. Gansch, S.I. Ahn, A.M. Andrews, H. Detz, T. Zederbauer, E. Mujagić, P. Reininger, G. Lasser, W. Schrenk, G. Strasser, *Detectivity enhancement in quantum well infrared photodetectors utilizing a photonic crystal slab resonator*, Opt. Express 20(5), 5622-5628 (2012), doi: 10.1364/OE.20.005622
- J2** P. Reininger, S. Kalchmair, R. Gansch, A.M. Andrews, H. Detz, T. Zederbauer, S.I. Ahn, W. Schrenk, G. Strasser, *Optimized photonic crystal design for quantum well infrared photodetectors*, Proc. SPIE 8425, 84250A (2012), doi: 10.1117/12.923045, *best student paper award*
- J3** S.I. Ahn, C. Schwarzer, S. Kalchmair, R. Gansch, D. Ristanic, T. Zederbauer, P. Reininger, H. Detz, A. M. Andrews, W. Schrenk, G. Strasser, *Facet Reflectivity Reduction of Quantum Cascade Lasers by Tilted Facets*, Proc. SPIE 8432, 84320L (2012), doi: 10.1117/12.922417
- J4** O. Glushko, R. Brunner, R. Meisels, S. Kalchmair, G. Strasser, *Extraordinary transmission in metal hole array-photonic crystal hybrid structures*, Opt. Express, accepted for publication (2012)
- J5** J. K. Choi, N. Vagidov, A. Sergeev, S. Kalchmair, G. Strasser, F. Vasko, V. Mitin, *Asymmetrically Doped GaAs/AlGaAs Double-Quantum-Well Structure for Voltage-Tunable Infrared Detection*, Japanese Journal of Applied Physics 51, accepted for publication (2012) doi: 10.1143/JJAP.51.xx xxxx
- J6** S. Kalchmair, R. Gansch, H. Detz, A.M. Andrews, P. Klang, W. Schrenk, G. Strasser, *Photonic Crystal Slab Quantum Well Photodetectors* Proc. GMe Forum 2011, 53 (2011), ISBN: 978-3-901578-23-6
- J7** R. Gansch, S. Kalchmair, H. Detz, A. M. Andrews, P. Klang, W. Schrenk, G. Strasser, *Higher order modes in photonic crystal slabs*, Optics Express 19, 15990-15995 (2011), doi: 10.1364/OE.19.015990
- J8** S. Kalchmair, H. Detz, G.D. Cole, A.M. Andrews, P. Klang, M. Nobile, R. Gansch, C. Ostermaier, W. Schrenk, G. Strasser, *Photonic Crystal Slab Quantum Well Infrared Photodetector*, Appl. Phys. Lett. 98, 011105 (2011), doi: 10.1063/1.3537954

- J9** S.I. Ahn, E. Mujagić, M. Nobile, H. Detz, S. Kalchmair, C. Schwarzer, A. M. Andrews, P. Klang, W. Schrenk, G. Strasser, *Electrical beam steering of Y-coupled quantum cascade lasers*, Appl. Phys. Lett. 96 (14) 141113 (2010), doi: 10.1063/1.3374335
- J10** S. Schartner, S. Kalchmair, A.M. Andrews, P. Klang, W. Schrenk, G. Strasser, *Post-fabrication Fine-Tuning of Photonic Crystal Quantum Well Infrared Photodetectors*, Appl. Phys. Lett. 94, 231117 (2009), doi: 10.1063/1.3152769
- J11** S. Kalchmair, N. Jährling, K. Becker, H. Dodt, *Image contrast enhancement in confocal ultramicroscopy* Opt. Lett. 36, 79-81 (2009), doi: 10.1364/OL.35.000079

## Invited talks

- I1** S. Kalchmair, R. Gansch, P. Reininger, S. Schartner, A.M. Andrews, H. Detz, P. Klang, T. Zederbauer, W. Schrenk, G. Strasser, *Resonant photonic detection*, NanoPhotonicsMeeting, Vienna, Austria, Nov 10-11, 2011
- I2** R. Gansch, S. Kalchmair, H. Detz, A. M. Andrews, P. Klang, W. Schrenk, G. Strasser, *Resonantly enhanced absorption in photonic crystal slab quantum well infrared photodetectors*, Institut für Physik, Montanuniversität Leoben, Austria, Jun 21, 2011
- I3** S. Kalchmair, R. Gansch, P. Reininger, S. Ahn, C. Schwarzer, A. Alexewicz, A.M. Andrews, H. Detz, W. Schrenk, G. Strasser, *Photonic Crystal Resonators in Quantum Well Photodetectors*, Seminar on photonic crystal mid-IR and THz QWIPs, Helmholtz-Zentrum Dresden-Rossendorf, Germany, Aug 24, 2011
- I4** S. Kalchmair, S. Ahn, R. Gansch, E. Mujagić, C. Schwarzer, M. Nobile, C. Ostermaier, M. Schramböck, S. Schartner, A.M. Andrews, H. Detz, P. Klang, W. Schrenk, and G. Strasser, *Tailored Mid-infrared Optoelectronics: Design, Processing and Systems*, 17th Seminar on Electron & Ion Beam Nanofabrication for Applications in Nanotechnology, Dortmund, Germany, Feb 21-22, 2011
- I5** S. Schartner, S. Kalchmair, M. Nobile, E. Mujagić, B. Basnar, H. Detz, P. Klang, A.M. Andrews, W. Schrenk, G. Strasser, *Photonic Crystal Photodetectors*, Institut für Physik, Montanuniversität Leoben, Austria, Apr 30, 2009
- I6** H. Dodt, N. Jährling, S. Saghafi, S. Kalchmair, K. Becker, *Visualization of neuronal networks in the whole mouse brain and mouse embryos by ultramicroscopy* Topical problems of Biophotonics, Nizhny Novgorod, Russia, Jul 19, 2009

## Contributed oral talks

- O1** R. Gansch, S. Kalchmair, P. Reininger, H. Detz, T. Zederbauer, A.M. Andrews, W. Schrenk, G. Strasser, *Stacked Photonic Crystal Slabs as Resonant Cavities for Multicolor Quantum Well Infrared Photodetectors*, QSIP 2012, Cargese, France, Jun 17-22, 2012
- O2** S. Kalchmair, R. Gansch, A.M. Andrews, H. Detz, T. Zederbauer, W. Schrenk, G. Strasser, *Focusing of Light with a Plasmonic Lens onto Mid-Infrared Quantum Well Photodetector*, PECS-X, Santa Fe, USA, Jun 3-8, 2012
- O3** R. Gansch, S. Kalchmair, H. Detz, T. Zederbauer, A.M. Andrews, W. Schrenk, G. Strasser, *Photonic Crystal Slabs for Resonant Cavity Enhancement of Quantum Well Infrared Photodetectors*, PECS-X, Santa Fe, USA, Jun 3-8, 2012
- O4** S. Kalchmair, R. Gansch, E. Mujagić, S.I. Ahn, P. Reininger, G. Lasser, A.M. Andrews, H. Detz, T. Zederbauer, W. Schrenk, G. Strasser, *Increased Detectivity and Operation Temperature in Photonic Crystal Slab Quantum Well Photodetectors*, Cleo 2012, San Jose, USA, May 6-12, 2012
- O5** S. Kalchmair, R. Gansch, P. Reininger, S.I. Ahn, H. Detz, A.M. Andrews, W. Schrenk, G. Strasser, *Resonant detectivity enhancement of quantum well infrared photodetectors by photonic crystal slabs*, SPIE Photonics Europe, Brussels, Belgium, Apr 16-19, 2012 *Best Student Paper-Award*
- O6** R. Gansch, S. Kalchmair, P. Reininger, H. Detz, A.M. Andrews, W. Schrenk, G. Strasser, *Responsivity enhancement of QWIPs by photonic crystal slabs*, Photonics West 2012, San Francisco, USA, Jan 21-26, 2012
- O7** R. Meisels, R. Brunner, O. Glushko, S. Kalchmair, R. Gansch, G. Strasser, *Using photonic crystal slabs to optimize quantum-well photo-detectores*, Photonica 2011, 3rd Int. School & Conf. on Photonics, Belgrade, Serbia, Aug 29-Sep 2, 2011
- O8** R. Gansch, S. Kalchmair, H. Detz, A. M. Andrews, P. Klang, W. Schrenk, G. Strasser, *Photonic Crystal Slab Quantum Well Infrared Photodetector*, Annual Meeting of the Austrian & Swiss Phys. Soc., Lausanne, Switzerland, Jun 15-17, 2011
- O9** R. Gansch, S. Kalchmair, H. Detz, P. Klang, A.M. Andrews, W. Schrenk, G. Strasser, *Experimental verification of the revised plane wave expansion method for photonic crystal slabs*, 1st MIRTHE-IRON-SensorCAT Virtual Conference, Jan 19-20, 2011
- O10** S. Kalchmair, H. Detz, G. Cole, A.M. Andrews, M. Nobile, P. Klang, W. Schrenk, G. Strasser, *Quantum well photodetector in a free-standing photonic crystal slab*, MNE2010, Genoa, Italy. Sep 19-22, 2010
- O11** A. Glushko, R. Meisels, S. Kalchmair, G. Strasser, *Resonant coupling of light into*

- quantum well infrared photodetectors with embedded 2D photonic crystal*, SPIE Photonics Europe 2010, Brussels, Belgium, Apr 12-16, 2010
- O12** S. Kalchmair, S. Schartner, A.M. Andrews, P. Klang, W. Schrenk, G. Strasser, *Fine Tuning of Photonic Crystals Post Fabrication using QWIP Photo-Response*, ITQW10, Montreal, Canada, Sep 6-11, 2009
- O13** R. Meisels, O. Glushko, S. Kalchmair, G. Strasser, *3D FDTD simulations of photonic devices*, Annual Meeting of the Austrian & Swiss Phys. Soc., Innsbruck, Austria, Sep 2-4, 2009
- O14** S. Kalchmair, S. Schartner, A.M. Andrews, P. Klang, O. Glushko, R. Meisels, W. Schrenk, G. Strasser, *Post-fabrication Fine-tuning of Photonic Crystal Devices*, Annual Meeting of the Austrian & Swiss Phys. Soc., Innsbruck, Austria, Sep 2-4, 2009
- O15** H. Dodt, N. Jährling, S. Saghafi, S. Kalchmair, K. Becker, *Visualization of Neuronal networks in the mouse brain and mouse embryos by ultramicroscopy* Graduate School Meeting, Münster, Deutschland, May 11-13, 2011

## Poster presentations

- P1** S. Ahn, C. Schwarzer, S. Kalchmair, R. Gansch, D. Ristanic, T. Zederbauer, H. Detz, A.M. Andrews, W. Schrenk, G. Strasser, *The Influence of a Tilted Facet on Quantum Cascade Lasers*, IQCLSW 2012, Baden, Austria, Sep 2-6, 2012
- P2** R. Gansch, S. Kalchmair, H. Detz, T. Zederbauer, A.M. Andrews, W. Schrenk, G. Strasser, *Impedance matched resonant cavities for quantum well infrared photodetectors*, IQCLSW 2012, Baden, Austria, Sep 2-6, 2012
- P3** P. Reininger, B. Schwarz, S. Kalchmair, R. Gansch, O. Baumgartner, Z. Stanojevic, H. Kosina, W. Schrenk, G. Strasser, *Simulation of a dual wavelength quantum cascade laser in a photonic crystal cavity*, IQCLSW 2012, Baden, Austria, Sep 2-6, 2012
- P4** R. Gansch, S. Kalchmair, H. Detz, T. Zederbauer, A.M. Andrews, W. Schrenk, G. Strasser, *Resonant cavity enhanced quantum well infrared photodetectors showing improved temperature performance*, 31st ICPS, Zürich, Switzerland, Jul 29-Aug 3, 2012
- P5** P. Reininger, R. Gansch, S. Kalchmair, H. Detz, T. Zederbauer, A.M. Andrews, W. Schrenk, G. Strasser, *Detectivity Improvement of Quantum Well Infrared Photodetectors using a Photonic Crystal Slab as Resonant Cavity*, ICSNN 2012, Dresden, Germany, Jul 22-27, 2012
- P6** S.I. Ahn, S. Kalchmair, C. Schwarzer, R. Gansch, H. Detz, A. M. Andrews, W.

- 
- Schrenk, G. Strasser, *Facet Reflectivity Reduction of Quantum Cascade Lasers by Tilted Facets*, GME Forum 2012, Vienna, Austria, Mar 29-30, 2012
- P7** S. Kalchmair, R. Gansch, P. Reininger, A. M. Andrews, H. Detz, T. Zederbauer, W. Schrenk, G. Strasser, *Photonic Crystal Slabs for Resonant Photodetection in Quantum Wells*, GME Forum 2012, Vienna, Austria, Mar 29-30, 2012
- P8** S. Kalchmair, R. Gansch, P. Reininger, A.M. Andrews, H. Detz, T. Zederbauer, W. Schrenk, G. Strasser, *High Detectivity and Operation Temperature of Photonic Crystal Slab QWIPs*, 17th Int. Winterschool on New Developments in Solid State Physics, Mauterndorf, Austria, Feb 12-17, 2012
- P9** S. Kalchmair, R. Gansch, G.D. Cole, H. Detz, A.M. Andrews, P. Klang, W. Schrenk, G. Strasser, *Photonic Crystal Slabs for Resonant Photodetection in Quantum Wells*, Metamaterials 2011, Barcelona, Spain, Oct 10-15, 2011
- P10** S. Kalchmair, R. Gansch, G.D. Cole, H. Detz, A.M. Andrews, P. Klang, W. Schrenk, G. Strasser, *Temperature effects in Photonic Crystal Slab Quantum Well Photodetectors*, ITQW11, Badesi, Italy, Sep 11-17, 2011
- P11** R. Gansch, S. Kalchmair, H. Detz, A. M. Andrews, P. Klang, W. Schrenk, G. Strasser, *Photonic Crystal Slab Quantum Well Infrared Photodetector*, Junior Scientist Conf. "Einstein's in the City 2011", New York, USA, Apr 14-15, 2011
- P12** S. Kalchmair, R. Gansch, H. Detz, A.M. Andrews, P. Klang, W. Schrenk, G. Strasser, *Photonic Crystal Slab Quantum Well Photodetectors*, GME Forum 2011, Vienna, Austria, Apr 14-15, 2011
- P13** S. Kalchmair, H. Detz, M. Nobile, A.M. Andrews, P. Klang, W. Schrenk, G. Strasser, *Direct Measurement of Guided Resonances in a Photonic Crystal Slab by quantum Well Photodetector*, PECS-IX Conf., Granada, Spain, Sep 26-30, 2010
- P14** R. Meisels, O. Glushko, S. Kalchmair, G. Strasser, *Resonant polarization conversion and extraordinary transmission through sub-wavelength holes due to coupling of light to photonic crystal modes*, PECS-IX Conf., Granada, Spain, Sep 26-30, 2010
- P15** R. Gansch, S. Kalchmair, G. Strasser, *Numerical Study of Photonic Crystal SLAB based Quantum Well Infrared Photodetectors*, ÖPG2010, Salzburg, Austria, Sep 6-10, 2010
- P16** R. Meisels, O. Glushko, S. Kalchmair, G. Strasser, *Resonant Polarization Conversion and Extraordinary Transmission in Photonic Crystal Slabs Covered with Metal*, ÖPG2010, Salzburg, Austria, Sep 6-10, 2010
- P17** S. I. Ahn, E. Mujagić, M. Nobile, H. Detz, S. Kalchmair, C. Schwarzer, A.M. Andrews, P. Klang, W. Schrenk, G. Strasser, *Electronic beam steering of phase*

- locked quantum cascade laser*, 16th Int. Winterschool on New Developments in Solid State Physics, Mauterndorf, Austria, Feb 22-26, 2010
- P18** O. Glushko, R. Meisels, S. Kalchmair, G. Strasser, *Enhanced optical transmission through the sub-wavelength holes due to the coupling of light to photonic crystals*, 16th Int. Winterschool on New Developments in Solid State Physics, Mauterndorf, Austria, Feb 22-26, 2010
- P19** S. Kalchmair, S. Schartner, A.M. Andrews, P. Klang, O. Glushko, R. Meisels, W. Schrenk, G. Strasser, *Post-Fabrication Precision Tuning of Photonic Crystal Devices*, 16th Int. Winterschool on New Developments in Solid State Physics, Mauterndorf, Austria, Feb 22-26, 2010
- P20** S. Kalchmair, S. Schartner, A. M. Andrews, P. Klang, O. Glushko, R. Meisels, W. Schrenk, G. Strasser, *Post-Fabrication Precision Tuning of Photonic Crystal Microstructures*, 35th Int. Conf. on Micro & Nano Engineering (MNE), Ghent, Belgium, Sep 28-Oct 1, 2009
- P21** C. Schwarzer, E. Mujagić, C. Deutsch, H. Detz, M. Nobile, S. Kalchmair, P. Klang, A. M. Andrews, W. Schrenk, K. Unterrainer, G. Strasser, *Shaped Beams in Vertically Emitting Quantum Cascade Ring Lasers*, Annual Meeting of the Austrian & Swiss Phys. Soc., Innsbruck, Austria, Sep 2-4, 2009
- P22** O. Glushko, R. Meisels, S. Schartner, S. Kalchmair, G. Strasser, *Optimization of quantum well infrared photodetectors with embedded photonic crystals*, Photonica 2009, Int. School & Conf. on Photonics, Belgrade, Serbia, Aug 24-28, 2009
- P23** C. Ostermaier, S. Ahn, K. Potzger, M. Helm, S. Kalchmair, D. Pogany, J. Lee, S. Hahm, J. Lee, *Realization of Inversion-type GaN MOSFETs with Ar Implantation for Device Isolation*, Junior Scientist Conference 2008, Technische Universität Wien, Wien, Nov 16-18, 2008

## Master thesis

S. Kalchmair, *Image Improvement by Structured Illumination in Ultramicroscopy*, Institut für Festkörperelektronik, Technische Universität Wien, Wien, 2008

## Awards

Raith Micrograph Award 2011

# Curriculum Vitae

## Personal Data

Stefan Kalchmair

born on April 17<sup>th</sup> 1981

Wels, Austria

## Academics

- |                         |   |
|-------------------------|---|
| 2002 - 2006             | B.Sc. <i>with Honors</i> in Electrical Engineering<br>Vienna University of Technology, Vienna, Austria                |
| Sept 2005 - Feb<br>2006 | Exchange Semester in the department of Electrical Engineering<br>Universitat Politècnica de València, Valencia, Spain |
| 2006 - 2008             | M.Sc. <i>with Honors</i> in Electrical Engineering<br>Vienna University of Technology, Vienna, Austria                |
| 2008 - 2012             | PhD Candidate in Solid State Physics<br>Vienna University of Technology, Vienna, Austria                              |

## Scientific Career

- |                        |   |
|------------------------|---|
| Jul - Aug 2005         | Individual Research Project with Prof. Ernst Wintner<br>Vienna University of Technology, Vienna, Austria  |
| Jul 2007 - Dec<br>2008 | Research Assistant at the Institute for Solid State Electronics,<br>Department for Bioelectronics<br>Vienna University of Technology, Vienna, Austria |
| 2008 - 2012            | Research Assistant at the Center for Micro- and Nanostructures<br>Vienna University of Technology, Vienna, Austria                                    |